DECEMBER 1991

FOM-INSTITUUT
VOOR
PLASMAFYSICA
RIJNHUIZEN

ASSOCIATIE
EURATOM-FOM

# EXTERNAL RESISTIVE MODES AND TOROIDICITY INDUCED ALFVEN EIGENMODES IN TOKAMAKS

EXTENSIONS OF THE NUMERICAL PROGRAM CASTOR
FOR THE INVESTIGATION OF IDEAL AND RESISTIVE
MHD STABILITY OF JET DISCHARGES

G.T.A. HUYSMANS, J.P. GOEDBLOED, AND S. POEDTS

RIJNHUIZEN REPORT 91-209

This work was performed as part of the research programme of the association agreement of Euratom and the 'Stichting voor Fundamenteel Onderzoek der Materie' (FOM) with financial support from the 'Nederlandse Organisatie voor Wetenschappelijk Onderzoek' (NWO) and Euratom.

POSTBUS 1207
3430 BE NIEUWEGEIN
NEDERLAND
EDISONBAAN 14
3439 MN NIEUWEGEIN
TEL. 03402 - 31224
TELEFAX 03402 -31204

# CONTENTS

# 1. INTRODUCTION

## 1.1 MHD stability and mode structure near optimum $\beta$ values

The latest high-$\beta$ discharges produced at JET have reached values of $\beta$ close to the maximum attainable ones with respect to MHD stability as predicted by the Troyon limit to external kink modes and the Sykes-Wesson limit for ballooning modes. These values of $\beta$ were reached in double-null x-point configurations during the H-mode phase. Similar results were obtained in single-null discharges, although with reduced values of $\beta$. In view of the future pumped divertor upgrade of JET it is of interest to compare in detail discharges in double and single-null x-point configurations with respect to the MHD stability limits and to investigate the modes structure at high $\beta$.

The necessary numerical tools have recently been developed and applied to JET data. For the purpose of studying ideal ballooning and kink modes at high $\beta$, the numerical code HBT (for High-$\beta$ Tokamak) and its up-down asymmetric successor HBTAS have been installed at JET by G.T.A. Huysmans, R.M.O. Galvao, and J.P. Goedbloed [Huysmans89,90a,90b, and 91]. These codes have been extensively exploited in a systematic investigation of the ideal MHD $\beta$ limits under the contract JT9/9003. An extension of these studies to non-ideal modes and the possibility of discriminating between ideal and resistive modes was the next relevant step. This step could be made by means of the new resistive spectral code CASTOR (for Complex Alfvén Spectrum in TORoidal geometry), developed by W. Kerner, J.P. Goedbloed, S. Poedts, and E. Schwarz. This code solves for the full spectrum of resistive modes in toroidal geometry. Whereas HBT is based on ideal MHD, and has been specifically designed for fast parameter scans, CASTOR is based on resistive MHD and has the potential of incorporating other dissipative effects as well. Hence, it is important to operate the two codes in conjuction. The comparison of the computed normal modes with the experimental and diagnostic data should help detecting possible destruction of magnetic surfaces, which is the major effect of resistive instabilities. It should also be stressed that the experimental situation requires analysis of free-boundary modes.

## 1.2 Purpose of the investigations

With the above considerations in mind, we have carried out two main investigations, viz.:

i) extension of the new resistive spectral code CASTOR with an external vacuum and interfacing this code with the equilibrium identification code IDENTD;

ii) investigation of ballooning modes, edge localised modes, and resistive kink/tearing modes in high-$\beta$ and divertor discharges exploiting the numerical codes HBT and CASTOR.

In addition, it turned out to be necessary to develop an accurate, state-of-the-art equilibrium code to match the accuracy and flexibility of the CASTOR code. This code was called HELENA (for Hermite Elements Equilibrium solver for Normal-mode Analysis). Together, the two codes HELENA and CASTOR form a very powerful stand-alone tool to investigate resistive MHD phenomena in tokamaks.

Since these codes were also transformed into similarly powerful programs to study astrophysical problems, used by a group of scientists of the FOM-Instituut voor Plasmafysica (Nieuwegein, the Netherlands), the Astronomical Institute of the Katholieke Universiteit Leuven (Belgium), and the Max-Planck- Institut für Plasmaphysik (Garching, Germany), a set of extremely useful auxiliary tools used by this group were also installed at JET. This concerns the package REVISE, developed for the purpose of enabling the exchange of numerical programs which are in a constant state of development, and the plotting library PPPLIB (for Plasma Physics Plotting), which is a completely portable and very easy to use standard FORTRAN library containing all of the plotting routines needed in CASTOR.

Finally, during the course of the present investigations interest in a special class of modes arose, the so-called gap modes, which could very effectively be investigated by means of CASTOR and a special auxiliary code CSCAS (for Continuous Spectrum associated with CASTOR) developed by S. Poedts (associated with the Max-Planck-Institut für Plasmaphysik until 1/10/91) and W.O.K. Kerner. Since these modes offer an additional insight in the spectrum of magnetohydrodynamics, which is at the basis of all resistive phenomena of interest to JET, we decided to add this material to the report.

Whereas the stress of the main text of the report is on the physics embodied by the two points i) and ii) mentioned above, the description of the complete set

of numerical tools REVISE, PPPLIB, HELENA, CASTOR, and CSCAS is given in the appendices. Although this technical material is relegated to the appendices, it should be pointed out that the installation of these tools at JET facilitates an effective new way of collaboration between physicists at JET and in the associations.

### 1.3 Review of the report

In Section 2 the background material is given on the resistive MHD spectral calculations with the CASTOR code. Section 3 describes the computation of the equilibrium by means of HELENA.

To enable the calculation of free boundary resistive modes in axisymmetric toroidal equilibria, we have implemented the ideal and resistive boundary conditions at the plasma vacuum interface in the CASTOR code. The boundary conditions, their implementation, and the required solution of the vacuum magnetic field equations are described in Section 4.

In Section 5, we apply the numerical codes described in the Sections 2, 3 and 4. The first part of Section 5 deals with the pressure dependence of the tearing mode stability. A comparison is made between the pressure dependence of fixed and of free boundary tearing modes in a toroidal geometry. In the second part we investigate the influence of an X-point on the stability properties of resistive modes which are localized near the edge of the plasma.

In Section 6, the stability properties of actual JET discharges are analyzed. Here, we focus on the resistive stability of equilibria during the H-mode phase where edge localized modes (ELMs) have been observed and we try to establish the relevance of free boundary resistive modes.

Section 7 is concerned with another aspect of the MHD spectrum of tokamaks, viz. the damping of global Alfvén waves due to resonant absorption.

Finally, technical details and additional material on the computational procedures is found in the appendices.

# 2. LINEAR RESISTIVE MHD; NUMERICAL SOLUTION

## 2.1 Resistive MHD equations

One of the simplest self consistent models for the description of large scale motions of a hot plasma is given by the resistive magnetohydrodynamic (MHD) equations. In this model the plasma is described as a conducting fluid embedded in a magnetic field. The relevant variables for the description of the plasma behavior are the density, the pressure, the fluid velocity and the current density ($\rho, p, \boldsymbol{v}$ and $\boldsymbol{j}$) and the electric and magnetic field ($\boldsymbol{E}$ and $\boldsymbol{B}$). The time evolution of the system is determined by four fluid equations:
the continuity equation expressing the conservation of mass:

$$\frac{\partial \rho}{\partial t} + \nabla\cdot(\rho \boldsymbol{v}) = 0\,, \tag{2.1}$$

the momentum equation:

$$\rho \frac{d\boldsymbol{v}}{dt} = -\nabla p + \boldsymbol{j} \times \boldsymbol{B}\,, \tag{2.2}$$

the energy equation:

$$\frac{1}{\gamma - 1}\frac{\partial p}{\partial t} = -\frac{1}{\gamma - 1}\boldsymbol{v}\cdot\nabla p - \frac{\gamma}{\gamma - 1} p \nabla\cdot\boldsymbol{v} + \eta \boldsymbol{j}^2\,, \tag{2.3}$$

and Ohms law:

$$\eta \boldsymbol{j} = \boldsymbol{E} + \boldsymbol{v} \times \boldsymbol{B}\,. \tag{2.4}$$

The system is completed with three electromagnetic equations, Faraday's law, Ampere's Law and the condition on the divergence of $\boldsymbol{B}$:

$$\frac{\partial \boldsymbol{B}}{\partial t} = -\nabla \times \boldsymbol{E}\,, \tag{2.5}$$

$$\mu_0 \boldsymbol{j} = \nabla \times \boldsymbol{B}\,, \tag{2.6}$$

$$\nabla\cdot\boldsymbol{B} = 0\,. \tag{2.7}$$

Here, $\eta$ is the resistivity, $\mu_0$ is magnetic permeability, and $\gamma$ is the ratio of the specific heats. In the electromagnetic equations, the displacement current has been dropped. This eliminates electromagnetic waves from the system. Consistently, space charge effects are neglected in the momentum equation. The important difference with the ideal MHD equations is the $\eta \boldsymbol{j}$ term in Ohms law. The effect

of this term is to allow a finite electric field parallel to the magnetic field. This implies that the magnetic flux is not conserved and the magnetic field lines are allowed to break. We have neglected the ohmic dissipation in the energy equation. Other non-ideal terms, as for example a finite heat conductivity or viscosity, can be added to the equations but will not be discussed here.

The resistive equations as given by Eqs. (2.1) $-$(2.7) can be made dimensionless by normalizing the space coordinate, the magnetic field, the density, and the velocity:

$$\widetilde{R} = \frac{R}{R_M}, \quad \widetilde{\boldsymbol{B}} = \frac{\boldsymbol{B}}{B_M}, \quad \widetilde{\rho} = \frac{\rho}{\rho_M}, \quad \widetilde{\boldsymbol{v}} = \frac{\boldsymbol{v}}{V_A} \quad \text{with} \quad V_A^2 = \frac{B_M^2}{\mu_0 \rho_M}. \tag{2.8}$$

Here, $R_M, \rho_M$, and $B_M$ are the major radius, the density, and the toroidal field at the position of the magnetic axis. The velocity is normalized with the velocity of the Alfvén wave also on the magnetic axis. For the other quantities the normalization amounts to:

$$\widetilde{\boldsymbol{E}} = \frac{\boldsymbol{E}}{V_A B_M}, \qquad \widetilde{\eta} = \frac{\eta}{\mu_0 R_M V_A}, \qquad \widetilde{p} = \frac{\mu_0 p}{B_M^2},$$

$$\widetilde{\boldsymbol{J}} = \frac{\mu_0 R_M}{B_M} \boldsymbol{J}, \qquad \widetilde{t} = \frac{t}{\tau_A} \qquad \text{with} \qquad \tau_A = \frac{R_M}{V_A}. \tag{2.9}$$

Dropping the displacement current and the space charge effects changed the evolution equations of the electric field and the current density into expressions which determine $\boldsymbol{E}$ and $\boldsymbol{J}$ directly from the velocity and the magnetic field. Eliminating $\boldsymbol{E}$ and $\boldsymbol{J}$ from the system, we are left with four evolution equations and one condition on the magnetic field:

$$\begin{aligned}
\frac{\partial \rho}{\partial t} &= -\nabla \cdot (\rho \boldsymbol{v}), \\
\rho \frac{d\boldsymbol{v}}{dt} &= -\nabla p + (\nabla \times \boldsymbol{B}) \times \boldsymbol{B}, \\
\frac{\partial \boldsymbol{B}}{\partial t} &= \nabla \times (\boldsymbol{v} \times \boldsymbol{B}) - \nabla \times (\eta \nabla \times \boldsymbol{B}), \\
\rho \frac{\partial T}{\partial t} &= -\rho \boldsymbol{v} \cdot \nabla T - (\gamma - 1) \rho T \nabla \cdot \boldsymbol{v}, \\
\nabla \cdot \boldsymbol{B} &= 0.
\end{aligned} \tag{2.10}$$

where we have dropped the tildes of the normalized quantities. The pressure has been replaced by the temperature by using the ideal gas law $p = \mathcal{R}\rho T$. This is done for the convenience of future extensions like, for example, a finite heat conductivity.

The form of Eqs. (2.10) is not very suitable for the numerical calculation of the time behavior of a resistive plasma because the condition $\nabla \cdot \boldsymbol{B} = 0$ has to be treated separately from the other equations. The condition can be dropped if we use the vector potential

$$\boldsymbol{B} = \nabla \times \boldsymbol{A} \tag{2.11}$$

instead of $\boldsymbol{B}$ itself. The gauge is set by taking the scalar potential zero.

The set of equations (2.10) describes the full non-linear time evolution of a resistive plasma. The equations describing the linear stability are obtained by expanding the equations around an equilibrium. Substitution of

$$\begin{aligned} &\rho = \rho_0 + \rho_1(t), \qquad T = T_0 + T_1(t), \qquad \boldsymbol{v} = \boldsymbol{v}_1(t)\,, \\ &\boldsymbol{B} = \boldsymbol{B}_0 + \boldsymbol{b}(t)\,, \qquad \boldsymbol{A} = \boldsymbol{A}_0 + \boldsymbol{A}_1(t) \quad \text{with} \quad \boldsymbol{b}(t) = \nabla \times \boldsymbol{A}_1(t)\,, \end{aligned} \tag{2.12}$$

yields the equilibrium equations for a static equilibrium:

$$\nabla p_0 = (\nabla \times \boldsymbol{B}_0) \times \boldsymbol{B}_0\,, \qquad \nabla \times (\eta \nabla \times \boldsymbol{B}_0) = 0\,. \tag{2.13}$$

It is evident that, with the exception of some special cases, no static equilibrium can exist in resistive MHD. By assuming the equilibrium to be static, we ignore velocity terms of the order of the resistivity. This inconsistency can give rise to resistive modes with a growth rate of the order of the resistivity diffusion time, $\tau_R = R_M/\eta$. However, the growth rate of typical resistive instabilities scale with a fractional power of the resistivity, $\frac{1}{3}$ for resistive interchange modes and $\frac{3}{5}$ for tearing modes. So for the small $\eta$ values ($\eta \sim 10^{-8} - 10^{-9}$) relevant in present day tokamaks, the time scale of the diffusive modes is much slower than the time scale of the relevant instabilities.

The numerical solution of the ideal static equilibrium equations is discussed in detail in Chapter 3.

The equations describing linear perturbations of the equilibrium are obtained by substitution of Eq. 2.12 in Eq. 2.10 which yields:

$$\begin{aligned} \lambda \rho_1 &= -\nabla \cdot (\rho_0 \boldsymbol{v}_1) \\ \lambda \rho_0 \boldsymbol{v}_1 &= -\nabla(\rho_0 T_1 + \rho_1 T_0) \\ &\quad + (\nabla \times \boldsymbol{B}_0) \times (\nabla \times \boldsymbol{A}_1) - \boldsymbol{B}_0 \times (\nabla \times \nabla \times \boldsymbol{A}_1) \\ \lambda \rho_0 T_1 &= -\rho_0 \boldsymbol{v}_1 \cdot \nabla T_0 - (\gamma - 1) p_0 \nabla \cdot \boldsymbol{v}_1 \\ &\quad + 2\eta(\gamma - 1)(\nabla \times \boldsymbol{B}_0) \cdot (\nabla \times \nabla \times \boldsymbol{A}_1) \\ \lambda \boldsymbol{A}_1 &= -\boldsymbol{B}_0 \times \boldsymbol{v}_1 - \eta \nabla \times \nabla \times \boldsymbol{A}_1 \end{aligned} \tag{2.14}$$

where the time dependence of the linear perturbations is taken to be $\sim e^{\lambda t}$. The eigenvalue $\lambda$ can, in general, be complex.

The numerical solution of the eigenvalue problem of Eqs. (2.14), as implemented in the CASTOR code, is discussed in the next section.

## 2.2 The CASTOR code

In this section we will describe the methods used for the numerical solution of the resistive MHD eigenvalue problem as implemented in the CASTOR code [Kerner91]. The CASTOR code was developed by W. Kerner and J.P. Goedbloed. In CASTOR, the same numerical techniques are used as in an earlier code which solved the resistive MHD equations in a cylindrical geometry [Kerner85]. There, both the equilibrium and the eigenfunctions are a function of the radial coordinate only. In CASTOR, the linearized resistive MHD equations (2.14) are solved in a general toroidal geometry, where the equilibria are assumed to be axisymmetric. Due to this symmetry, the dependence on the toroidal angle can be described with one toroidal mode number, $u(R, Z, \phi) = u(R, Z)e^{in\phi}$. The eigenfunctions are essentially two dimensional.

We will start this section with a general description of the Galerkin method. Then the coordinate system, the discretization of the variables, and the resulting matrices are discussed. Finally, we will mention the methods used for the solution of the non-Hermitian matrix eigenvalue problem.

### 2.2.1 The Galerkin method

For the numerical solution of the eigenvalue problem (2.14) we rely on the Galerkin method [Strang and Fix 73, Schwarz 84]. This method, described below, can be considered to be the natural extension of the Ritz variational method to a more general class of equations including dissipative problems.

Defining the state vector:

$$\boldsymbol{U} \equiv [\rho_1, \boldsymbol{v}_1, T_1, \boldsymbol{A}_1] , \tag{2.15}$$

the system of equations (2.14) can be written in the matrix form:

$$\boldsymbol{L}\boldsymbol{U} = \lambda \boldsymbol{R}\boldsymbol{U} , \tag{2.16}$$

where $\boldsymbol{L}$ and $\boldsymbol{R}$ are differential operators. A weak form of Eqs. (2.16) is constructed by multiplying the set of equations (2.16) with an arbitrary test function $\boldsymbol{V}$ and

integrating over the domain of interest, the plasma interior:

$$\int \boldsymbol{V}\boldsymbol{L}\boldsymbol{U}dV = \lambda \int \boldsymbol{V}\boldsymbol{R}\boldsymbol{U}dV\,. \tag{2.17}$$

$\boldsymbol{U}$ is a solution of (2.16) in the weak sense, if Eq. (2.17) is satisfied for an arbitrary $\boldsymbol{V}$ satisfying the appropriate boundary conditions.

In CASTOR, we use the same functions for the test functions $\boldsymbol{V}$ in the weak form (2.17) as will be used in the discretization of $\boldsymbol{U}$. So, if the $k^{th}$ component of $\boldsymbol{U}$ is approximated by:

$$U^k \simeq \widetilde{U}^k = \sum_{j=1}^{N} a_j^k h_j^k(\boldsymbol{r}), \tag{2.18}$$

where $N$ is the total number of expansion functions, the following set of equations is obtained for the coefficients $a_j^k$:

$$\int \boldsymbol{h}_j \boldsymbol{L}\widetilde{\boldsymbol{U}}dV = \lambda \int \boldsymbol{h}_j \boldsymbol{R}\widetilde{\boldsymbol{U}}dV \qquad \text{for} \qquad j = 1, N\,. \tag{2.19}$$

The second order derivatives in the radial coordinate in $\boldsymbol{L}$ can, in the weak form, be reduced to first order derivatives by partial integration. This implies that the test functions $\boldsymbol{V}$ must satisfy the same essential boundary conditions as the solution vector $\boldsymbol{U}$ [Strang and Fix 73]. Since the weak form only contains first order derivatives, the essential boundary conditions will be conditions on the function values, whereas conditions on the first order derivatives will be natural boundary conditions. The natural boundary conditions must not be implemented in the test functions or the solution vector. They are implemented by substituting the conditions into the weak form.

### 2.2.2 The coordinate system

The behavior of the MHD equations in the direction normal to the flux surfaces is very different from the in-plane direction. The ideal MHD equations exhibit a singularity in the direction perpendicular to the flux surfaces. In resistive MHD these singularities are resolved but the modes still show large gradients near an ideal singular surface. So, for an accurate representation of the mode structure it is essential to use a coordinate system with a function of the flux as a radial coordinate. The two other coordinates can be chosen freely. Here, we take the two angular coordinates such that the magnetic field lines appear straight. This ensures that the $\boldsymbol{B}\cdot\boldsymbol{\nabla}$ operator is accurately represented [Harley90]. With this

choice we still have the freedom to choose one of the angular coordinates. If one of the angles is taken to be the usual toroidal angle $\phi$ of the $(R, Z, \phi)$ coordinate system, then the poloidal coordinate of the straight field line system, $\theta$, must be determined such that the field lines are straight in the $(\theta, \phi)$ plane, i.e.:

$$d\phi/d\theta = q(\psi). \tag{2.20}$$

The contravariant and covariant basis vectors are then defined by:

$$\begin{aligned} \boldsymbol{a}^1 &= \boldsymbol{\nabla} s, \qquad & \boldsymbol{a}_1 &= J\boldsymbol{\nabla}\theta \times \boldsymbol{\nabla}\phi, \\ \boldsymbol{a}^2 &= \boldsymbol{\nabla}\theta, \qquad & \boldsymbol{a}_2 &= J\boldsymbol{\nabla}\phi \times \boldsymbol{\nabla} s, \\ \boldsymbol{a}^3 &= \boldsymbol{\nabla}\phi, \qquad & \boldsymbol{a}_3 &= J\boldsymbol{\nabla} s \times \boldsymbol{\nabla}\theta, \end{aligned} \tag{2.21}$$

where the radial coordinate $s$ is given by $\boldsymbol{\nabla}\psi = f(s)\boldsymbol{\nabla} s$, $J$ is the Jacobian of the $(s, \theta, \phi)$ coordinate system. The metric coefficients $g^{ij}$ and $g_{ij}$ are given by:

$$\begin{aligned} g^{11} &= |\boldsymbol{\nabla} s|^2 & g_{11} &= \frac{J^2}{R^2}|\boldsymbol{\nabla}\theta|^2 \\ g^{12} &= \boldsymbol{\nabla} s \cdot \boldsymbol{\nabla}\theta & g_{12} &= -\frac{J^2}{R^2}\boldsymbol{\nabla} s \cdot \boldsymbol{\nabla}\theta \\ g^{22} &= |\boldsymbol{\nabla}\theta|^2 & g_{22} &= \frac{J^2}{R^2}|\boldsymbol{\nabla} s|^2 \\ g^{33} &= |\boldsymbol{\nabla}\phi|^2 = \frac{1}{R^2} & g_{33} &= R^2 \end{aligned} \tag{2.22}$$

In this coordinate system, a field line can be represented by:

$$\frac{dl_\phi}{dl_p} \equiv \frac{\sqrt{g_{33}}d\phi}{\sqrt{g_{22}}d\theta} = \frac{B_\phi}{B_p}, \tag{2.23}$$

where $B_\phi$ and $B_p$ are the physical components in the toroidal and poloidal direction. Using (2.20), we obtain an expression of the poloidal arclength in terms of the angle $\theta$:

$$dl_p = \frac{B_p}{B_\phi} Rq\, d\theta, \quad \text{or} \quad \theta = \int \frac{F}{q}\frac{1}{R|\boldsymbol{\nabla}\psi|}dl_p, \quad \text{where} \quad F = RB_\phi\,, \tag{2.24}$$

and an expression for the Jacobian:

$$J = \frac{fqR^2}{F}. \tag{2.25}$$

### 2.2.3 Projections and discretization

The variables used in the numerical solution of the eigenvalue problem are defined by the following definitions. For the velocity, the following representation is chosen:

$$\boldsymbol{v} = \frac{R^2}{J}\bar{v}_1\boldsymbol{a}_1 + \frac{R^2}{iJ}\bar{v}_2\boldsymbol{a}_2 + \frac{R^2}{if}\bar{v}_3\boldsymbol{B}\,. \tag{2.26}$$

The representation of the perturbed vector potential is basically covariant:

$$\boldsymbol{A} = -i\bar{A}_1\boldsymbol{a}^1 + \bar{A}_2\boldsymbol{a}^2 + \bar{A}_3\boldsymbol{a}^3\,. \tag{2.27}$$

The perturbed density and temperature are multiplied with $s$ :

$$\bar{\rho}_1 = s\rho_1\,, \qquad \bar{T}_1 = sT_1\,. \tag{2.28}$$

The eight variables $(\bar{\rho}_1, \bar{v}_1, \bar{v}_2, \bar{v}_3, \bar{T}_1, \bar{A}_1, \bar{A}_2, \bar{A}_3)$ are functions of both the $s$ and the $\theta$ coordinate. Each variable is approximated by a Fourier series in the $\theta$ coordinate and a finite element interpolation in the radial direction:

$$u_k(s,\theta,\phi) \simeq \widetilde{u}_k = \sum_{m,j,p} \alpha_{m,j}^{k,p}\, h_{p,k}(s - s_j)\,\mathrm{e}^{im\theta}\mathrm{e}^{in\phi}\,. \tag{2.29}$$

Here, $k$ labels the eight variables, $m$ labels the Fourier harmonics and $j$ is the index for the radial grid points. The index $p$ labels the different interpolating functions at one radial node. For example, for linear elements there would be only one interpolating function on each node, for cubic Hermite elements there are two functions.

For ideal MHD codes, it was found [Gruber and Rappaz 85] that the Alfvén continuum modes are not well represented unless a specific choice is made for the finite element discretization of the velocity perturbation. If the same type of elements are used for the three components, so-called spectral pollution can occur. Due to numerical errors, the Alfvén modes couple to the fast magneto- acoustic modes. This leads to spurious eigenvalues in the Alfvén continuum. The artificial coupling to the fast wave can be avoided by interpolating the $\bar{v}_1$ component with a finite element which is one order higher than for $\bar{v}_2$ and $\bar{v}_3$. If, for example, $\bar{v}_1$ is interpolated with linear finite elements, the $\bar{v}_2$ and $\bar{v}_3$ components should be interpolated with piece wise constant elements. This ensures that in the divergence of $\boldsymbol{v}$ the same order polynomials appear, such that the divergence of $\boldsymbol{v}$ can cancel exactly.

In CASTOR higher order elements are used. The variables that have to be differentiated, $\bar{v}_1, \bar{A}_2$ and $\bar{A}_3$, are represented with cubic Hermite finite elements such that both the variables and their derivatives are continuous. Quadratic elements are used for the other variables, $\bar{\rho}, \bar{v}_2, \bar{v}_3, \bar{T}$ and $\bar{A}_1$.

On an interval, $s_j < s < s_{j+1}$, the cubic Hermite elements are given by:

$$\begin{aligned} H_{j,1} &= -(\tfrac{1}{d})^3(s-s_{j+1})^2(3s_j - s_{j+1} - 2s)\,, \\ H_{j,2} &= (\tfrac{1}{d})^2(s-s_j)(s-s_{j+1})^2\,, \\ H_{j+1,1} &= (\tfrac{1}{d})^3(s-s_j)^2(3s_{j+1} - s_j - 2s)\,, \\ H_{j+1,2} &= (\tfrac{1}{d})^2(s-s_j)^2(s-s_{j+1})\,, \end{aligned} \tag{2.30}$$

where $d = (s_{j+1} - s_j)$. The quadratic elements are given by:

$$\begin{aligned} h_{j,1} &= (\tfrac{1}{d})^2 2(s-s_{j+1/2})(s-s_{j+1})\,, \\ h_{j,2} &= -(\tfrac{1}{d})^2 4(s-s_j)(s-s_{j+1})\,, \\ h_{j+1,1} &= (\tfrac{1}{d})^2 2(s-s_j)(s-s_{j+1/2})\,, \\ h_{j+1,2} &= 0\,. \end{aligned} \tag{2.31}$$

The zero fourth quadratic element is added so that cubic and quadratic elements can be treated the same in the code. The coefficients of the cubic Hermite elements interpolation are determined by the values of the function and the first derivative at the nodes, the coefficients of quadratic elements by the function values at the nodes and at the midpoint between the nodes.

$$\begin{aligned} f_c(s) &= f(s_j)H_{j,1}(s) + f'(s_j)H_{j,2}(s) \\ &\quad + f(s_{j+1})H_{j+1,1}(s) + f'(s_{j+1})H_{j+1,2}(s)\,, \\ f_q(s) &= f(s_j)h_{j,1}(s) + f(s_{j+1/2})h_{j,2}(s) + f(s_{j+1})h_{j+1,1}(s)\,. \end{aligned} \tag{2.32}$$

### 2.2.4 The matrices

Using the discretization of (2.29), and representing the equilibrium quantities in $JL^{\bar{k},k}$ as a Fourier series, the weak form of Eq. (2.19) can be written as:

$$\iiint h^j_{k,p} e^{-im\theta} \sum_{\bar{k},\bar{p},\bar{m},\bar{j}} \sum_{l} (JL^{\bar{k},k})_l e^{il\theta} \alpha^{\bar{k},\bar{p}}_{\bar{m},\bar{j}} h^{\bar{j}}_{\bar{k},\bar{p}} e^{i\bar{m}\theta} ds d\theta d\phi = \lambda(\mathrm{RHS})\,, \tag{2.33}$$

where $J$ is the Jacobian (Eq. 2.25) and $L^{\bar{k},k}$ is an element of the matrix $L$ as defined in Eq. 2.16. The $k^{th}$ equation is multiplied with the corresponding finite

element, i.e. the equations for $\rho_1, v_2, v_3$ and $T_1$ are multiplied with a quadratic element and the equations for $v_1, A_2$ and $A_3$ with a cubic Hermite element. The number of test functions, $h^j_{k,p} e^{-im\theta}$, is the same as the number of unknowns $\alpha^{\bar{k},\bar{p}}_{\bar{m},\bar{j}}$. The total number is $2 \times 8 \times M \times N_r$, where $M$ is the number of Fourier harmonics and $N_r$ the number of radial points. The right hand side of the equation, is similar to the left with the $L^{\bar{k},k}$ replaced by $R^{\bar{k},k}$.

After integration in the two angles $\theta$ and $\phi$ the weak form becomes :

$$\int h^j_{k,p} \sum_{\bar{k},\bar{p},\bar{m},\bar{j}} (JL^{\bar{k},k})_{(m-\bar{m})} \alpha^{\bar{k},\bar{p}}_{\bar{m},\bar{j}} h^{\bar{j}}_{\bar{k},\bar{p}} ds = \lambda (\mathrm{RHS}). \tag{2.34}$$

Due to the local basis of the finite elements, the integrand is nonzero only for neighboring grid points. At each grid point there are 2 different interpolating functions and $M$ harmonics. Because the equilibrium quantities in $(JL^{\bar{k},k})$, in general, contain many Fourier harmonics, the integrand is non-zero for every combination of $m$ and $\bar{m}$. The resulting structure of the matrices $A$ and $B$ is shown in Fig. A.1. For every radial interval, there is a full block (ZMA). Each of the four blocks in the ZMA matrix is again divided into 8 by 8 sub-blocks, 8 rows for each the equations and 8 columns for the different variables. Each sub-block contains the $M$ harmonics and 2 interpolating functions. The final form of the elements of the matrices $A$ and $B$ is given in Appendix A.2.

### 2.2.5 Boundary conditions

In deriving the matrix elements (A.1) – (A.16), the momentum equation and the equations for the vector potential have been partially integrated. This yields extra surface integrals over the plasma boundary. From the normal component of the momentum equation we obtain the boundary term:

$$\iint \boldsymbol{v}^* \cdot \boldsymbol{n}\, \Pi_1\, dS\,, \tag{2.35}$$

where $\Pi_1$ is the total perturbed pressure, $\Pi_1 = p_1 + \boldsymbol{B}_0 \cdot \boldsymbol{b}$ and $\boldsymbol{n}$ is the normal pointing out of the plasma boundary. The induction equation yields:

$$\iint \eta \boldsymbol{A}^* \times \boldsymbol{\nabla} \times \boldsymbol{A} \cdot \boldsymbol{n}\, dS\,. \tag{2.36}$$

The symbols $\boldsymbol{v}^*$ and $\boldsymbol{A}^*$ should not be mistaken for the complex conjugate of the physical variables $\boldsymbol{v}$ and $\boldsymbol{A}$. Instead they represent the test functions, i.e., the type of finite elements used in the construction of the weak form.

The resistive MHD equations are of sixth order in the radial coordinate. Thus, we need to specify six boundary conditions to fully determine the system. When the plasma is surrounded by an ideally conducting wall at the plasma boundary, the normal component of the velocity, the normal magnetic field, and the tangential electric field must go to zero at the wall:

$$\begin{aligned} \boldsymbol{v}\cdot\boldsymbol{n}\big|_{\text{wall}} &= 0\,, \\ \boldsymbol{B}\cdot\boldsymbol{n}\big|_{\text{wall}} &= 0\,, \\ \boldsymbol{E}\times\boldsymbol{n}\big|_{\text{wall}} &= 0\,. \end{aligned} \tag{2.37}$$

In terms of the variables used in the CASTOR code, the boundary conditions are:

$$\bar{v}_1\big|_{\text{wall}} = 0\,, \qquad \bar{A}_2\big|_{\text{wall}} = 0\,, \qquad \bar{A}_3\big|_{\text{wall}} = 0\,. \tag{2.38}$$

In the plasma center, the boundary condition are a consequence of the regularity conditions on axis:

$$\bar{v}_1\big|_{\text{axis}} = 0\,, \qquad \bar{A}_2\big|_{\text{axis}} = 0\,, \qquad \bar{A}_3\big|_{\text{axis}} = 0\,. \tag{2.39}$$

With an ideally conducting wall on the plasma boundary, all boundary conditions are essential boundary conditions. They must be applied to both the variables and the test functions. In CASTOR, the conditions are implemented by removing the rows and columns of the matrices corresponding to the variables and the test functions of $\bar{v}_1, \bar{A}_2$ and $\bar{A}_3$ at the wall and $\bar{v}_1, \bar{A}_2$ and $\bar{A}_3$ in the center. Note that the boundary terms of Eqs. (2.35) and (2.36) are zero in this case.

The boundary conditions in the case where the plasma is surrounded by a vacuum and an ideally conducting wall is discussed in Chapter 4.

### 2.2.6 The solvers

The Galerkin formulation of the resistive MHD eigenvalue problem, described in section 2.2.1, leads to a complex non-Hermitian matrix eigenvalue problem. For the numerical solution of this eigenvalue problem several solvers have been implemented. The numerical methods in non-Hermitian eigenvalue problems have been reviewed by Kerner [Kerner89].

The complete spectrum of eigenvalues can be calculated using the standard QR algorithm of the LINPACK library. A major disadvantage of the QR algorithm is that it transforms the banded matrices into full matrices. The corresponding memory requirements limit the application of the QR algorithm to relatively small

problems where the number of harmonics and radial grid points is low. In, for example, 32 Mwords of memory, the maximum number of Fourier harmonics times the number of radial points, $M \times N_r$, is about 175.

For the study of the stability of the eigenmodes, the complete spectrum contains far to much information and one is only interested in the one or two largest positive eigenvalues. In those cases, the inverse vector iteration algorithm can be used to calculate single eigenvalues. The vector iteration conserves the band structure and therefore allows much larger problems to be treated. The implementation of the algorithm in the CASTOR code requires roughly $6\times(16M)^2+9\times(16M))\times N_r$ Mwords of memory. So, 32 Mwords is sufficient for, for example, 101 radial points and 12 Fourier harmonics. For very large problems which do not fit into central memory, an 'out of core' solver is available which reads/writes parts of the matrices to disk. A disadvantage of the inverse vector iteration algorithm is that a fairly accurate initial guess has to be supplied in order to find an eigenvalue. In typical applications the initial guess must be given within a factor of two to three of the actual eigenvalue. In parameter studies, where the eigenvalue is determined as a function of, for example, the resistivity this is less of a problem.

# 3. THE EQUILIBRIUM

In the previous section, it was shown that in resistive MHD the equilibria cannot be static but must have a small but finite flow in order to satisfy the resistive equilibrium equations. When a static equilibrium is used for the calculation of the resistive eigenvalues, the influence of the inconsistency of the equilibrium on the eigenvalue will be of the order of $\eta$. Also, additional modes will arise, with eigenvalues scaling like $\eta^{-1}$ representing the resistive diffusion of the static equilibrium. However, the growth rates of typical resistive instabilities scale with a fractional power of the resistivity, and will, for small $\eta$, be much larger than the growth rate of the diffusive modes. For these modes, the influence of $\eta$ on the equilibrium is small and the equilibrium can be considered static. Since our interest is mainly the unstable side of the resistive spectrum of eigenmodes, we will, from here on, assume the equilibrium to be static.

In calculating the eigenmodes of a given equilibrium, the actual eigenvalue usually is the result of a cancellation of the stabilizing and destabilizing terms yielding an eigenvalue which is small compared to the equilibrium terms involved. For example, in calculating the stability of the $m/n = 1/1$ internal kink mode in a circular plasma, the growth rate is determined by equilibrium quantities which are of the fourth order in the inverse aspect ratio. Thus, for a reliable calculation of the growth rate, the accuracy of the equilibrium quantities must be very high. Especially near marginal stability, where the growth rates become very small, the minimum growth rate that can still be resolved is determined by the numerical accuracy of the equilibrium.

In this section, we will describe the method used for the numerical solution of the equilibrium equations [Huysmans90] for the purpose of calculating the equilibrium quantities needed in the toroidal resistive stability code CASTOR. It will be shown that using bicubic isoparametric Hermite finite elements in the solution of the equilibrium problem yields very accurate solutions. Adjusting the positions of the elements such that in the final solution the element boundaries coincide with flux surfaces greatly facilitates the calculation of the flux surface quantities needed for the stability calculations.

## 3.1 The Grad-Shafranov equation

The equations describing the static equilibrium of an ideal plasma are given

by force balance, Ampères law, and the condition of vanishing divergence of the magnetic field:

$$\boldsymbol{J} \times \boldsymbol{B} = \boldsymbol{\nabla} p, \qquad \mu_0 \boldsymbol{J} = \boldsymbol{\nabla} \times \boldsymbol{B}, \qquad \boldsymbol{\nabla} \cdot \boldsymbol{B} = 0\,. \tag{3.1}$$

In a toroidally symmetric configuration, the last equation allows for the introduction of a scalar field $\psi$ such that the magnetic field can be represented by

$$\boldsymbol{B} = \boldsymbol{\nabla}\psi \times \boldsymbol{\nabla}\phi + F\boldsymbol{\nabla}\phi, \tag{3.2}$$

where $\phi$ is the toroidal angle of the cylindrical $(R, Z, \phi)$ coordinate system (see Fig. 3.1) and $F$ is an arbitrary function. Since $\boldsymbol{B} \cdot \boldsymbol{\nabla}\psi = 0$, field lines lie on surfaces of constant $\psi$. The function $\psi$ represents the poloidal magnetic flux. The current density can then be written as

$$\boldsymbol{J} = -\Delta^* \psi \boldsymbol{\nabla}\phi + \boldsymbol{\nabla} F \times \boldsymbol{\nabla}\phi, \tag{3.3}$$

where the operator $\Delta^*$ is given by

$$\Delta^* \equiv R^2 \boldsymbol{\nabla} \cdot \frac{1}{R^2} \boldsymbol{\nabla}. \tag{3.4}$$

The well known Grad-Shafranov equation is obtained from force balance in the direction of $\boldsymbol{\nabla}\psi$:

$$\Delta^* \psi = -F \frac{dF}{d\psi} - R^2 \frac{dp}{d\psi}. \tag{3.5}$$

From force balance one can also derive that both $\boldsymbol{\nabla} p \times \boldsymbol{\nabla}\psi = 0$ and $\boldsymbol{\nabla} F \times \boldsymbol{\nabla}\psi = 0$, i.e., both $p$ and $F$ are a function of $\psi$ only.

The formulation of the equilibrium problem contains two trivial scaling parameters, viz. the vacuum magnetic field $B_0$ at the geometric center of the plasma and the scale length $a$, the minor radius of the plasma boundary. They provide the dimensions of the physical quantities but do not enter otherwise. Similarly, the total poloidal flux, $2\pi\psi_1$ only enters as a scaling parameter normalizing the $J_\phi$ and $B_\phi$ profiles. This scaling is accounted for by the parameter $\alpha = a^2 B_0/\psi_1$. The two profiles $p$ and $F$ are then normalized by

$$\bar{p}(\bar{\psi}) = \left(\frac{\alpha^2}{\epsilon B_0^2}\right) p(\psi), \qquad \bar{F}^2(\bar{\psi}) = \left(\frac{\epsilon\alpha^2}{a^2 B_0^2}\right)(F^2(\psi) - R_0^2 B_0^2), \tag{3.6}$$

where $\bar{\psi}$ is the normalised flux, $\bar{\psi} = \psi/\psi_1$, $R_0$ is the major radius of the plasma, $\epsilon = a/R_0$, and $\psi_1$ and is the poloidal flux at the plasma boundary. In addition,

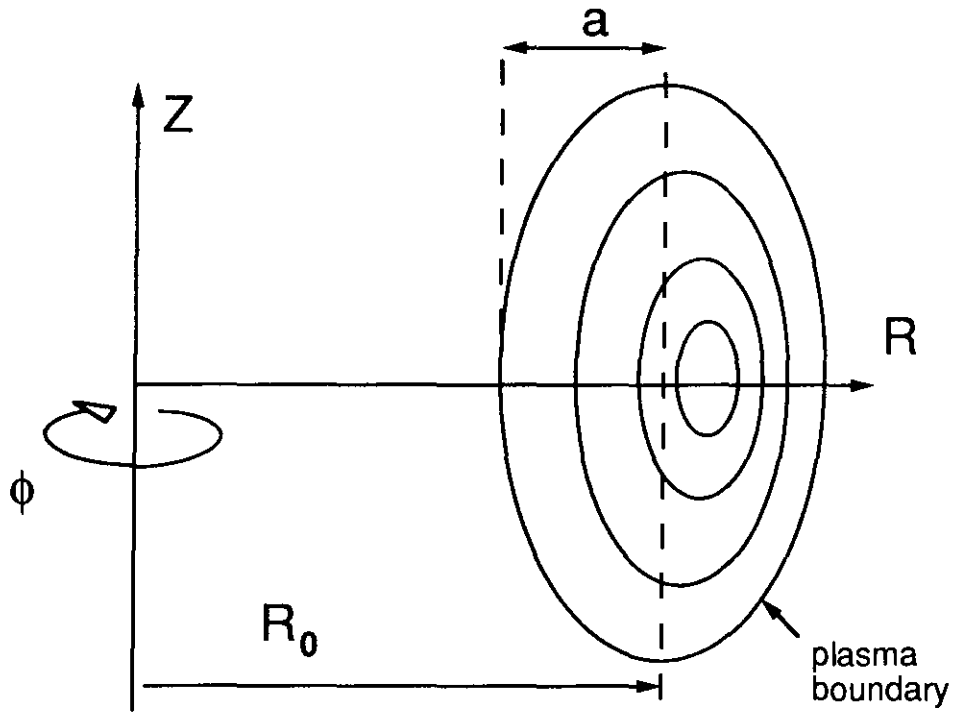


**Fig. 3.1** *The tokamak geometry.*

the $(R, Z)$ coordinate system is changed to a $(x, y)$ coordinate system centered in the plasma, where $x = (R - R_0)/a$ and $y = Z/a$.

In order to separate the shape of the two input profiles, $\bar{p}(\bar{\psi})$ and $\bar{F}\bar{F}'(\bar{\psi})$ from the amplitude, we define two unit profiles which are normalized to one on the magnetic axis ($\bar{\psi} = 0$):

$$\begin{aligned} \tfrac{1}{2}AB\Pi(\bar{\psi}) &= -\bar{p}'(\bar{\psi}) \\ A\Gamma(\bar{\psi}) &= -\frac{1}{\epsilon}\left(\bar{p}'(\bar{\psi}) + \bar{F}\bar{F}'(\bar{\psi})\right). \end{aligned} \tag{3.7}$$

The amplitudes of the two input profiles are given by the quantities $A$ and $B$. However, only $B$ is an input quantity. The value of $A$ is determined by the condition that $\bar{\psi} = 1$ on the plasma boundary. The definition of the $\Pi(\psi)$ and $\Gamma(\psi)$ profiles is the same as is used in the HBT equilibrium and stability code [Goedbloed81].

The boundary condition to be imposed on the solution of Eq. (3.5) depends on the type of application. In the stability calculation, no information is needed beyond the plasma boundary. In that case, the appropriate boundary condition

is $\bar{\psi}_B = 1$ where $\bar{\psi}_B$ is the flux at the boundary of the computational plane, the plasma boundary. In the problem of the reconstruction of an equilibrium given by some measurements of the flux and the poloidal field on a contour C outside the plasma (a free boundary problem) the boundary condition changes to $\psi_C = \Phi(\theta)_{\text{measured}}$. In the case of up-down symmetry in the poloidal plane, when the G-S equation has to solved only in the upper half of the $(x, y)$ plane, an additional condition appears along the x-axis: $\nabla\psi \cdot \boldsymbol{n} = 0$, where $\boldsymbol{n}$ points normal to the x-axis.

The solution, $\psi(R, Z)$, of the Grad-Shafranov equation (3.5) within a given shape of the plasma boundary and a given functional dependance of $\bar{p}$ and $\bar{F}$ on $\psi$, will describe the complete equilibrium. It can be shown that the solution $\psi(R, Z)$ consists of closed surfaces, which, for typical fusion plasma parameters, are centered around the magnetic axis, where $B_p = 0$.

The equilibrium quantities needed as input for the toroidal resistive eigenvalue code CASTOR are primarily the metric coefficients, $g^{ij}$, of the straight field line coordinate system $(s, \vartheta, \phi)$. The metric coefficients are given by:

$$\begin{aligned} g^{11} &= |\nabla s|^2\,, \qquad & g^{12} &= \nabla s \cdot \nabla \vartheta\,, \qquad & g^{33} &= \frac{1}{R^2}\,, \\ g^{22} &= |\nabla \vartheta|^2 = \frac{1}{g^{11}}\left(\frac{R^2}{J^2} + (g^{12})^2\right), \qquad & J &= \frac{fqR^2}{F}\,. \end{aligned} \tag{3.8}$$

The coefficients have to be calculated on a grid of $(s_i, \vartheta_j)$ values. The positions of these grid points can be calculated with:

$$s = \sqrt{\psi/\psi_1}, \qquad \vartheta(\theta) = \frac{F}{q}\int_{\psi} \frac{dl}{R|\nabla\psi|}. \tag{3.9}$$

Note that the definition of $s$ specifies the function $f$ in Eq. (2.21) as $f = 2s\psi_1$. The evaluation of the metric requires line integrals over surfaces of constant $\psi$ with $\nabla\psi$ in the integrand. Therefore, both $\psi$ and $\nabla\psi$ have to be known accurately. In the next section it is shown that using cubic Hermite elements both for the discretisation of the computational plane and for the solution $\psi$, yields a very accurate representation of $\psi$ and $\nabla\psi$ with a continuous representation of the field lines.

## 3.2 Isoparametric bicubic Hermite elements

The demands on the accuracy of the solution $\psi$ and $\nabla\psi$ suggest the use of a higher order finite element in order to avoid the very large number of elements and associated matrices which would be needed to obtain the required accuracy with, e.g., linear elements. Bicubic Hermite elements allow for a representation of $\psi(x,y)$ such that both $\psi$ and $\nabla\psi$ are continuous across element boundaries. The interpolating functions of the bicubic Hermite element are given by [Zienkiewicz71] :

$$\begin{aligned}
H_{00}(x,y) &= \frac{1}{16}(x+x_0)^2(xx_0-2)(y+y_0)^2(yy_0-2)\,,\\
H_{01}(x,y) &= -\frac{1}{16}x_0(x+x_0)^2(xx_0-1)(y+y_0)^2(yy_0-2)\,,\\
H_{10}(x,y) &= -\frac{1}{16}(x+x_0)^2(xx_0-2)y_0(y+y_0)^2(yy_0-1)\,,\\
H_{11}(x,y) &= \frac{1}{16}x_0(x+x_0)^2(xx_0-1)y_0(y+y_0)^2(yy_0-1),
\end{aligned} \tag{3.10}$$

where $x_0$ and $y_0$ are the coordinates of the four corners of a unit element (-1,-1), (-1,1), (1,1) and (1,-1). A function $f(x,y)$ inside the element is then approximated by:

$$\begin{aligned}
f(x,y) = \sum_{x_0,y_0} & H_{00}(x,y)f(x_0,y_0) + H_{10}(x,y)\frac{\partial f}{\partial x}(x_0,y_0)\\
& + H_{01}(x,y)\frac{\partial f}{\partial y}(x_0,y_0) + H_{11}(x,y)\frac{\partial^2 f}{\partial y\partial x}(x_0,y_0),
\end{aligned} \tag{3.11}$$

where the summation is over the four corners of the element. However, with the elements directly defined in $(x,y)$ coordinates it is impossible to approximate the shape of the plasma boundary accurately or even continuously. One way around this problem is to define the elements in a 'polar' coordinate system such that the plasma boundary coincides with a coordinate line [Lütjens90]. Another possibility, exploited here, is the use of an isoparametric mapping. This local approach allows for a more flexible placement of the nodes. The present approach is a generalization of [Kerner84], which was concerned with linear and quadratic elements, to bicubic Hermite elements.

With isoparametric elements the problem is formulated in a coordinate system $(s,t)$ which is local to each element (as illustrated in Fig. 3.2). In this element the solution $\psi$ and both original coordinates $x$ and $y$ are represented by the same

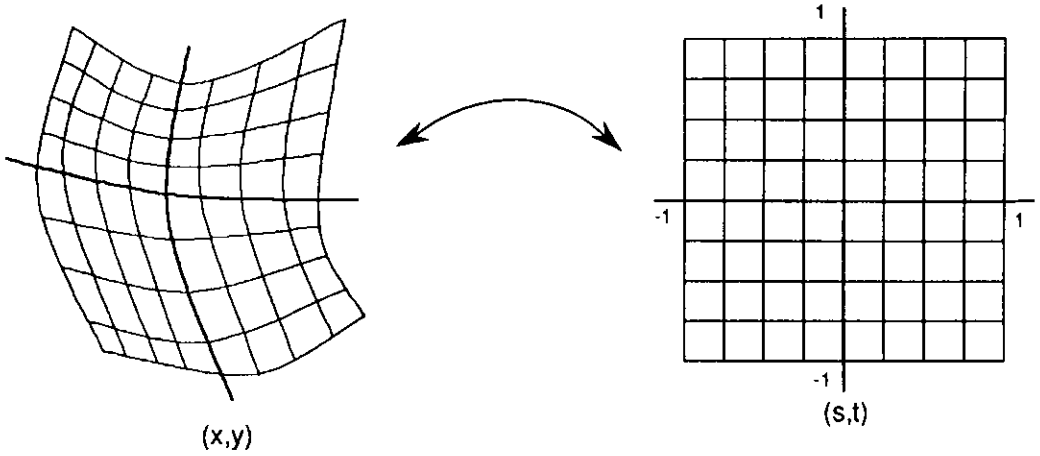


**Fig. 3.2** *The isopararametric mapping of one finite element.*

interpolating functions:

$$\begin{aligned}
\psi(s,t) &= \sum_{s_0,t_0} H_{00}\psi_{s_0,t_0} + H_{10}\frac{\partial\psi_{s_0,t_0}}{\partial s} + H_{01}\frac{\partial\psi_{s_0,t_0}}{\partial t} + H_{11}\frac{\partial^2\psi_{s_0,t_0}}{\partial s\partial t}\,, \\
x(s,t) &= \sum_{s_0,t_0} H_{00}x_{s_0,t_0} + H_{10}\frac{\partial x_{s_0,t_0}}{\partial s} + H_{01}\frac{\partial x_{s_0,t_0}}{\partial t} + H_{11}\frac{\partial^2 x_{s_0,t_0}}{\partial s\partial t}\,, \\
y(s,t) &= \sum_{s_0,t_0} H_{00}y_{s_0,t_0} + H_{10}\frac{\partial y_{s_0,t_0}}{\partial s} + H_{01}\frac{\partial y_{s_0,t_0}}{\partial t} + H_{11}\frac{\partial^2 y_{s_0,t_0}}{\partial s\partial t}\,.
\end{aligned} \tag{3.12}$$

In order to obtain a discretization of the computational $(x,y)$ plane in which $x$ and $y$ and their derivatives are continuous, all that is needed is a prescription of the values of $x, \partial x/\partial s, \partial x/\partial t$ and $\partial^2 x/\partial s\partial t$ (and similarly for $y$) at the nodes of the elements. In [Frind77] the length of the element boundary was used to estimate the values of $\partial x/\partial s$ and $\partial x/\partial t$. This, however, destroys the continuity of $\nabla\psi$ across the elements, leaving continuity only at the nodes.

A different approach, which is followed here, conserves all the good properties of the cubic Hermite element. We approximate the given radius of the plasma boundary by a Fourier series:

$$a_B(\theta) = \sum_m a_m e^{im\theta}\,, \tag{3.13}$$

where $\theta$ is a polar angle. With this boundary representation, a global coordinate system is constructed:

$$\begin{aligned}
x &= v(r)a_B(\theta)\cos\theta\,, \\
y &= v(r)a_B(\theta)\sin\theta\,,
\end{aligned} \tag{3.14}$$

where the radial coordinate $v$ is an arbitrary function ranging from 0 in the center to 1 on the boundary. By identifying the local coordinate $s$ with the global $v(r)$ coordinate, i.e. $s = s(v)$, and $t$ with $\theta$, the values of $\partial x/\partial s, \partial x/\partial t$ and $\partial^2 x/\partial s \partial t$ can be calculated. By this construction, $x$ and $y$ are continuously known in the poloidal plane. The resulting finite element discretization of the computational plane within a typical plasma boundary is shown in Fig. 3.3a.

## 3.3 Solution of the Grad-Shafranov equation

The Grad-Shafranov equation can now be solved using the Galerkin method (as in section 2.2.1). The weak form for the Grad-Shafranov equation is given by:

$$\iiint H_i \Delta^* \psi dV = \iiint H_i (-F\frac{dF}{d\psi} - R^2 \frac{dp}{d\psi}) dV \,. \tag{3.15}$$

With the discretisation of $x, y$, and $\psi$ of Eq. (3.12), this leads to a system of linear equations for each step of the non-linear iteration:

$$\boldsymbol{K}\psi_{n+1} = \boldsymbol{b}_n \,, \tag{3.16}$$

with

$$\begin{aligned} K_{ij} &= \iint H_i(s,t)\Delta^* H_j(s,t) J \, ds \, dt \\ &= -\iint \frac{1}{R} \nabla H_i(s,t) \cdot \nabla H_j(s,t) J \, ds \, dt, \\ b_i &= \iint \frac{1}{R} H_i [R^2 \bar{P}'(\psi_n) + \tfrac{1}{2} \bar{F}^{2\prime}(\psi_n)] J \, ds \, dt, \end{aligned} \tag{3.17}$$

where $J$ is the Jacobian $\partial(x,y)/\partial(s,t)$, and the functions $H_i$ are the interpolating functions. The boundary terms arising in the partial integration of the $\Delta^*$ operator in $\boldsymbol{K}$ vanish when the boundary conditions, $\psi_B = 1$ and $\nabla\psi \cdot \boldsymbol{n} = 0$, are applied. In this way the boundary conditions are implemented as natural boundary conditions.

The integration is done numerically using a 4 by 4 point Gaussian integration scheme. The resulting matrix $\boldsymbol{K}$ is positive definite and has a size of $4N_rN_p$ by $4N_rN_p$ where $N_r$ and $N_p$ are the number of radial and poloidal grid points, respectively. The matrix $\boldsymbol{K}$ consists of one main diagonal of width 16 and one off-diagonal, also of width 16 and separated by $4(N_p - 2)$ zeros. The structure of this matrix is partly spoiled when the boundary conditions are included in the matrix. The matrix is therefore stored without the boundary conditions in a compact form (storing only the non-zero elements).

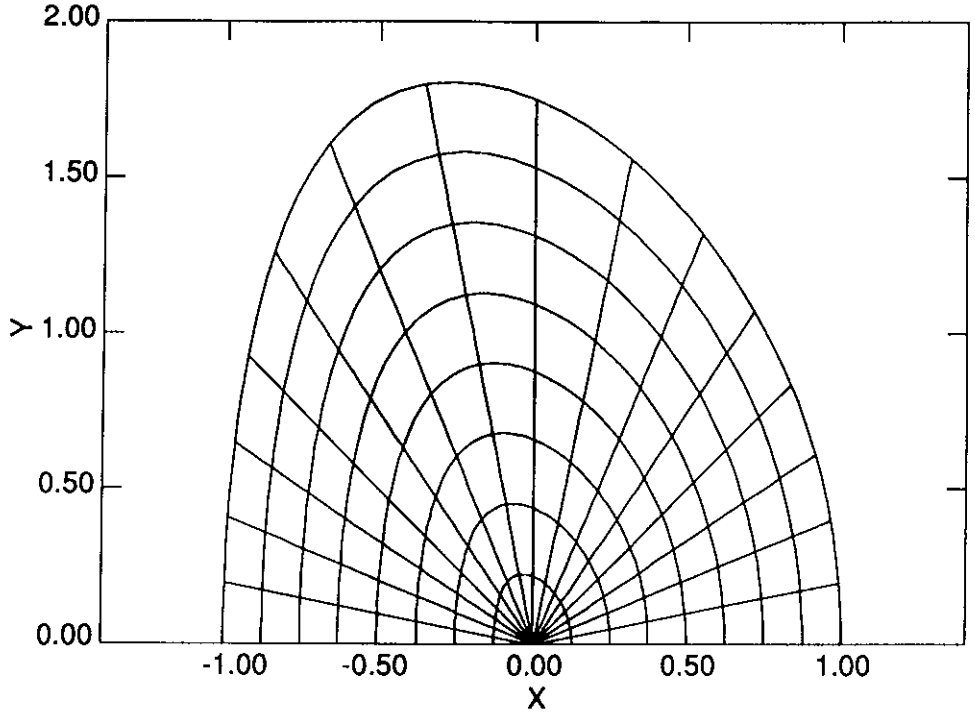


**Fig. 3.3a** *The initial 'polar' grid of bicubic isoparametric finite elements.*

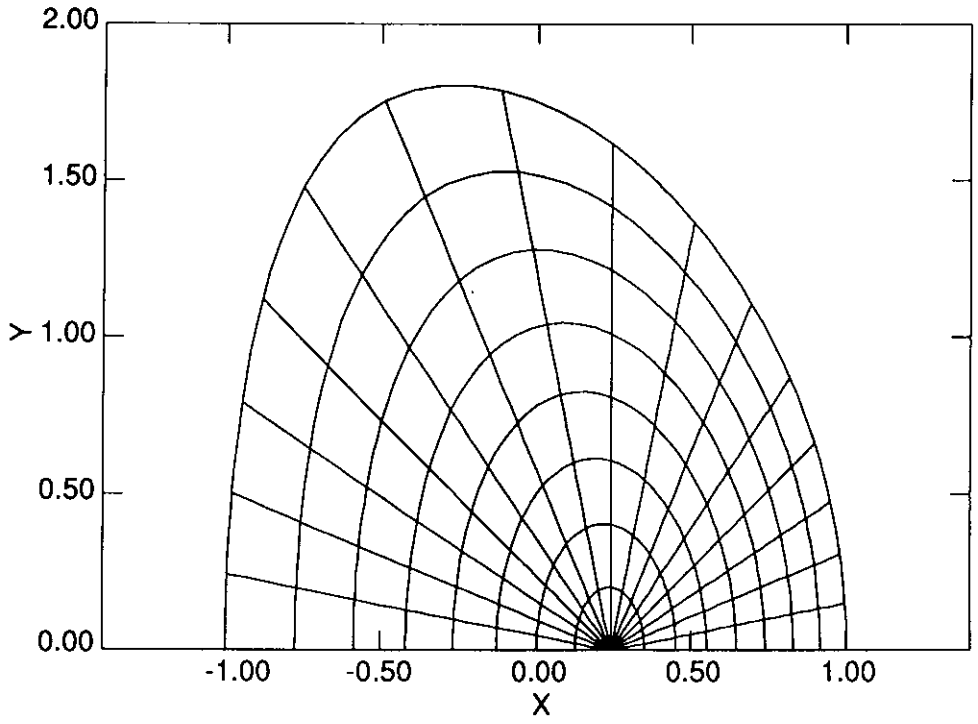


**Fig. 3.3b** *The final grid of elements aligned on flux surfaces.*

The set of linear equations is solved iteratively with a conjugate gradient method [Hageman81]. The matrix $\boldsymbol{K}$ is conditioned with its diagonal elements, which improves the convergence rate considerably. In the iterative solution only the inner product of $\boldsymbol{K}$ with a vector is needed. At each evaluation of an inner product the boundary conditions are included. The memory requirements are low: the code uses approximately $120N_rN_p$ words of memory. Another advantage of the iterative solution is that the solution of the previous step of the non-linear iteration can be used as a first estimate.

## 3.4 The mapping

A big advantage of the isoparametric mapping is that during the iteration of the non-linear Grad-Shafranov equation (3.5), the grid of finite elements can be adjusted to the non-converged solution obtained so far. If the local $s$ coordinate is identified with some function of $\psi$, the values of $\partial x/\partial s, \partial x/\partial t$ and $\partial^2 x/\partial s\partial t$ can be calculated from $\psi(x,y)$. The final solution will then have the finite elements aligned on the surfaces of constant $\psi$ and centered with respect to the magnetic axis. An example of a flux surface grid is shown in Figure 3.3b.

In this way, the result of the grid adjustment is an 'inverse' representation of the solution, i.e. both $x$ and $y$ are known as a function of $\psi$ and a poloidal angle $t$ instead of the usual representation of the solution $\psi$ as a function of $x$ and $y$. This greatly facilitates the calculation of the metric coefficients of the straight field line coordinate system $(s,\vartheta,\phi)$. To determine the positions of the grid points $(s_i,\vartheta_j)$ at which the metric is to be evaluated, the values of $\vartheta, \partial\vartheta/\partial s, \partial\vartheta/\partial t$ and $\partial^2\vartheta/\partial s\partial t$ are calculated at the finite element nodes of the flux surface grid. This is done by integrating over the known flux contours using four point Gaussian integration in each element. Given this, the angle $\vartheta$ is known in the whole poloidal plane using the finite element representation of Eq. (3.11). Finding the $\vartheta_j$ is thereby reduced to solving a third order polynomial equation for each $\vartheta_j$.

Another advantage of the flux surface grid is that the accuracy of the equilibrium can be locally improved by accumulating the radial grid points, for example near a rational $q$-surface. The locally improved accuracy is of importance for modes which are localized at a particular flux surface or depend critically on the local equilibrium quantities.

## 3.5 Test cases

As a first test case we calculated a so called Soloviev equilibrium [Soloviev75],

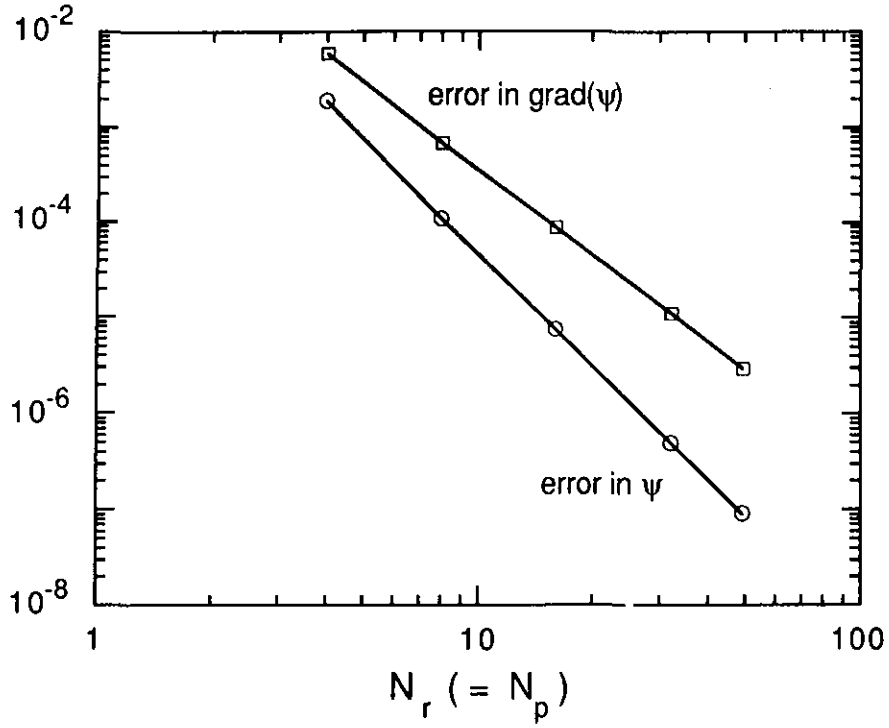


**Fig. 3.4** *The absolute error in $\bar{\psi}$ of the numerical Soloviev equilibrium ($E = 1.5, \epsilon = 0.25$) as a function of the number of radial intervals. The error is an average over 100 points in each element.*

and compared the numerical solution with the analytic expression. The Soloviev equilibria are analytic solutions of the Grad-Shafranov equation where the two equilibrium profiles $p'(\psi)$ and $FF'(\psi)$ are independent of $\psi$. The general up-down symmetric solution is given by:

$$\psi = \left(x - \tfrac{1}{2}\epsilon(1-x^2)\right)^2 + \left((1-\tfrac{1}{4}\epsilon^2)(1+\epsilon x)^2 + \lambda x(1+\tfrac{1}{2}\epsilon x)\right)\left(\tfrac{a}{b}\right)^2 y^2 \qquad (3.18)$$

where $x$ and $y$ are the normalized coordinates and $\psi$ is the normalized flux. The plasma boundary is given by $\psi(x,y) = 1$. The parameters $b/a$ and $\lambda$ are a measure of the ellipticity and triangularity of the plasma boundary. The inverse aspect ratio, $\epsilon$, is defined with respect to the geometric center of the plasma. Note that in the literature, the Soloviev equilibria are usually represented by $\epsilon_0$ and $E$, where $\epsilon_0$ is the inverse aspect ratio with respect to the magnetic axis. $\epsilon_0$ and $E$ are related to $\epsilon$ and $b/a$ through:

$$\epsilon_0 = \epsilon/(1+\epsilon^2), \qquad E = \left(\frac{b}{a}\right)/\sqrt{1-\tfrac{1}{4}\epsilon^2}\,. \qquad (3.19)$$

The Soloviev equilibrium used here is characterized by $E = 1.5$ and $\epsilon = 0.25$). The resulting error (an average error over many points) is shown in Fig. 3.4 as a

function of the number of radial elements, calculated with a polar grid. The convergence rate of the numerical solution $\psi(x,y)$, calculated with the isoparametric elements, is of the fourth order of the grid size, which is the same as for the usual cubic Hermite elements. This shows that no accuracy is lost by approximating the original $(x,y)$ plane through the isoparametric mapping. The convergence of $\nabla\psi(x,y)$ is of one order less than the solution itself, in accordance with the expectation for finite elements without the use of an isoparametric mapping.

The results shown here are obtained using an equidistant grid in both the radial and the angular coordinate. Especially for non-circular plasma boundaries, the errors can be reduced significantly (up to a factor 8 for this case) by using a non equidistant grid in the angular direction.

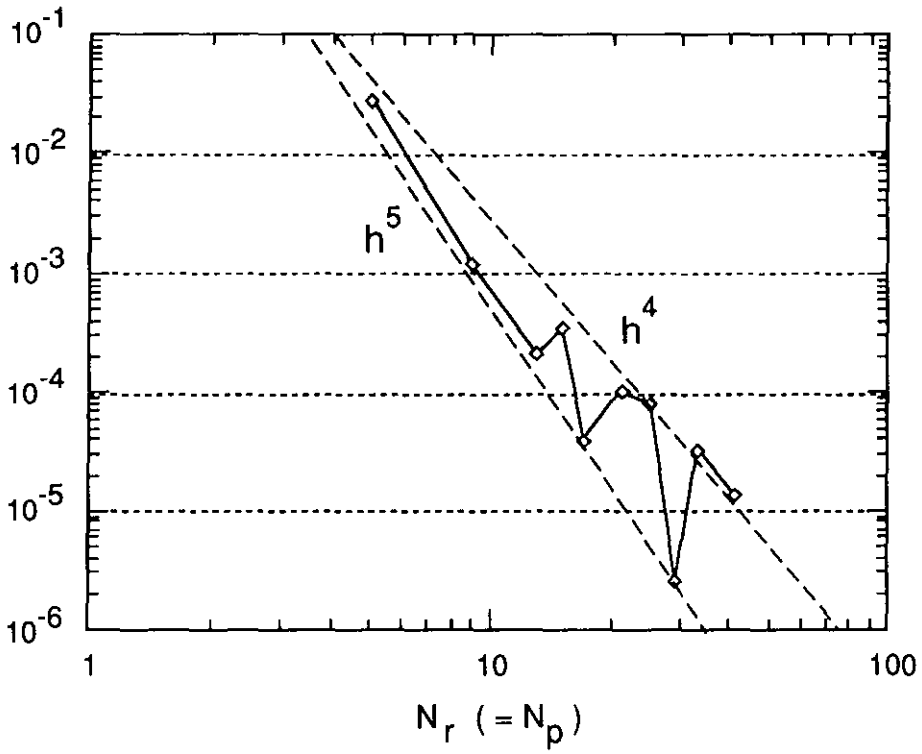


**Fig. 3.5** *The error of the growth rate of an $n = 2$ instability of a Soloviev equilibrium ($E = 2, \varepsilon = 1/3, q_0 = 0.6$) as a function of the number of finite elements in the equilibrium calculation. The scaling with the grid size, $h = (N_R - 1)^{-1}$, is indicated by the dashed lines.*

A more relevant test of the accuracy of the equilibrium quantities, that are used in the linear resistive stability code CASTOR, is to determine the sensitivity of the eigenvalues on the number of grid points of the equilibrium. For this, we have taken a Soloviev equilibrium ($E = 2, \epsilon = 1/3, q_{\text{axis}} = 0.6$) and calculated the

growth rate of an $n = 2$ instability as a function of the number of grid points of the equilibrium calculation. The eigenvalue was calculated using 5 harmonics in the poloidal direction and 51 radial grid points. The absolute value of the relative error of the resulting eigenvalues is shown in Fig. 3.5. The error is calculated using the value of the equilibrium with $51 \times 51$ grid points as a reference value. The error in the growth rate scales with the fourth power of the element size. The relative error as a function of the number of points is oscillating around zero: this causes the lower lying points in the graph. The graph shows that already with a coarse grid of $17 \times 17$ elements, the growth rate is converged up to four decimal places.

## 3.6 Conclusion

An equilibrium code has been developed for the purpose of calculating the metric coefficients of a coordinate system with the flux as a radial coordinate. It has been shown that bicubic Hermite elements yield a very accurate solution with relatively few finite elements. Through the use of an isoparametric mapping of the $(x, y)$ coordinate system, also using bicubic Hermite elements, a solution can be obtained with the finite elements aligned on flux surfaces. In the solution, both the flux and the derivatives of the flux are continuous in the $(x, y)$ plane. Here, it is used for the subsequent calculation of the metric coefficients required in the CASTOR code. However, many other applications can be imagined for the use of the isoparametric representation of a flux coordinate system. It may be useful, not only for the calculation of flux surface quantities, but also as an actual coordinate system to solve, for example, 2D transport or other MHD stability problems.

# 4. IMPLEMENTATION PLASMA-VACUUM BOUNDARY CONDITIONS

## 4.1 Boundary conditions

### 4.1.1 Ideal boundary conditions

The boundary conditions at the interface of an ideally conducting plasma and a surrounding vacuum are given by:

$$\boldsymbol{B}\cdot\boldsymbol{n} = \hat{\boldsymbol{B}}\cdot\boldsymbol{n} = 0\,, \tag{4.1}$$

$$p + \tfrac{1}{2}B^2 = \tfrac{1}{2}\hat{B}^2, \tag{4.2}$$

where Eq. (4.1) expresses the fact that field lines cannot point out of the plasma (i.e. the definition of the plasma boundary) and Eq. (4.2) expresses pressure balance across the boundary. The vector $\boldsymbol{n}$ is the normal of the plasma boundary. The vacuum variables are distinguished from the plasma variables by a hat. Since an ideally conducting plasma allows for an arbitrary surface current, there is no condition on the continuity of the tangential component of the magnetic field. The jump in the tangential field across the boundary merely defines the surface current:

$$\boldsymbol{n} \times (\boldsymbol{B} - \hat{\boldsymbol{B}}) = \boldsymbol{j}^{\star}. \tag{4.3}$$

The boundary conditions (4.1) and (4.2) are valid for an arbitrary stationary or moving plasma boundary, provided the actual values at the boundary are used. Here, however, we are interested in the linear stability of a given equilibrium and we need to rewrite the boundary conditions in terms of the equilibrium quantities and the perturbations. If the equilibrium is perturbed by a velocity field $\boldsymbol{v}(\boldsymbol{r})$, the value of an arbitrary plasma parameter at the perturbed boundary is approximated to first order by:

$$\boldsymbol{A} = \boldsymbol{A}_0 + \boldsymbol{A}_1 + \frac{1}{\lambda}\boldsymbol{v}\cdot\nabla\boldsymbol{A}_0, \tag{4.4}$$

where $\boldsymbol{A}$ is an arbitrary vector with index 0 for the equilibrium quantities and 1 for the linear perturbation. $\lambda$ is the eigenvalue as defined in sec. 2.1. The normal to the plasma boundary is given by:

$$\boldsymbol{n} = \boldsymbol{n}_0 + \frac{1}{\lambda}(\nabla\boldsymbol{v})\cdot\boldsymbol{n}_0 - \frac{1}{\lambda}\boldsymbol{n}_0\boldsymbol{n}_0\cdot(\nabla\boldsymbol{v})\cdot\boldsymbol{n}_0. \tag{4.5}$$

This leads to the following linearized boundary conditions at the perturbed boundary:

$$\boldsymbol{n}_0 \cdot \nabla \times (\boldsymbol{v} \times \boldsymbol{B}_0) - \boldsymbol{n}_0 \cdot \lambda \boldsymbol{b} = \boldsymbol{n}_0 \cdot \nabla \times (\boldsymbol{v} \times \hat{\boldsymbol{B}}_0) - \boldsymbol{n}_0 \cdot \lambda \hat{\boldsymbol{b}} = 0\,, \tag{4.6}$$

$$\lambda(p_1 + \boldsymbol{B}_0 \cdot \boldsymbol{b}) + \boldsymbol{v} \cdot \nabla(p_0 + \tfrac{1}{2} B_0^2) = \lambda \hat{\boldsymbol{B}}_0 \cdot \hat{\boldsymbol{b}} + \boldsymbol{v} \cdot \nabla(\tfrac{1}{2} \hat{B}_0^2), \tag{4.7}$$

where $\boldsymbol{b}$ is the magnetic field perturbation. The second part of Eq.(4.6) is just the ideal induction equation and, hence, trivially satisfied. Conditions (4.6) and (4.7) can be simplified if we ignore the physically less interesting equilibria with surface currents. In that case the equilibrium magnetic field is continuous across the boundary, $\boldsymbol{B}_0 = \hat{\boldsymbol{B}}_0$, and the pressure $p_0$ falls to zero at the boundary. The terms containing the velocity $\boldsymbol{v}$ both in Eq. (4.6) and Eq. (4.7) contain only derivatives of $\boldsymbol{B}_0$ in the plane of the plasma surface and are, therefore, continuous going from plasma to vacuum. This simplifies Eqs. (4.6) and (4.7) to

$$\boldsymbol{b} \cdot \boldsymbol{n}_0 = \hat{\boldsymbol{b}} \cdot \boldsymbol{n}_0, \tag{4.8}$$

$$p_1 + \boldsymbol{B}_0 \cdot \boldsymbol{b} = \hat{\boldsymbol{B}}_0 \cdot \hat{\boldsymbol{b}}. \tag{4.9}$$

From the evolution equation for the pressure,

$$\lambda p_1 = -\boldsymbol{v} \cdot \nabla p_0 - \gamma p_0 \nabla \cdot \boldsymbol{v}\,, \tag{4.10}$$

it is clear that for the equilibria without surface currents the Lagrangian pressure perturbation must vanish at the plasma boundary.

### 4.1.2 Resistive boundary conditions

The main change going from ideal to resistive boundary conditions is that surface currents are no longer allowed in the plasma perturbation. This changes the definition of the surface current of the ideal boundary conditions to two additional resistive boundary conditions:

$$\boldsymbol{B} \times \boldsymbol{n} = \hat{\boldsymbol{B}} \times \boldsymbol{n}. \tag{4.11}$$

Expressed in terms of the equilibrium magnetic field and a linear perturbation this gives:

$$\boldsymbol{n}_0 \times (\boldsymbol{b} + \frac{1}{\lambda} \boldsymbol{v} \cdot \nabla \boldsymbol{B}_0) = \boldsymbol{n}_0 \times (\hat{\boldsymbol{b}} + \frac{1}{\lambda} \boldsymbol{v} \cdot \nabla \hat{\boldsymbol{B}}_0). \tag{4.12}$$

For equilibria with zero current density at the plasma boundary $\nabla B_0$ is continuous and Eq. (4.12) reduces to the condition that the tangential perturbation of the magnetic field is continuous.

If this condition is satisfied, it follows that the magnetic perturbation parallel to the equilibrium magnetic field, $\boldsymbol{B_0}\cdot\boldsymbol{b}$, is also continuous. The pressure balance condition in the resistive case then reduces to

$$p_1 = 0. \tag{4.13}$$

However, this condition is trivially satisfied since we have assumed both $p_0$ and $\nabla p_0$ (as part of the total current) to be zero at the boundary, reducing Eq. (4.10) to Eq. (4.13). Thus, the pressure balance does not pose any boundary condition in this case and is replaced by the continuity of the tangential magnetic field perturbation.

The condition of the continuity of the normal component of the magnetic field does not change. But the condition that $\boldsymbol{B}\cdot\boldsymbol{n}$ equals zero, which was trivially satisfied in the ideal case by virtue of the ideal induction equation, now imposes an additional constraint. That is, the resistive induction equation must reduce to the ideal induction equation at the plasma boundary:

$$\boldsymbol{n_0}\cdot\eta\boldsymbol{j} = 0, \tag{4.14}$$

where $\boldsymbol{j}$ is the perturbed current density. Combination of Eq. (4.14) with the condition $\boldsymbol{n}\cdot\boldsymbol{J} = 0$ at the perturbed boundary, i.e.

$$\boldsymbol{n_0}\cdot\boldsymbol{j} + \boldsymbol{n_0}\cdot(\nabla \times \boldsymbol{v} \times \boldsymbol{J_0}) = 0, \tag{4.15}$$

yields a condition on the equilibrium current density at the plasma boundary:

$$\boldsymbol{J_0} = 0. \tag{4.16}$$

So, the choice of $\boldsymbol{J_0} = 0$ made in the first paragraph, appears to be a sufficient condition to obtain a consistent set of boundary conditions.

A consequence of $\boldsymbol{J_0}, \boldsymbol{n_0}\cdot\boldsymbol{j}$ and $p_1$ being zero at the boundary is that all the driving terms in the momentum equation are pointing normal to the plasma boundary. The velocity perturbation at the boundary of a resistive plasma will therefore have no tangential components.

The discontinuity of the tangential magnetic field at the plasma boundary in an ideally conducting plasma, is replaced by a rapid change of the tangential

field perturbations in a resistive boundary layer in order to connect continuously to the vacuum magnetic field. Consequently, the surface current density arising in the perturbation in ideal MHD, is now spread out in this layer. The behavior of the normal magnetic field perturbation is similar to the ideal situation since the continuity of this component does not depend on a finite resistivity. The change in the tangential components of the velocity perturbation is also taking place in the resistive boundary layer. The width of the resistive boundary layer decreases with $\eta$ as $\eta^{1/2}$.

## 4.2 Implementation of the boundary conditions

For *ideal* MHD the problem of implementing the plasma vacuum solution has been solved in a number of ways. For example, in the PEST code [Grimm76], a Green's function method is used. Here, one does not have to solve for the complete vacuum solution explicitly but complicated surface integrals arise over both the plasma boundary and the ideally conducting wall. In the ERATO code [Roy90], the problem is solved by artificially extending the domain in which the perturbed magnetic vector potential is calculated up to the wall. This allows an easy implementation of the boundary conditions but increases the size of the resulting eigenvalue problem. It also suffers from the fact that the divergence of the vector potential is not zero in the vacuum.

For *resistive* MHD, the boundary conditions change to a continuity condition on the total perturbed magnetic field. To implement the boundary conditions we have developed a formulation whereby both the ideal and the resistive boundary conditions are implemented as natural boundary conditions, i.e. they are automatically satisfied after minimization of the weak form. It will be shown that the ideal boundary conditions are retrieved by setting the resistivity to zero in the general resistive case. Moreover, the vacuum problem can be solved independently from the eigenvalue problem of the plasma interior. The method may be considered as an extension to a general toroidal geometry of the cylindrical analysis of the cylindrical resistive MHD code LEDA [Poedts89].

In the weak form formulation of the eight resistive MHD equations, as used in CASTOR (see chapter 2), two surface integrals appear as a result of partial integration of the momentum and the induction equation. The momentum equation contributes a boundary term to the weak form which is independent of the resistivity:

$$W_s^I = - \iint_S (\boldsymbol{v}^* \cdot \boldsymbol{n}_0)(p_1 + \boldsymbol{B}_0 \cdot \boldsymbol{b}) dS, \tag{4.17}$$

whereas the induction equation yields a purely resistive term:

$$W_s^R = \iint_S \eta(\boldsymbol{A}^* \times \boldsymbol{b})\cdot\boldsymbol{n}_0 dS. \tag{4.18}$$

By rewriting the ideal and resistive surface terms by introducing information of the vacuum solution and using the boundary conditions to connect the plasma solution with the vacuum solution, both the ideal and resistive boundary conditions can be implemented. We will start with the ideal conditions.

Using the pressure balance condition (4.9) of the ideal boundary conditions and the absence of equilibrium surface currents, $\boldsymbol{B}_0 = \hat{\boldsymbol{B}}_0$, Eq. (4.17) can be rewritten as:

$$W_s^I = -\iint_S (\boldsymbol{v}^*\cdot\boldsymbol{n}_0)(\boldsymbol{B}_0\cdot\hat{\boldsymbol{b}})dS. \tag{4.19}$$

If we now perturb the vacuum with a unit magnetic field perturbation at the plasma boundary, $\boldsymbol{b}\cdot\boldsymbol{n}_0 = \hat{\boldsymbol{b}}\cdot\boldsymbol{n}_0$, the response of the vacuum in terms of the parallel magnetic field perturbation, $\boldsymbol{B}_0\cdot\hat{\boldsymbol{b}}$, at the plasma boundary can be 'measured' with Eq. (4.19). Defining the vacuum response as:

$$\boldsymbol{B}_0\cdot\hat{\boldsymbol{b}} = \hat{\alpha}\ (\hat{\boldsymbol{b}}\cdot\boldsymbol{n}_0) \tag{4.20}$$

and rewriting Eq. (4.19) in terms of plasma variables, the ideal boundary term becomes:

$$W_s^I = -\iint_S \hat{\alpha}\ (\boldsymbol{v}^*\cdot\boldsymbol{n}_0)(\boldsymbol{b}\cdot\boldsymbol{n}_0)dS. \tag{4.21}$$

So, all information needed from the vacuum solution is the operator $\alpha$ at the plasma boundary. This quantity can be calculated independently from the solution of the plasma equations.

In cylindrical geometry, the different Fourier harmonics in the poloidal angle are not coupled and can be treated independently. The vacuum is then perturbed with one Fourier harmonic of $\hat{\boldsymbol{b}}\cdot\boldsymbol{n}_0$ yielding a response of the same Fourier harmonic in $\boldsymbol{B}_0\cdot\hat{\boldsymbol{b}}$. The vacuum response $\alpha$ is then a single constant which depends on the poloidal and toroidal Fourier harmonic and on the distance of the plasma boundary to the wall and can be expressed analytically in terms of Bessel functions.

In a general toroidal geometry, with an arbitrary shape of the plasma boundary and the wall, both the perturbation and the response at the plasma boundary can be arbitrary functions of the poloidal angle. The general vacuum perturbation

can then be taken as a series of independent perturbations, where one perturbation of the plasma boundary can be characterized, for example, by one Fourier harmonic (with all the other harmonics set to zero). The response of each independent perturbation $(\boldsymbol{b}\cdot\boldsymbol{n}_0)_k$ will again be an arbitrary function in the poloidal angle:

$$(\boldsymbol{B}_0\cdot\boldsymbol{b})_k = \sum_l \hat{\alpha}_{kl} e^{il\theta} (\boldsymbol{b}\cdot\boldsymbol{n}_0)_k. \tag{4.22}$$

Rewritten in Fourier components Eq. (4.19) reads:

$$W_s^I = -\iint_S \sum_m (\boldsymbol{v}^*\cdot\boldsymbol{n}_0)_m e^{-im\theta} \sum_{k,l} \hat{\alpha}_{kl}\, e^{il\theta} (\boldsymbol{b}\cdot\boldsymbol{n}_0)_k dS, \tag{4.23}$$

where all the information of the vacuum is now described by the vacuum response matrix $\hat{\alpha}$ , which is a function of the shape of both the plasma and the wall, and of the aspect ratio, the plasma wall distance, the toroidal mode number, and the equilibrium angular coordinate distribution at the plasma boundary.

Notice that in the derivation of Eq. (4.23) we have used both ideal boundary conditions. In this formulation, the pressure balance has become a natural boundary condition which will be satisfied automatically after minimization of the weak form including the boundary term. The continuity of $\boldsymbol{b}\cdot\boldsymbol{n}$ is satisfied by definition since the different Fourier components of $\boldsymbol{b}\cdot\boldsymbol{n}$ provide the amplitudes of the independent vacuum solutions.

The same procedure of rewriting the boundary term to implement the boundary condition as a natural boundary condition can be followed for the resistive boundary conditions. In the case of a finite resistivity the perturbed pressure, $p_1$, equals zero at the boundary and the pressure balance reduces to the continuity of the parallel magnetic field perturbation, $\boldsymbol{B}_0\cdot\hat{\boldsymbol{b}}$. This leaves expression (4.19) for the ideal surface term unchanged. This term is now used to implement the continuity of $\boldsymbol{B}_0\cdot\hat{\boldsymbol{b}}$. The resistive surface term, $W_s^R$, can be used to implement the continuity of the other tangential component of the perturbed magnetic field. In covariant components $W_s^R$ reads:

$$W_s^R = \iint_S \eta (A_2^* \hat{b}_3 - A_3^* \hat{b}_2) d\phi d\theta, \tag{4.24}$$

where we have used the continuity across the boundary of both tangential components $b_2$ and $b_3$. As in the ideal case, we define the vacuum response caused by a unit perturbation of the normal magnetic field, $\boldsymbol{b}\cdot\boldsymbol{n}$, now in terms of $b_2$ and $b_3$:

$$(b_3)_k = \sum_l \hat{\beta}_{kl} e^{il\theta} (\boldsymbol{b}\cdot\boldsymbol{n}_0)_k, \qquad (b_2)_k = \sum_l \hat{\gamma}_{kl} e^{il\theta} (\boldsymbol{b}\cdot\boldsymbol{n}_0)_k. \tag{4.25}$$

The Fourier components of the $\hat{\beta}$, $\hat{\gamma}$ and $\hat{\alpha}$ matrices are related through

$$\boldsymbol{B}_0 \cdot \boldsymbol{b} = \frac{F}{qR^2}(b_2 + qb_3) \tag{4.26}$$

and the normal component of the vacuum equations, $\nabla \times \boldsymbol{b} = 0$, at the plasma boundary:

$$\partial b_3/\partial\theta = \partial b_2/\partial\phi. \tag{4.27}$$

So, for the implementation of the boundary conditions in the CASTOR code, we need only one of the three vacuum response matrices. Only in the case of axisymmetric modes, $n = 0$, there is no relation between $b_2$ and $b_3$. In that case, the matrix $\hat{\beta}$ is zero and we have to use the matrix $\hat{\gamma}$. The final form of the resistive surface term is:

$$W_s^R = \iint_S \sum_{m,k,l} \eta(\hat{\beta}_{kl}(A_3^*)_m - \hat{\gamma}_{kl}(A_2^*)_m)(\boldsymbol{b}\cdot\boldsymbol{n}_0)_k e^{-i(m-l)\theta} dS. \tag{4.28}$$

## 4.3 The vacuum solution

In the previous section it was shown how the vacuum, and the plasma problem can be solved independently and what quantities are needed from the vacuum solution to solve the free boundary plasma problem. Here we will discuss the formulation of the vacuum problem in terms of the scalar potential and the numerical solution using cubic Hermite finite elements.

The perturbation of the magnetic field in the vacuum in between the plasma boundary and an ideally conducting wall, is described by the equations

$$\nabla \times \boldsymbol{b} = 0,$$

$$\nabla \cdot \boldsymbol{b} = 0. \tag{4.29}$$

Because of the linearity of these equations, no information of the equilibrium vacuum magnetic field is needed. The boundary condition at the plasma vacuum interface is determined by the independent unit perturbations driving the vacuum, as defined in the previous section:

$$\boldsymbol{b}\cdot\boldsymbol{n}_0 = e^{im\theta}. \tag{4.30}$$

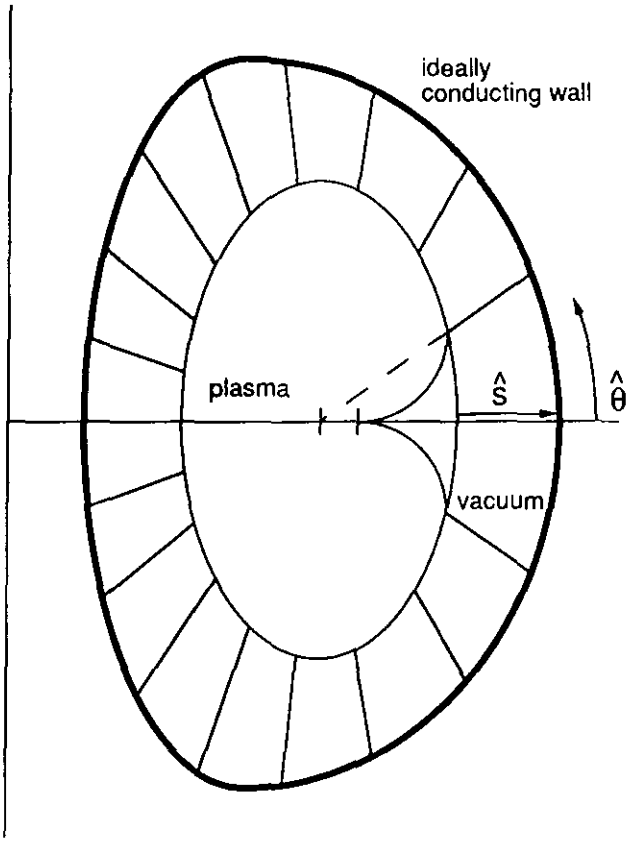


**Fig. 4.1** *The vacuum geometry, showing the arbitrarily shaped ideally conducting wall surrounding the plasma.*

At the ideally conducting wall, the normal component of the magnetic field must vanish:

$$\boldsymbol{b}\cdot\boldsymbol{n}_{\text{wall}} = 0. \tag{4.31}$$

The zero curl of $\boldsymbol{b}$ suggests the introduction of a magnetic scalar potential:

$$\boldsymbol{b} = \nabla\Phi, \tag{4.32}$$

reducing the four vacuum equations (4.29) to a single Laplace equation:

$$\nabla\cdot\nabla\Phi = 0. \tag{4.33}$$

For the numerical solution of Eq. (4.33) we use the standard weak form of the finite element method [Schwarz88]:

$$W_V = \iiint \Phi^*\nabla^2\Phi dV = -\iiint \nabla\Phi^*\cdot\nabla\Phi dV + \iint \Phi^*(\boldsymbol{b}\cdot\boldsymbol{n}_0)dS\,, \tag{4.34}$$

where the surface integral is over both the plasma boundary and the wall. The boundary term which contains the term $(\boldsymbol{b}\cdot\boldsymbol{n}_0)$ is perfectly suited to implement the boundary conditions of the vacuum problem as natural boundary conditions. The term arising from the wall vanishes and the term from the plasma boundary is determined by the unit perturbation of the vacuum. This term then yields the right hand side of the set of linear equations resulting from the minimization of $W_V$.

The coordinate system to be used in the vacuum must have both the plasma boundary and the wall as a radial coordinate surface. On the plasma boundary the vacuum poloidal angle coordinate is chosen to be the same as the plasma poloidal angle so that the continuity of $\boldsymbol{b}\cdot\boldsymbol{n}$ also holds for every Fourier component separately. This leads to the following coordinate system:

$$\hat{s} = \frac{r - r_p(\theta)}{r_w(\theta) - r_p(\theta)}, \qquad \hat{\vartheta} = \vartheta(\theta)\big|_{\text{plasma boundary}}, \tag{4.35}$$

where $(r, \theta)$ is the polar coordinate system centered at the geometric center of the plasma boundary. The functions $r_p$ and $r_w$ are the radius of the plasma boundary and the radius of the wall, respectively (see Fig. 4.1).

For the discretization of $\Phi$ we use Fourier harmonics in the poloidal angle, $\hat{\vartheta}$, and cubic Hermite finite elements, $H_1(\hat{s})$ and $H_2(\hat{s})$, in the radial coordinate:

$$\Phi(\hat{s}, \hat{\vartheta}) = \sum_{i,m} \left[\Phi^1_{im} H_1(\hat{s} - \hat{s}_i) + \Phi^2_{im} H_2(\hat{s} - \hat{s}_i)\right] e^{im\hat{\vartheta}}. \tag{4.36}$$

Minimization of the discretized $W_V$ with respect to $\Phi^*$ leads to a set of linear equations of which the matrix elements are given by:

$$\begin{aligned} A_{i,j} = & \int H_{k,p}\, H_{\bar{k},\bar{p}} \left(\bar{m} m (Jg^{22})_{(m-\bar{m})} + \left(\frac{n^2 J}{R^2}\right)_{(m-\bar{m})}\right) d\hat{s} \\ & + \int \frac{\partial H_{k,p}}{\partial s}\, H_{\bar{k},\bar{p}}\, i\bar{m} (Jg^{12})_{(m-\bar{m})}\, d\hat{s} \\ & + \int -H_{k,p}\, \frac{\partial H_{\bar{k},\bar{p}}}{\partial s}\, im\, (Jg^{12})_{(m-\bar{m})}\, d\hat{s} \\ & + \int \frac{\partial H_{k,p}}{\partial s}\, \frac{\partial H_{\bar{k},\bar{p}}}{\partial s} (Jg^{11})_{(m-\bar{m})}\, d\hat{s}, \end{aligned} \tag{4.37}$$

where $g^{ij}$ are the metric coefficients of the coordinate system (4.35). The labels $p$ and $\bar{p}$ label the two different cubic Hermite elements, the labels $k$ and $\bar{k}$ label the radial node of the element. The indices $i$ and $j$ are related to the Fourier components $m$ and $\bar{m}$, the $k^{th}$ and $\bar{k}^{th}$ radial grid point, and the element labels $p$

and $\bar{p}$ by $i = 2M(k-1) + 2(m-1) + p$ and $j = 2M(\bar{k}-1) + 2(\bar{m}-1) + \bar{p}$, where $M$ is the total number of Fourier harmonics.

To calculate the vacuum response matrix $\hat{\alpha}$, we have to calculate the response of each harmonic of the driving perturbation separately. So, we have to solve the system of equations, $\boldsymbol{A}\boldsymbol{x} = \boldsymbol{c}_m$, $M$ times. Each right hand side vector is equal to zero except for one element:

$$c_{2m_{\text{pert}}-1} = -(Jb^1)_{m_{\text{pert}}}. \tag{4.38}$$

where $Jb^1$ is set to 1 since we need only a normalized solution. Each vector $c$ yields one column of the vacuum response matrix:

$$\gamma_{m,m_{\text{pert}}} = m\Phi_m(\hat{s}=0), \qquad \beta_{m,m_{\text{pert}}} = n\Phi_m(\hat{s}=0). \tag{4.39}$$

The matrix of the system of equations is a block tridiagonal positive definite matrix with a band width of two times the number Fourier harmonics. The length of the diagonal is $2M$ times the number of radial points. The system is stored in band form, storing only the lower half of the matrix. The equations are solved by Gauss elimination. The decomposition of the $A$ matrix which is relatively expensive in CPU time, is independent of the $c$ vector and has to be done only once. To obtain the $M$ solutions a backward substitution has to be done for every $c$ vector.

## 4.4 Conclusion

In this section, we have described the boundary conditions for resistive free boundary modes in a general toroidal geometry. The boundary conditions have been implemented in the CASTOR code as natural boundary conditions, such that at zero resistivity the ideal boundary conditions are retrieved. The magnetic field perturbations in the vacuum are calculated independent from the plasma eigenvalue problem. The Laplace equation for the scalar potential in the vacuum is solved using a standard Galerkin method with a Fourier/finite element representation. This allows for an arbitrary shape of the ideally conducting wall, which can, for example, be used to determine the influence of an axisymmetric limiter close to the plasma boundary on the stability of free boundary modes.

Extensive tests of the free boundary CASTOR code have shown that ideal modes and cylindrical resistive modes are accurately reproduced. Details are given in Appendix B. Checking the resistive boundary conditions gives us confidence that the CASTOR code can now be used for the study of resistive free boundary modes in a general toroidal geometry.

# 5. STABILITY OF EXTERNAL RESISTIVE MODES

In the previous section we have described the boundary conditions at the plasma boundary of a resistive plasma surrounded by a vacuum and an ideally conducting wall. Also described in section 4 are the implementation of the solution of the vacuum problem and of the boundary conditions in the toroidal resistive MHD code CASTOR. Using the equilibrium mapping code HELENA, as described in section 3, to calculate the equilibria and the metric coefficients, we are now in the position to examine the stability of external or free boundary resistive modes in a general toroidal geometry. In section 5.1, we start with a short overview of the stability properties of external modes in the cylindrical approximation and recalculate some known results. In section 5.2, we present our results on the stability of free boundary modes in toroidal geometry. The influence of a low pressure is discussed and a comparison is made between the free boundary and fixed boundary tearing modes. In section 5.3, we examine the influence of an X-point plasma shape on the stability of free boundary modes, especially those localized near the plasma edge.

## 5.1 Cylindrical geometry

The simplest approximation of a toroidal tokamak is a straight cylinder with the additional constraint of periodicity along the cylinder axis. This is also called the straight tokamak. The constraint relates the length of the cylinder, $L$, to the major radius of the torus, $R$, and to the toroidal mode number, $n$: $L = 2\pi R/n$. Although, for example, the toroidal curvature can have a large effect on the stability properties, the periodic cylinder serves well to show the difference between the ideal and resistive external modes.

In *ideal* MHD, the stability of external modes of a pressureless cylindrical equilibrium is well known. The ideal mode is driven by the current density gradient at the edge. For a given poloidal mode number, $m$, this mode is unstable in a window of the edge safety factor, $q_1$, extending from $q_1 = m$ down to $q_M > m - 1$, where the actual value of $q_M$ depends on details of the current density profile and the distance between the plasma boundary and the ideally conducting wall. With increasing mode number, the mode gets more and more localized at the edge: the amplitude of the mode behaves like $(r - r_s)^{|m|-1}$, where $r_s$ is the radius of the rational $q$-surface. For large $m$, the stability of the mode is determined by the local

equilibrium quantities at the edge, so that it can be expressed by a local stability criterion [Laval74]. For equilibria with a finite current density at the edge, details of the profiles are not relevant and the instability window is determined by the edge current density, $J_1$:

$$\frac{1}{n}\Big(m - \frac{J_1}{\langle J\rangle}\Big) \le q_1 \le \frac{m}{n}, \tag{5.1}$$

where $\langle J\rangle$ is the average toroidal current density through the poloidal plane. In the more interesting case when the current density at the edge is zero, the stability is determined by the gradient of the current density at the edge, $J_1'$:

$$\frac{1}{n}\left[m - \exp\Big(\frac{2m\langle J\rangle}{aJ_1'}\Big)\right] < q_1 < \frac{m}{n}. \tag{5.2}$$

In this case, the unstable region shrinks exponentionally with increasing poloidal mode number and only the lower $m$ values ($2 \sim 4$) seem to be relevant. The same derivation of the stability condition (5.2) was used by [Laval74] to show the influence of a finite conductivity in the plasma. The effect was taken into account by allowing a jump in the normal component of the perturbation at the rational surface of the otherwise ideal solution. So in resistive MHD, the unstable window is symmetric around the rational $q_1$ value with the half-width given by the left-hand side of Eq. (5.2). The size of the unstable window is independent of the resistivity in this approximation. The growth rate of the modes at $q_1 > m/n$ scales with resistivity as $\eta^{3/5}$, the tearing mode scaling. At the $q_1 < m/n$ side, the growth rate is mainly determined by the ideal instability.

As an illustrative example, we have calculated the growth rates of a pressureless equilibrium with a circular boundary and $J_\phi = 1 - \psi(r)$. In Fig. 5.1, the growth rate of the ideal $m = 2$ mode is plotted versus $q_1$. This external mode is unstable in the window $1.6 < q_1 < 2.0$. Since in ideal MHD, reconnection of field lines can only take place in the vacuum region, the mode becomes stable when the rational $q$-surface moves into the plasma. With the *resistive* version of the external mode, reconnection can, of course, also take place with the rational surface inside the plasma. The driving term of the instability, the current density gradient at the plasma boundary, is unchanged. The resistive external mode will, therefore, be unstable in a larger window of $q_1$ values, extending the window at the larger $q_1$ values. This is shown in Fig. 5.1, by the upper curve, which represents the growth rate of the free boundary resistive mode for $\eta = 10^{-7}$. Instead of becoming stable, the mode now has a maximum growth rate at $q_1 = 2$. At the low $q_1$ side, the rational surface lies inside the vacuum so that resistivity does not give additional

freedom to the mode as compared to the ideal case and the position of $q_M$ is unchanged. The change in slope at $q_1 \simeq 2.3$ is caused by an unstable 'internal' tearing mode. The growth rate of the internal mode with the conducting wall onto the plasma boundary is shown for comparison.

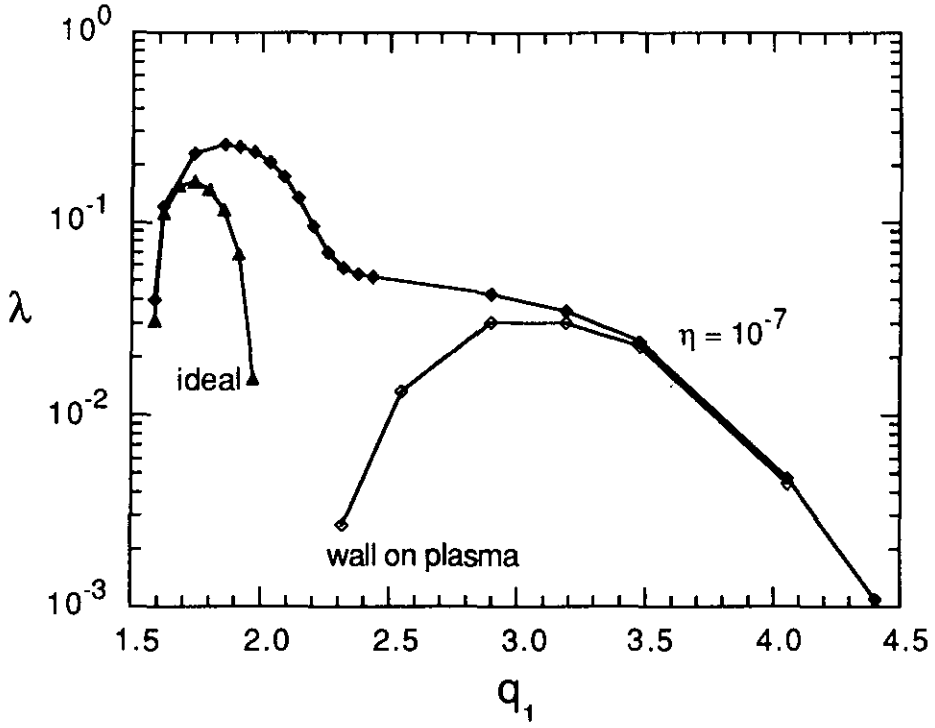


**Fig. 5.1** *The growth rate of a free boundary $m = 2$ tearing mode in a cylinder as a function of $q$ at the boundary. Also shown are the ideal external kink mode and the fixed boundary tearing mode.*

A necessary condition for the stability of ideal pressure driven interchange modes in a cylinder is given by the Suydam criterion:

$$-\frac{2p'}{rB_z^2} < \frac{1}{4}\left(\frac{q'}{q}\right)^2. \tag{5.3}$$

This criterion is a local stability criterion containing only local equilibrium quantities. Violation of the Suydam criterion gives rise to unstable modes which are very localized in the radial direction with an oscillatory behavior around the rational surface where $q = -m/n$. However, in ideal MHD, the oscillation theorem [Goedbloed74] states that, apart from the localized modes, the more dangerous global modes are also unstable, with a larger growth rate. The influence of resistivity on the local stability criterion is very large. It was shown by [Coppi63] that the localized resistive interchange modes are not stabilized by shear, i.e., the

right hand side of the Suydam criterion (5.3) is absent in the resistive case. This means that for typical tokamak plasmas, where the pressure gradient is negative everywhere, the resistive interchange mode is always unstable in a cylinder. As an example, we have examined the stability of the pressure driven interchange mode for the frequently used 'Wesson' equilibrium. The current density, the $q$-profile, and the pressure profile are given by:

$$\begin{aligned} j_z(r) &= j_0(1-r^2)^2\,, \qquad q(r) = \frac{4}{Rj_0\,(2-r^2)}\,, \\ p(r) &= \tfrac{1}{4}j_0^2\big((1-r^2) - \tfrac{3}{4}(1-r^4) + \tfrac{1}{6}(1-r^6)\big)\,, \end{aligned} \tag{5.4}$$

where $j_0$ is the current density on axis, and $R$ defines the periodicity length of the cylinder (i.e., the major radius of the torus). An equilibrium with $j_0 = 0.4$ and $R = 2.5$ is Suydam unstable in the region $0 < r < 0.54$, or $2 < q < 2.33$. The growth rate of the most unstable ideal $m = 4$ interchange mode versus $q_1$ for this equilibrium is shown in Fig. 5.2 (full curve). The Suydam unstable region is indicated by the black bar. It appears that, although the Suydam criterion is derived for localized modes, it also gives a good estimate of the stability window for the more unstable global $m = 4$ mode. This is not surprising since the global $m = 4$ mode is already rather localized around the rational surface. Adding resistivity to the plasma, the $m = 4$ interchange mode is unstable over the whole range of $q_1$ values as shown by the dashed curve in Fig. 5.2. The two curves show the growth rate of the mode with the conducting wall on the plasma and with the wall at infinity. With the rational surface moving towards the plasma boundary with decreasing $q_1$, the interchange mode slowly changes into a tearing mode in the free boundary case. This causes the sharp increase of the growth rate of the free boundary mode near $q_1 = 4$.

## 5.2 Toroidal geometry; Pressure dependence

The main difference between cylindrical and toroidal geometry is that the curvature of the magnetic field lines, instead of being constant on a flux surface, now has a 'good' curvature region on the inside of the torus and a 'bad' curvature region on the outside. The average curvature of the field lines in a torus is more favorable for stability than in a cylinder. Thus, the curvature will have a stabilizing effect on modes with low poloidal mode numbers such that the mode on average experiences a favorable curvature. In contrast with cylindrical geometry, the different poloidal harmonics can couple in toroidal geometry to form a mode which is localized on the outside of the torus in the region of unfavorable curvature where the pressure gradient is destabilizing. These are the so-called ballooning modes

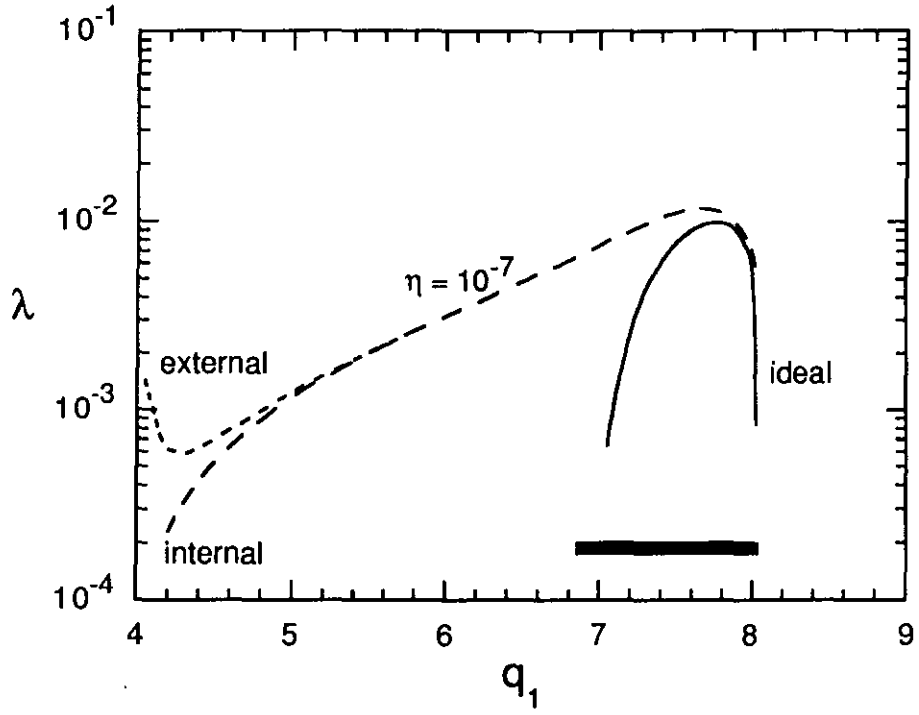


**Fig. 5.2** *The growth rate of the ideal and resistive $m = 4$ pressure driven interchange mode in a cylinder as a function of $q$ at the boundary. The black bar indicates the Suydam unstable range.*

In this section, the pressure dependence of current driven tearing modes is discussed. We will start with a short recapitulation of the analytic results of resistive layer theory [Glasser75] on the stabilizing influence of a finite pressure in a toroidal geometry. These results are given in the large aspect ratio low $\beta\,(\sim \epsilon^2)$ tokamak approximation as derived by [Glasser76, Hastie77] since this shows the relevant terms more clearly. It will then be shown (sec. 5.2.2 and 5.2.3) numerically that a finite pressure has a different influence on the stability of the external (free boundary) resistive modes as compared to that of the internal (fixed boundary) modes.

### 5.2.1 Analytic theory

A necessary stability condition for the ideal interchange modes in toroidal geometry is given by the well known Mercier criterion [Mercier60]. In the large aspect ratio, low $\beta$ approximation, it reads:

$$D_M < \tfrac{1}{4}\,, \quad D_M = \frac{2q^2}{B_0^2 r} p' \Big(1 - \frac{1}{q^2}\Big) \Big(\frac{q}{q'}\Big)^2 . \tag{5.5}$$

Compared to the cylindrical Suydam criterion, the additional term $(1-\frac{1}{q^2})$ provides stabilization due to the toroidal curvature if $q > 1$. In typical tokamak discharges,

the Mercier condition is usually satisfied in the region where $q > 1$ and $q'$ finite. Using the same ordering, the resistive version of the interchange condition is given by:

$$D_R < 0\,, \quad D_R = \frac{2q^2}{B_0^2 r} p' \Big(\frac{q}{q'}\Big)^2 \Big(1 - \frac{1}{q^2} + \frac{q}{r^3} q' \int_0^r d\tilde{r} \big(\frac{\tilde{r}^3}{q^2} - \frac{2R^2\tilde{r}}{B_0^2} p'\big)\Big). \qquad (5.6)$$

As in the cylindrical interchange condition, the term $\frac{1}{4}$ on the right-hand side of Eq. 5.5, representing the shear stabilization, does not survive in the resistive interchange condition. However, the additional integral term is stabilizing when $q' > 0$ and $p' < 0$. Thus, if $q > 1$, the resistive interchange condition is also satisfied, in contrast to the cylindrical case.

When the resistive interchange condition is satisfied, the stability of the tearing mode becomes important. It was shown by [Glasser75], that although the resistive layer is very small in the limit of small resistivity, the effect of the favorable average curvature cannot be neglected in a toroidal geometry. In combination with a finite pressure, the curvature has a large stabilizing influence on the tearing mode. The cylindrical stability condition $\Delta' < 0$ (see section 1.2) changes to:

$$\Delta' < \Delta_c, \qquad (5.7)$$

where, in general, $\Delta_c$ is a complicated function of the equilibrium parameters, and $\Delta'$ is the cylindrical driving term. In the bulk of the plasma, away from the plasma center and the plasma boundary, $\Delta_c$ may be approximated by:

$$\Delta_c = 1.54 \big(\frac{V_s}{X_0}\big) D_R^{5/6}, \qquad (5.8)$$

where $V_s/X_0$ is the ratio of the macroscopic scale length to the thickness of the resistive layer. In the large aspect ratio expansion, $V_s/X_0$ can be written as:

$$\frac{V_s}{X_0} = \left[\frac{1}{\rho}\Big(\frac{nB_0}{\eta R}\frac{q'}{q}\Big)^2 \Big/ \big(1 + 2q^2\big)\right]^{1/6}. \qquad (5.9)$$

This shows that the stabilization scales with $\eta^{-1/3}$ and will therefore be particularly pronounced at high temperatures.

In the case considered here, with $D_R > 0$, the tearing mode (also called the modified tearing mode) has two complex conjugate solutions. The real part of the eigenvalue changes sign at $\Delta' = \Delta_c$. At this point the mode is purely oscillatory.

At low pressure the approximation of Eq. (5.4) breaks down since a term, G, in $\Delta_c$ scaling as $\frac{1}{\gamma p}$ becomes very large. The expression for $\Delta_c$ has to be modified to:

$$\widetilde{\Delta}_c = 1.3|GD_R|^{-1/6}\Delta_c\,, \quad \text{with} \quad G = \frac{B_0^2}{\gamma p(1+2q^2)} \tag{5.10}$$

where $\Delta_c$ is the critical $\Delta$ as given by Eq. (5.8). Thus, at a low (local) pressure, as will occur near the edge of the plasma, the stabilization can be much less efficient.

In this formulation of the resistive stability of a plasma, the driving term of the instability, $\Delta'$, is determined by the cylindrical equilibrium approximation and is thereby independent of the pressure, the aspect ratio, or the resistivity. However, the driving term does depend on these equilibrium quantities and fully toroidal resistive calculations are needed to determine the resistive stability accurately. For fixed boundary (internal) resistive modes, the effects of a finite aspect ratio and pressure were studied numerically by [Hender89]. In the following sections, we will extend the numerical analysis to include the stability of free boundary (external) resistive modes using the CASTOR code (see chapter 2) with the extension of the vacuum as described in the previous chapter.

### 5.2.2 Numerical results, internal modes.

We will start this section with a typical example of the stabilization of an *internal* tearing mode by the good average curvature in combination with a finite pressure. To that end, we have calculated the eigenvalues of the $m/n = 2/1$ tearing mode. The equilibrium used for this calculation is given by an inverse aspect ratio of 0.25 and a circular plasma boundary. At zero pressure, the current density profile is given by the $\Gamma(\psi)$ profile (as defined by Eq. (3.7)), $\Gamma(\psi) = 1-\psi^2$. The total current is determined by the value of $q$ at the edge, $q_1 = 2.65$. In this pressureless case, the $m/n = 2/1$ tearing mode is unstable with a real growth rate which decreases with decreasing resistivity ($\sim \eta^{3/5}$) but the mode remains unstable for any value of $\eta$. This changes when we add even a small pressure. The normalized pressure profile used here is given by $\Pi(\psi) = 1 - \psi$, the total pressure is given by the poloidal $\beta$ of 0.26 where the poloidal $\beta$ is defined by:

$$\beta_p = \frac{8\pi S < p >}{I^2} \tag{5.11}$$

with $< p >$ the volume averaged pressure, $S$ the area of the poloidal cross section of the plasma, and $I$ the total toroidal plasma current. The resulting equilibrium profiles of the pressure, current density and $q$ are shown in Fig. 5.3.

The locus of the eigenvalue of the $m = 2$ tearing mode as a function of the resistivity is shown in Fig. 5.4. At high $\eta$ ($\eta = 10^{-6}$) the $m/n = 2/1$ tearing mode is still unstable with a real growth rate. Also drawn in the figure is the real eigenvalue of a less unstable branch. On this branch the eigenvalue increases with decreasing resistivity. As the resistivity is decreased further, the width of the resistive layer decreases and the stabilizing influence of the pressure becomes larger. At $\eta = 2.3. \times 10^{-7}$ the eigenvalue of the mode coalesces with the one of the lower branch and the two modes split into two overstable modes ($\mathrm{Re}[\lambda] > 0, \mathrm{Im}[\lambda] \neq 0$) which trace a curve in the complex plane. At $\eta = 4. \times 10^{-8}$, the mode stabilizes and the time behavior of the mode is purely oscillatory. As the resistivity is decreased still further, $|\lambda|$ goes to zero approaching the origin from the stable side as $\eta^{1/3}$, i.e., the interchange scaling.

Next, we examine the influence of the amplitude of the pressure profile and the radial position of the rational $q$ surface on the stability of the $m/n = 2/1$ tearing mode. The growth rate is calculated as a function of the total current for three values of the poloidal $\beta$, viz. $\beta_p = 0$, 0.13, and 0.26, using the same equilibrium profiles as before. By scanning the total current, the position of the rational surface changes from the plasma center at low current to the plasma edge

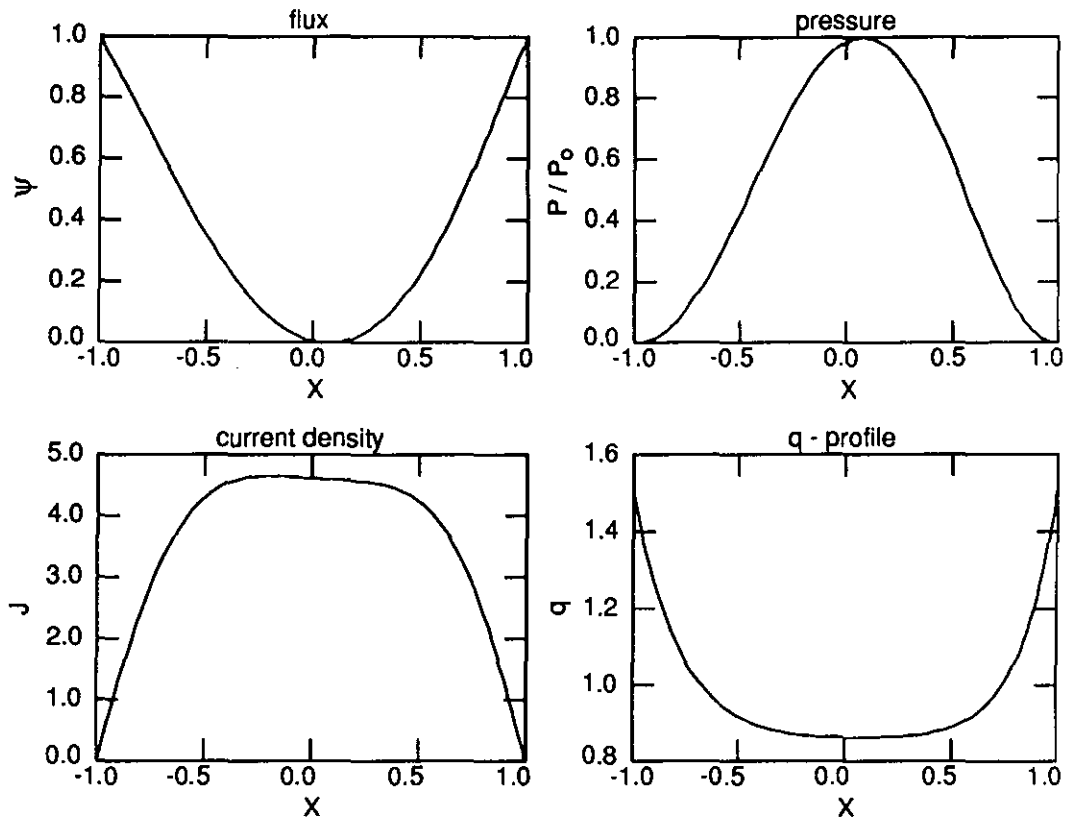


**Fig. 5.3** *The equilibrium profiles of the flux, the pressure, the toroidal current density, and the safety factor $q$ as a function the normalized minor radius (x).*

and the vacuum for the higher currents. The relative shape of the $q$-profile changes only marginally. While increasing the total pressure, we keep the $\Gamma(\psi)$ profile fixed. This means that the shape of the current density profile changes with increasing pressure. However, the pressures considered in this section are rather small and the current density profile is mainly determined by the $\Gamma(\psi)$ profile. At $\beta_p = 0.26$, the contribution of the $\Pi(\psi)$ profile to the current density is about 20%. If we had taken the more commonly used representation of the current density in terms of the $FF'$ profile, the changes in the current density would have been much larger.

The equilibria are characterized by a very broad current density profile such that there is only one rational surface inside the plasma for the range of currents considered. Consequently, no coupling can occur to other modes. The resulting growth rates of the $m/n = 2/1$ tearing mode for the three different pressures are shown in Fig. 5.5. The eigenvalues are calculated using 5 Fourier harmonics ranging from 1 to 5, and 101 radial grid points. The eigenvalues are plotted versus the value of $q$ at the plasma boundary, which is inversely proportional to the total current. The resistivity in this calculation is $10^{-6}$.

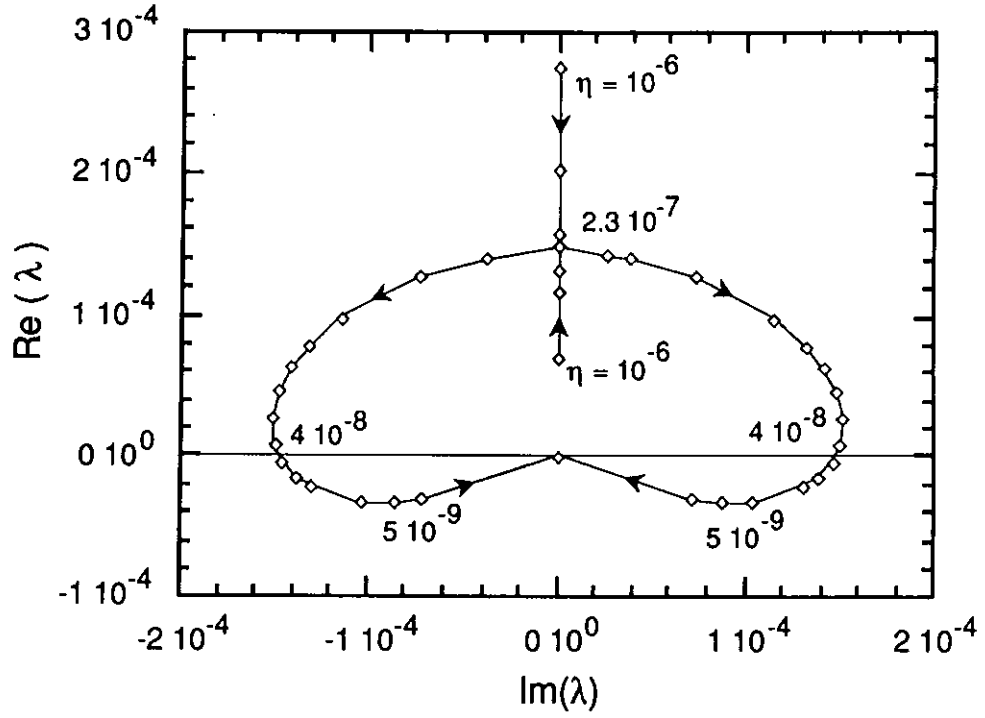


**Fig. 5.4** *The locus of the eigenvalue in the complex plane of an internal $m/n = 2/1$ tearing mode as a function of the resistivity.*

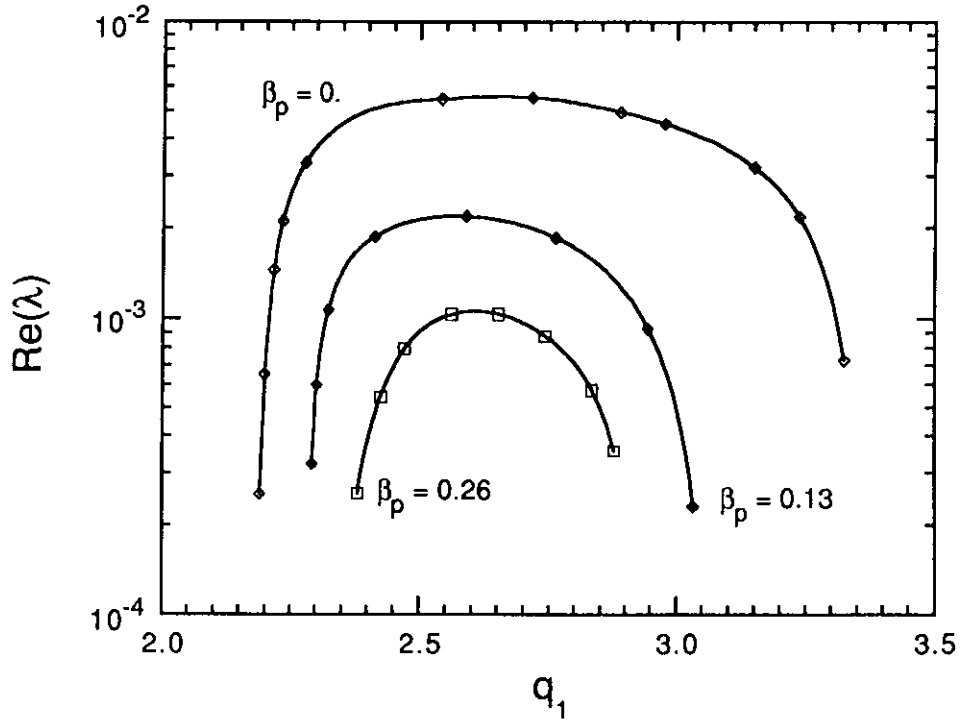


**Fig. 5.5** *The growth rate of an internal $m/n = 2/1$ tearing mode as a function of $q_1$ for three values of the poloidal beta. The resistivity is $10^{-6}$.*

At zero pressure, the mode is unstable in the window, $2.2 < q_1 < 3.35$. At the low $q_1$ side, where $q_1 < 2.2$, the 2/1 mode is stabilized by the ideally conducting wall which forces the normal component of the velocity and the magnetic field component to be zero. This marginal $q_1$ is independent of the resistivity. Only for high resistivity ($\eta > 5.10^{-6}$) when the layer width is of the order of the distance of the rational surface to the wall, the mode is becoming more stable with increasing resistivity. At the high $q_1$ side, the mode is unstable up to the point where the $q = 2$ surface coincides with the plasma center.

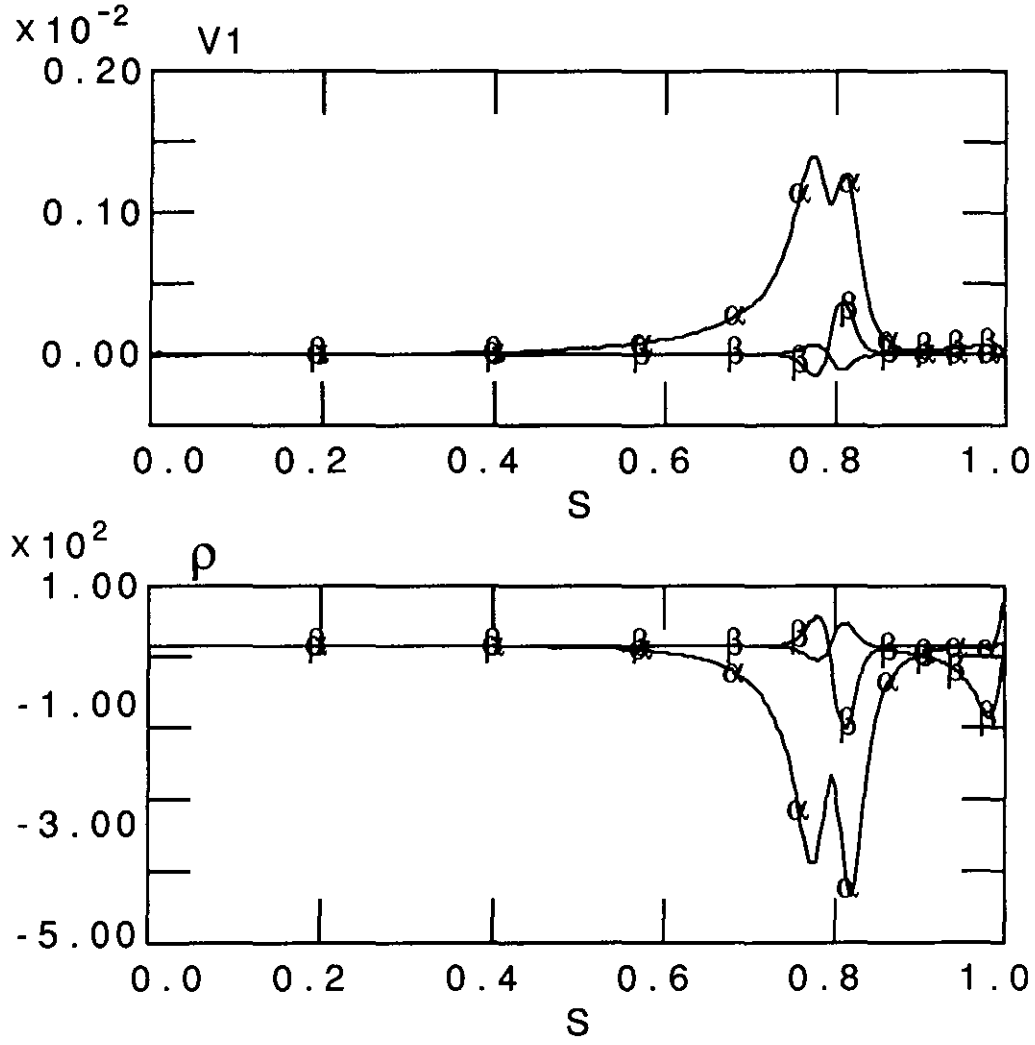


**Fig. 5.6** *The $m = 1, 2$, and 3 harmonics of the normal component of the velocity, and the density perturbation of an internal $m/n = 2/1$ tearing mode near marginal stability as a function of the radial coordinate, $s$. The $m = 2$ and 3 harmonics are indicated by $\alpha$ and $\beta$.*

When the pressure is increased, both the size of the unstable window in $q_1$ and the maximum growth rate become smaller. The stabilization is most pronounced at the high $q_1$ side because the driving force, the current density gradient, is smaller in the plasma center. The different components of the eigenmode near marginal stability at $q_1 = 2.89$ and $\beta_p = 0.26$ are plotted in Fig. 5.6. It shows the first three Fourier harmonics of the component of the perturbed velocity normal to the flux surfaces ($v_1$), and the density perturbation ($\rho_1$). Since we have taken the equilibrium density profile constant, the density perturbation equals the divergence of the velocity perturbation and is, therefore, a good measure of the plasma compression caused by the mode. Along the horizontal axis, the radial coordinate $s(= \sqrt{\psi})$ is plotted, where $s = 0$ on the magnetic axis and $s = 1$ at the plasma boundary. Notice that the $m = 2$ harmonic of $v_1$ develops a minimum at the $q = 2$ surface. This is seen more clearly on the density perturbation. This local minimum becomes smaller with decreasing growth rate and is characteristic for the mode near marginal stability [Harley 91] in the case of a compressible plasma ($\gamma = 5/3$).

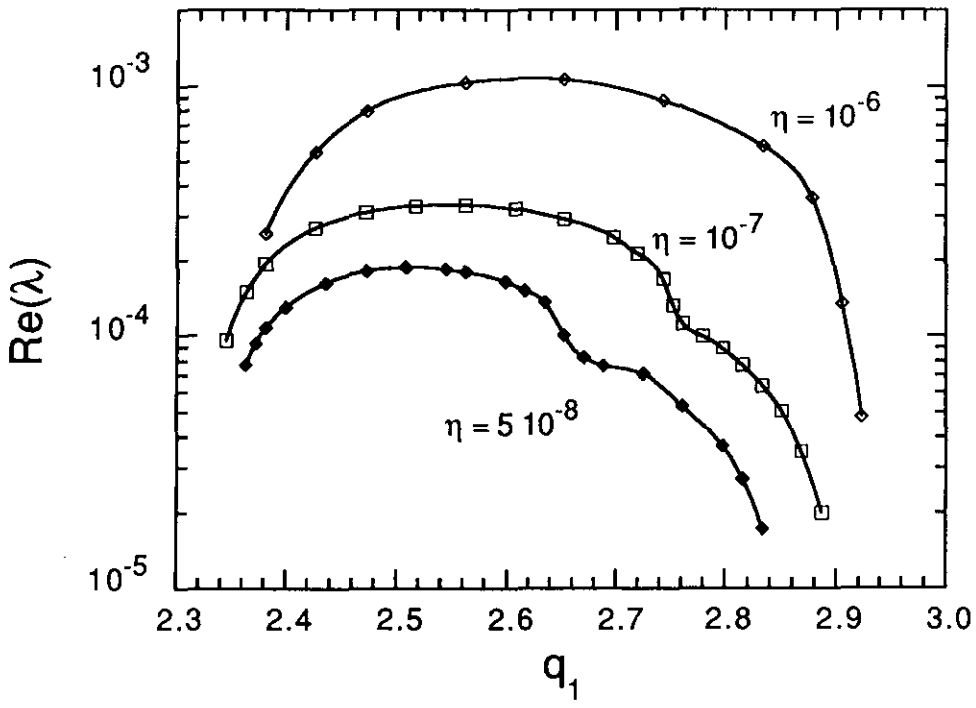


**Fig. 5.7** *The growth rate of an internal $m/n = 2/1$ tearing mode as a function of the value of $q$ at the edge, for three different values of the resistivity. The poloidal $\beta$ is 0.26.*

At first sight, it is not completely clear whether the stabilization of the

$m/n = 2/1$ mode is due to the good average curvature or is simply caused by the small changes of the current density profile. To show this more clearly we calculated the growth rates as a function of $q_1$ at a pressure of $\beta_p = 0.26$ for three different values of the resistivity, viz. $\eta = 10^{-6}, 10^{-7}$, and $5 \times 10^{-8}$. The results are shown Fig. 5.7. The upper curve for $\eta = 10^{-6}$ is identical to the lower curve of Fig 5.5. It is seen that reducing the resistivity, apart from the usual reduction of the growth rate, has only a small stabilizing effect (i.e., a change of sign of the eigenvalue). However, the figure does show that for $\eta$ smaller than $10^{-6}$, the 2/1 mode is stabilized through the average curvature effect. For $\eta$ larger than $10^{-6}$ the position of the marginal point is independent of the resistivity. So, in that case the lower growth rates at $\beta_p = 0.26$ are not caused by the curvature. This is also clear from the fact that at $\eta = 10^{-6}$ the mode is not becoming overstable near the marginal point. This in contrast to the situation at lower $\eta$, where the mode is overstable over a large part of the unstable window in $q_1$. For $\eta = 10^{-7}$ the mode is overstable in the range $2.76 < q_1 < 2.90$, and for $\eta = 5 \times 10^{-8}$ in the range $2.68 < q_1 < 2.84$. To completely stabilize the $m/n = 2/1$ tearing mode for this equilibrium, the resistivity must be reduced further. For example, at $q_1 = 2.65, \beta_p = 0.26$, the mode becomes stable at $\eta = 4 \times 10^{-8}$ (see Fig. 5.4).

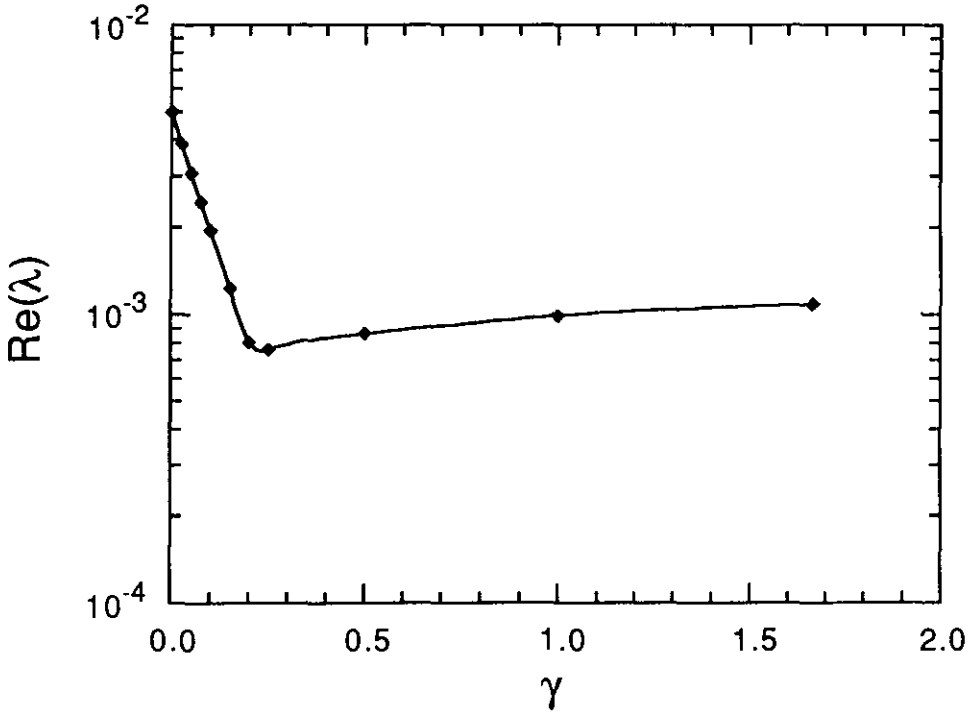


**Fig. 5.8** *The dependence of the growth rate of an $m/n = 2/1$ tearing mode on $\gamma$ (the ratio of the specific heats), showing the influence of the plasma compressibility.*

The influence of the compressibility of the plasma at a finite pressure can be studied by varying the value of $\gamma$, the ratio of the specific heats. The contribution of the plasma compression to the total energy in ideal MHD is given by (see Eq. (1.2)):

$$W_{comp.} = \gamma p |\nabla \cdot \boldsymbol{\xi}|^2 , \tag{5.7}$$

where $\boldsymbol{\xi}$ is the plasma displacement, $\partial \boldsymbol{\xi}/\partial t = \boldsymbol{v}$. The compression energy is positive definite and, therefore, stabilizing in ideal MHD. The contribution of this term can be determined by letting $\gamma$ go to zero such that the plasma compression does not require any energy. The dependence of the growth rate on $\gamma$ for $q_1 = 2.67, \eta = 10^{-6}$, and $\beta_p = 0.26$ is shown in Fig. 5.8. The growth rate at $\gamma = 0$ is approximately the same as the growth rate at zero $\beta$ so that we can conclude that the reduction in growth rate at finite $\beta$ and $\eta > 10^{-6}$ is due to the plasma compression of the tearing mode.

### 5.2.3 Numerical results, external modes.

Turning to the stability of the *external* or free boundary modes the picture changes considerably. The ideally conducting wall is removed from the plasma boundary and placed at a finite distance from the plasma, which is now surrounded by a vacuum. This removes the boundary condition on the normal component of the normal velocity and the plasma boundary is allowed to move freely. The condition on the normal component of the magnetic field perturbation at the ideally conducting wall is unchanged, although the condition is now on the vacuum magnetic field (see chapter 4).

Using the same equilibria as before (see Fig. 5.3), we have calculated the growth rate with the wall positioned relatively close to the plasma at 1.2 times minor radius. The shape of the wall is taken to be the same as the shape of the plasma boundary (circular in this case). The resulting growth rates of the resistive free boundary modes for $\beta_p = 0$ and $\beta_p = 0.26$ are shown in Fig. 5.9. For comparison we have included the growth rates of the fixed boundary modes at $\beta_p = 0.26$. The resistivity is $10^{-6}$.

The two maxima in Fig. 5.9, at $q_1 = 1.9$ and $q_1 = 2.9$, correspond to the $m = 2$ and $m = 3$ external modes. At the lower side of $q_1 = m/n$, the growth rates are largely determined by the underlying ideal instability as indicated in the figure for the $m = 3$ mode. At the $q_1 > m/n$ side the mode is purely resistive. As we increase $q_1$ to $q_1 > 2$, the $m = 2$ external mode at the steep part of the

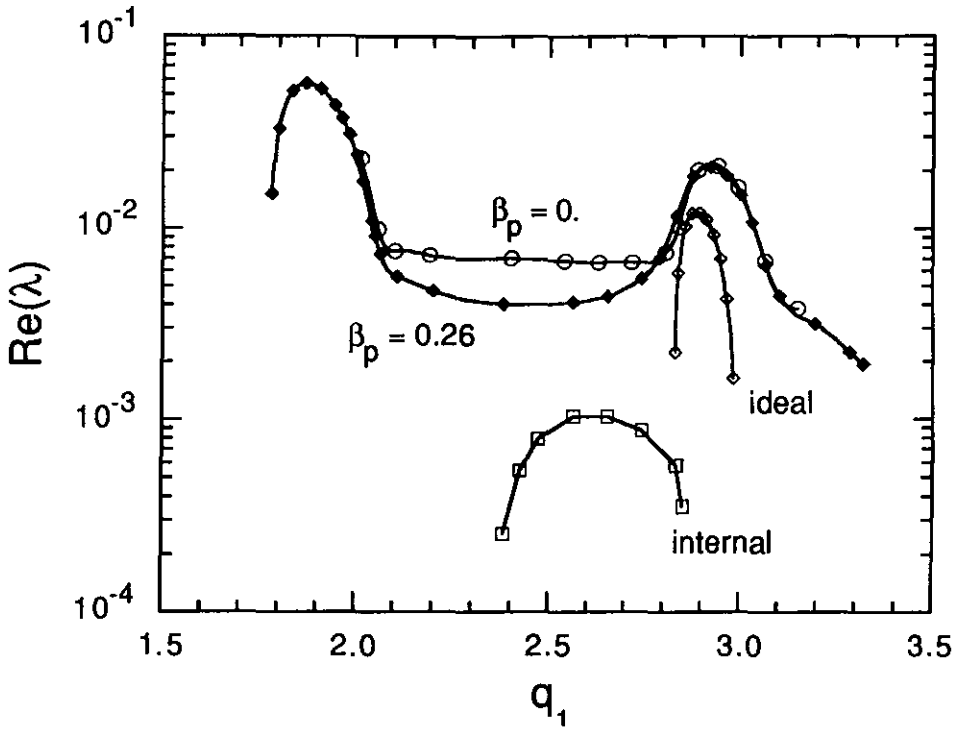


**Fig. 5.9** *The growth rate of the $n = 1$ free boundary tearing mode as a function of the value of $q$ at the boundary for two values of the total pressure. The resistivity is $10^{-6}$. The ideal $m = 3$ external kink mode and the $m = 2$ fixed boundary tearing mode are shown for comparison.*

curve changes to an 'internal' tearing mode. The 'internal' mode however still has a finite amplitude at the boundary. In the region near $q_1 = 2$ there is only one relevant rational $q$ surface and the behavior at zero pressure is similar to that in cylindrical geometry. Around $q_1 = 3$, however, the resistive $m/n = 3/1$ external mode is coupled to the $m/n = 2/1$ internal mode due to the toroidal geometry. The coupling increases the width of the region in which the resistive external mode is unstable. Without the coupling the marginal point of the resistive mode on the lower side of $q = 3$ would coincide with the marginal point of the ideal mode.

Comparing the growth rates at $\beta_p = 0$ and $\beta_p = 0.26$, we see that a finite pressure, at a resistivity of $10^{-6}$, has no effect at all on the stability of the external modes. For $q = m/n$ this is easily understood since there both the pressure and its gradient vanish at the rational surface. This is of course also true for $q_1 < m/n$ when the rational surface lies in the vacuum and the mode is basically ideal. This is not the case, however, at the $q > m/n$ side. On the steep part of the curve for $q > m/n$ it is not clear whether pressure stabilization is to be expected. In this part the mode is the resistive extension of the ideal external mode and the growth

rate of the mode is more determined by the current density gradient at the edge than by the gradient at the rational surface.

In the flat part of the curve at $\beta_p = 0$, the internal mode is dominant. When we compare this with the fixed boundary case shown in Fig. 5.5, it appears that at $\beta_p = 0$, the influence of the vacuum is very small. The only significant change is that the wall-stabilization of the $m = 2$ mode in the range $2 < q_1 < 2.2$ in the fixed boundary case does not survive with the wall placed at 1.2 times the minor radius. At $\beta_p = 0.26$, the vacuum has a larger influence. Compared to the fixed boundary case, the maximum growth rate is increased by a factor 4. In the free boundary case the plasma displacement of the 'internal' mode is less restricted so that the mode can largely avoid the plasma compression. This causes the increase in the growth rate compared to the fixed boundary case. The fact that also in the fixed boundary case a finite $\beta$ still reduces the growth rate shows that there is still a finite compression in the free boundary case. If we set $\gamma$ to zero so that plasma compression does not cost any energy, then the growth rates at $\beta_p = 0$ and $\beta_p = 0.26$ are again identical over the whole range of $q_1$.

In Fig. 5.10a and 5.10b we have plotted the radial profiles of the linear perturbation of the 'internal' mode at $q_1 = 2.38$ and $\beta_p = 0.26$, of the free boundary case and the fixed boundary case, respectively. The difference in compressibility is clearly shown by a comparison of the relative amplitudes of $v_1$ and the density perturbation $\rho$.

To show the pressure stabilization due to the average curvature in more detail, we have calculated the growth rate as a function of the resistivity for a number of values for $q_1$. The results are shown in Fig. 5.11, where we have plotted the real part of the eigenvalue. For $q_1 = 2.65$, the fixed boundary internal mode stabilizes at $\eta = 1.5 \times 10^{-8}$, whereas at $\eta = 5 \times 10^{-7}$ the mode becomes overstable. The corresponding free boundary mode, however, follows the tearing mode scaling $\lambda \sim \eta^{3/5}$ up to $\eta \sim 10^{-8}$. The mode does stabilize eventually at $\eta < 2 \times 10^{-9}$. Also shown in Fig. 5.11, is the $\eta$ dependence of the resistive external mode at $q_1 = 3.00$. As expected, it shows no sign of stabilization.

The equilibria we have examined so far in this paragraph were chosen such that there is only one rational surface inside the plasma. This leads to equilibria which are characterized by a very broad current density profile with large current gradients at the edge. Both the ideal and the resistive free boundary mode are therefore very unstable. In the following part, we will examine the influence of the vacuum for a different class of equilibria with a relatively peaked current density

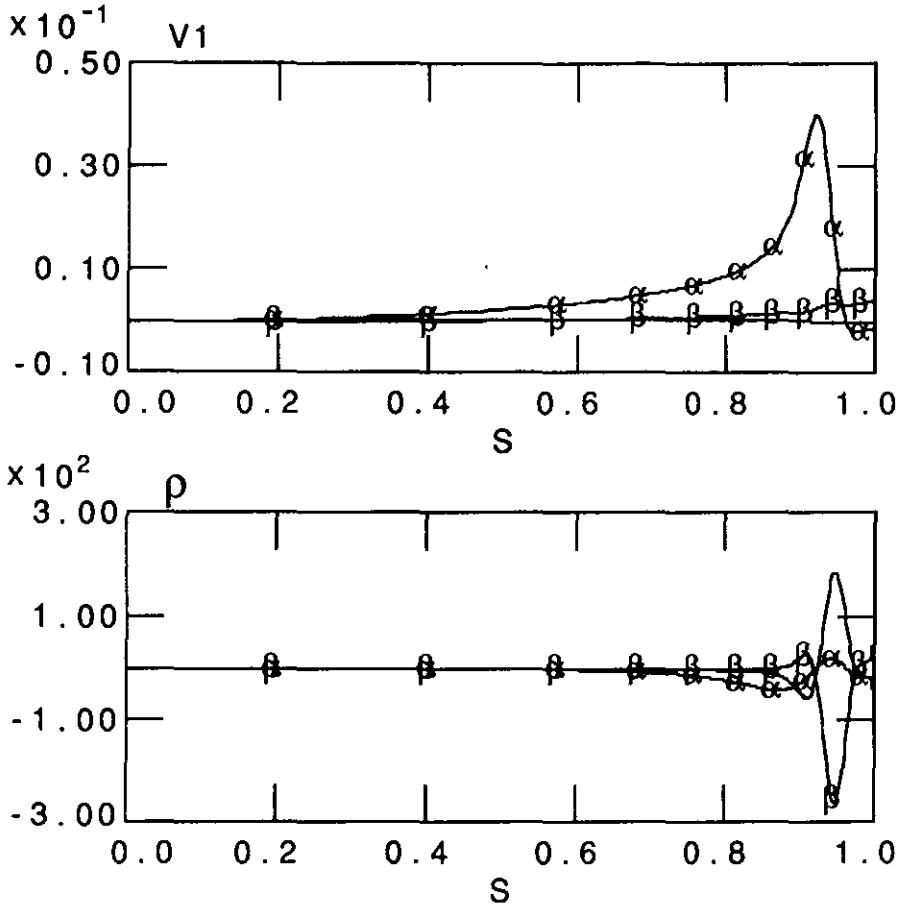


**Fig. 5.10a** *The $m = 1, 2,$ and 3 harmonics of the normal component of the velocity perturbation, $v_1$, and of the density perturbation, $\rho$, of the free boundary $n = 1$ tearing mode at $\beta_p = 0.26$. The $m = 2$ and 3 harmonics are indicated by $\alpha$ and $\beta$.*

profile. The internal modes will then be more unstable in the central part of the plasma and because of the smaller current gradient at the edge, the external modes will be more stable. Because of the peaked current, the value of $q_1/q_0$ will be larger. For the equilibria considered $q_1/q_0 = 3.4$, which means that there are three or four rational surfaces ($q = 2, 3, 4,$ and 5) inside the plasma, depending on the actual value of $q_1$.

The equilibrium profiles of the peaked current case are given by $\Gamma(\psi) = 1 - 1.5\psi + 0.5\psi^2$ and $\Pi(\psi) = 1 - \psi$. The aspect ratio is the same as before, viz. $\epsilon = 0.25$. The profiles of the pressure, the current density, and $q$ as a function of the normalized minor radius are plotted in Fig. 5.12.

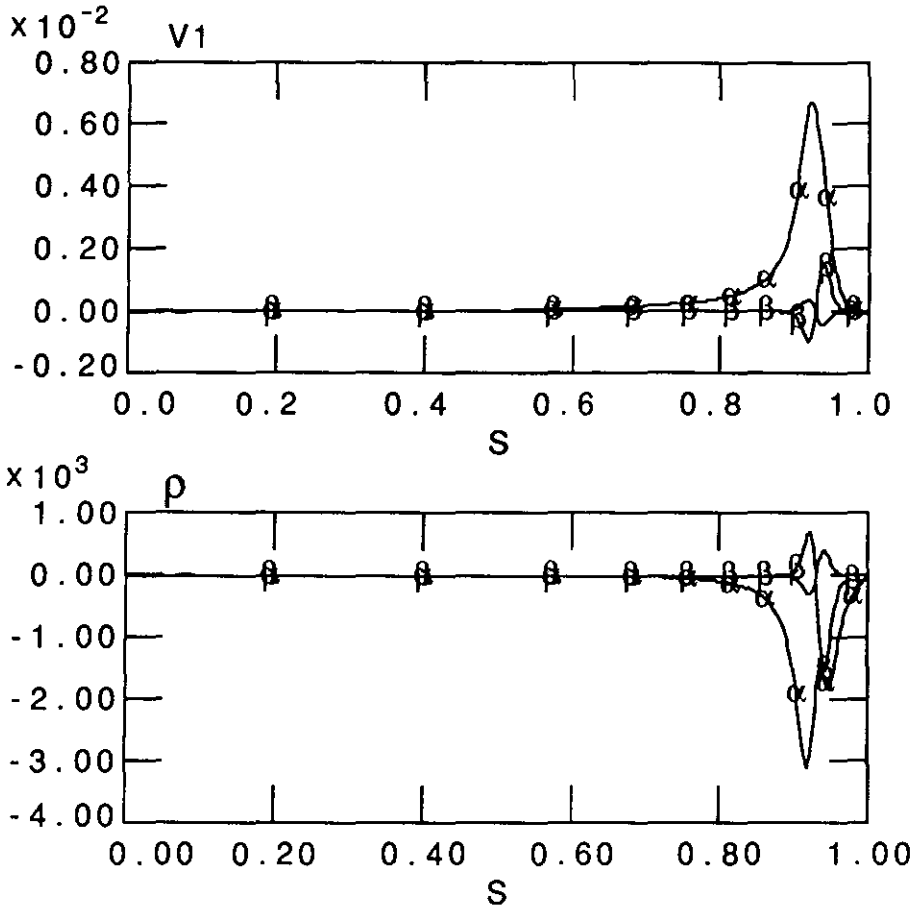


**Fig. 5.10b** *The $m = 1, 2,$ and 3 harmonics of the velocity perturbation and of the density perturbation of the fixed boundary $n = 1$ tearing mode at $\beta_p = 0.26$. The $m = 2$ and 3 harmonics are indicated by $\alpha$ and $\beta$.*

Because of the smaller edge current density gradients, the ideal $m = 3$ and $m = 4$ external modes are stable in these equilibria. We will not consider the $m = 2$ external mode since this would correspond to an equilibrium with $q$ on axis of about 0.67. This means that the resistive $m/n = 1/1$ internal kink mode would be unstable. Although the coupling of the internal kink to the external modes is itself an interesting subject, it will not be discussed in this paragraph. The growth rates of the resistive modes are plotted in Fig. 5.13 for $\eta = 10^{-6}$, and $\beta_p = 0$ and 0.26, both with the wall on the plasma and with the wall positioned at 10 times the minor radius.

The growth rates of the fixed boundary case are again due to the $m/n = 2/1$ tearing mode. Inspection of the eigenfunctions (not shown here) shows that, with the wall on the plasma, there is almost no coupling to the higher $m$ mode numbers.

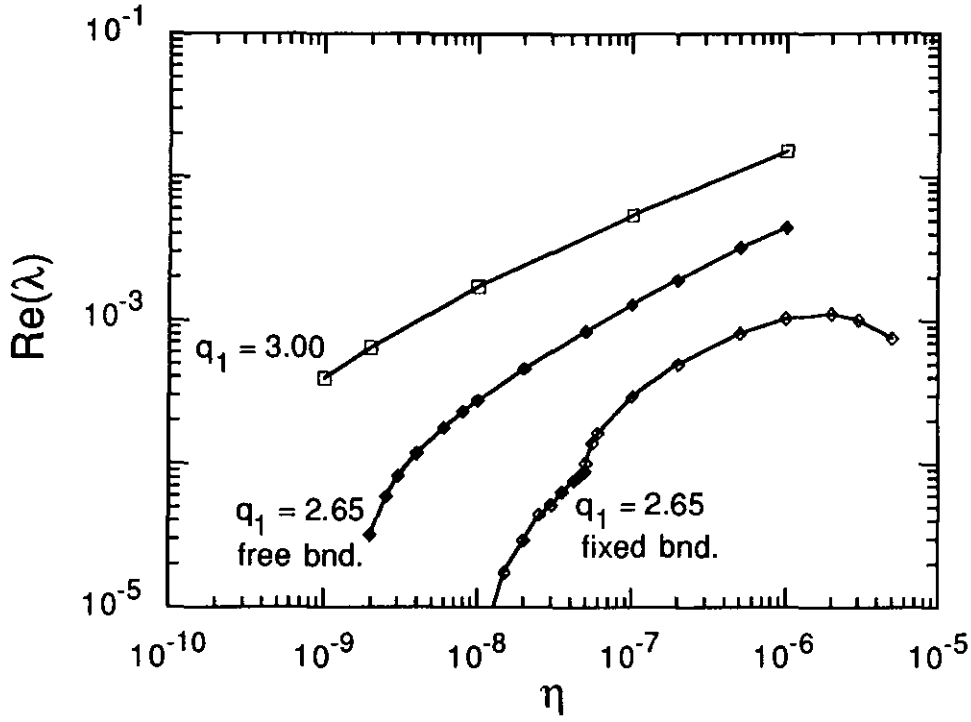


**Fig. 5.11** *The growth rate of the $n = 1$ free boundary tearing mode as a function of the resistivity for two values of $q$ at the boundary. The fixed boundary $m/n = 2/1$ tearing mode is included for comparison.*

Removing the wall has much less influence for these equilibria compared to the broad current density profile case, since the $m/n = 2/1$ is only unstable when $q = 2$ lies in the central part of the plasma. Only when $q_1$ is close to 3, where the $m = 3$ free boundary mode becomes unstable and couples to the $m = 2$ internal mode, there is a large increase in the growth rate. An interesting point is that there is no sign of an unstable ideal mode at $q_1 < 3$. The $m = 3$ is a purely resistive instability which is also present when the rational surface lies in the vacuum. This shows that the external resistive modes can also exist without an underlying ideal instability.

The effect of a small pressure is the same as in the case of a broad current density profile, the stabilization at $\eta = 10^{-6}$ is largely due to the plasma compression. For $q_1 > 4.5$ the effect of a vacuum is very small, the additional freedom does not affect the $m = 2$ mode in the central part of the plasma. Different from the previous case is that at $q_1 = 3$ the growth rate of the mode is now reduced by the pressure. This is caused by the coupling to the $m = 2$ which is affected by the pressure when $q = 2$ lies closer to the boundary.

Reducing the resistivity from $10^{-6}$ to $10^{-7}$ has a large stabilizing effect on

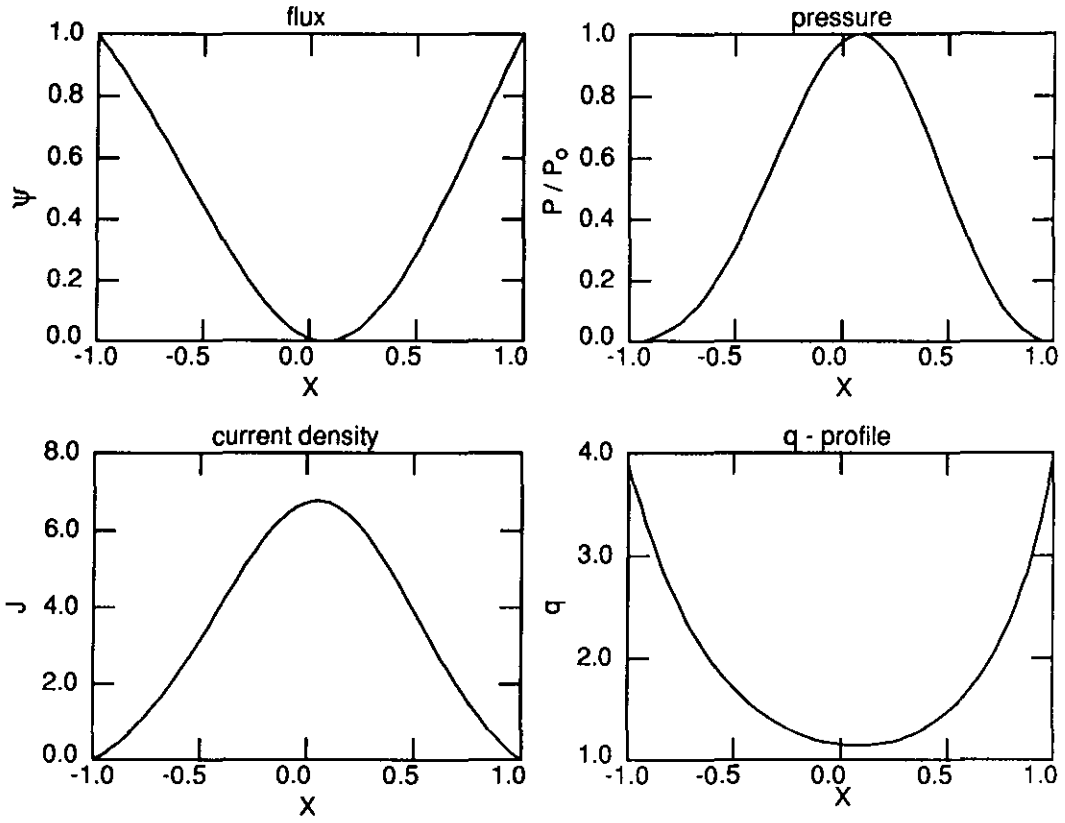


**Fig. 5.12** *The equilibrium profiles of the flux, the pressure, the current density and the q-profile, for the peaked current case as a function of the normalized minor radius (x).*

the fixed boundary case (see Fig. 5.14). In the free boundary case the modes are again less easily stabilized. Notice that around $q = 3$ and 4, where the mode amplitude peaks at the plasma boundary, the reduction of the growth rate is much smaller since there the pressure gradient vanishes at the rational surface.

Summarizing this section, the stabilizing effect of a finite pressure on the stability of the $n = 1$ fixed boundary tearing mode is twofold. First of all, the fixed boundary tearing mode causes a local compression of the plasma which requires an energy proportional to the local pressure. The good average curvature in the toroidal geometry in the presence of a finite pressure gradient provides another source of stabilization. Removing the ideally conducting wall from the plasma to a finite distance away from the plasma, gives the plasma an additional degree of freedom. This allows tearing modes which are localized near the plasma boundary to become essentially incompressible, such that the stabilizing effect of the pressure is much smaller in the free boundary situation. The tearing modes localized in

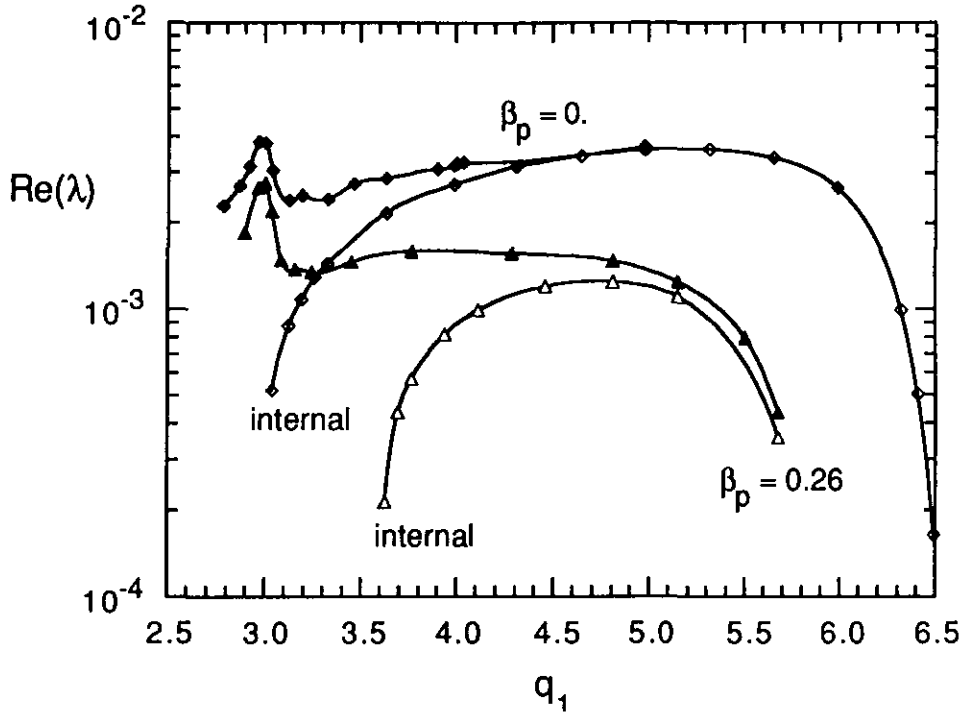


**Fig. 5.13** *The growth rate of the $n = 1$ fixed and free boundary tearing mode as a function of $q$ at the edge for the peaked current density case for $\beta_p = 0$ and $\beta_p = 0.26$. The resistivity is $10^{-6}$. The fixed boundary mode is an $m/n = 2/1$ tearing mode.*

the plasma center are not influenced by the different boundary conditions. Since pressure gradient goes to zero at the plasma boundary, the stabilization due to the average curvature is also much less efficient for modes near the boundary. Thus, the stabilizing influence on the tearing mode, which can be very effective for modes in the plasma center, is not effective for tearing modes localized near the plasma boundary.

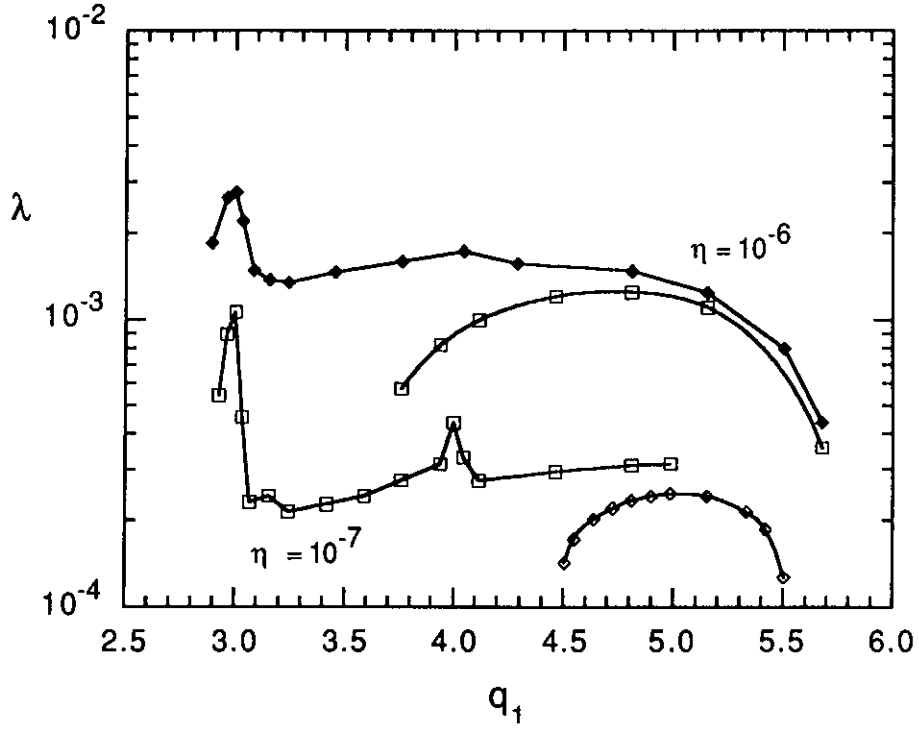


**Fig. 5.14** *The growth rate of the $n = 1$ fixed and free boundary tearing mode versus the value of $q$ at the boundary for different values of the resistivity for the peaked current density case. The ideal external kink mode is stable.*

## 5.3 Toroidal geometry; Shaping effects

Many of the present-day tokamaks can be operated in an X-point configuration to allow plasmas in the so-called H-mode regime. In this configuration the plasma boundary is not defined by a contact with the limiter but by the separatrix. In the X-point, the poloidal magnetic field is zero so that the safety factor $q$ will go to infinity towards the plasma boundary. The increased shear close to the plasma boundary, caused by the X-point shape, will have a large effect on MHD modes which are localized near the boundary. Ballooning modes, for example, can be stabilized near the plasma edge to the extent that they do not pose a limit on the local pressure gradient (see section 6.1).

The influence of the X-point geometry on the *ideal* $n = 1$ external kink mode has been investigated by [Ozeki88] and more extensively by [Roy90]. It was shown that, in general, the large shear near the boundary has a stabilizing effect on the $n = 1$ external kink mode. In a study of current and $\beta$ limits, it was found [Roy90] that the presence of a single X-point in a quasi-circular equilibrium can increase the maximum plasma current at which the $n = 1$ mode is still stable considerably as compared to a circular plasma. The increase of the current limit depends on

the poloidal position of the X-point. In the most favorable configuration the X-point is pointing upwards (or downwards). The maximum $\beta$, stable to the $n = 1$ mode, is larger only in the case where the X-point is pointing upwards. At other orientations of the X-point, the maximum $\beta$ is similar or even lower than in the circular case. The mode structure of the ideal $n = 1$ mode in the presence of an X-point becomes more localized near the plasma boundary with the plasma flow more parallel to the magnetic surfaces.

In this section we investigate the influence of an X-point plasma shape on the stability of the $n = 1$ free boundary resistive tearing modes localized near the plasma boundary. To enable a comparison with the stability of the free boundary tearing in a circular plasma, we use a quasi-circular plasma with a small perturbation of the plasma boundary. To avoid the singularity at the X-points, the shape of the plasma boundary is approximated by a closed flux surface just inside the separatrix. An example of the equilibrium flux surfaces of the X-point plasma are shown in Fig. 5.15a. The straight field line coordinate system used in the CASTOR code is not very well suited for the treatment of an X-point. The coordinate lines of the poloidal angle tend to bend towards the X-point in a region close to the plasma boundary. To obtain an accurate representation of the equilibrium quantities near the boundary, a non-equidistant radial grid is used with the grid points packed close to the plasma boundary. The equilibrium profiles of the flux surface averaged current density, the $q$-profile, and the shear ($= s/q\,\partial q/\partial s$) profile as a function of $s$ ($= \sqrt{\psi}$) are shown in Fig. 5.15b. For comparison, we have included the $q$ and shear profiles for a circular plasma boundary keeping the current density profile fixed. The influence of the X-point is confined to a region close to the boundary, $0.9 < s < 1$. The aspect ratio is 4, the poloidal $\beta$ is 0.35. The current density gradient has a shoulder near the edge of the plasma to create a situation which is violently unstable in a circular plasma.

First, we compare the growth rates of the ideal external kink mode as a function of the value of $q$ at the boundary for the X-point shape of Fig. 5.15a and for a circular plasma. The equilibrium profiles are kept the same. The wall is placed at 10 times the minor radius. The resulting growth rates are shown in Fig. 5.16. The maximum growth rate in the X-point geometry decreases by a factor 2.6 and the unstable window in $q_1$ becomes smaller at the low $q_1$ side. This is in good agreement with [Ozeki88]. The poloidal components of the velocity perturbation in the poloidal plane are plotted in Figs. 5.17a and b. The mode is mainly an $m = 3$ mode which becomes much more localized at the plasma boundary by the increased shear of the X-point geometry.

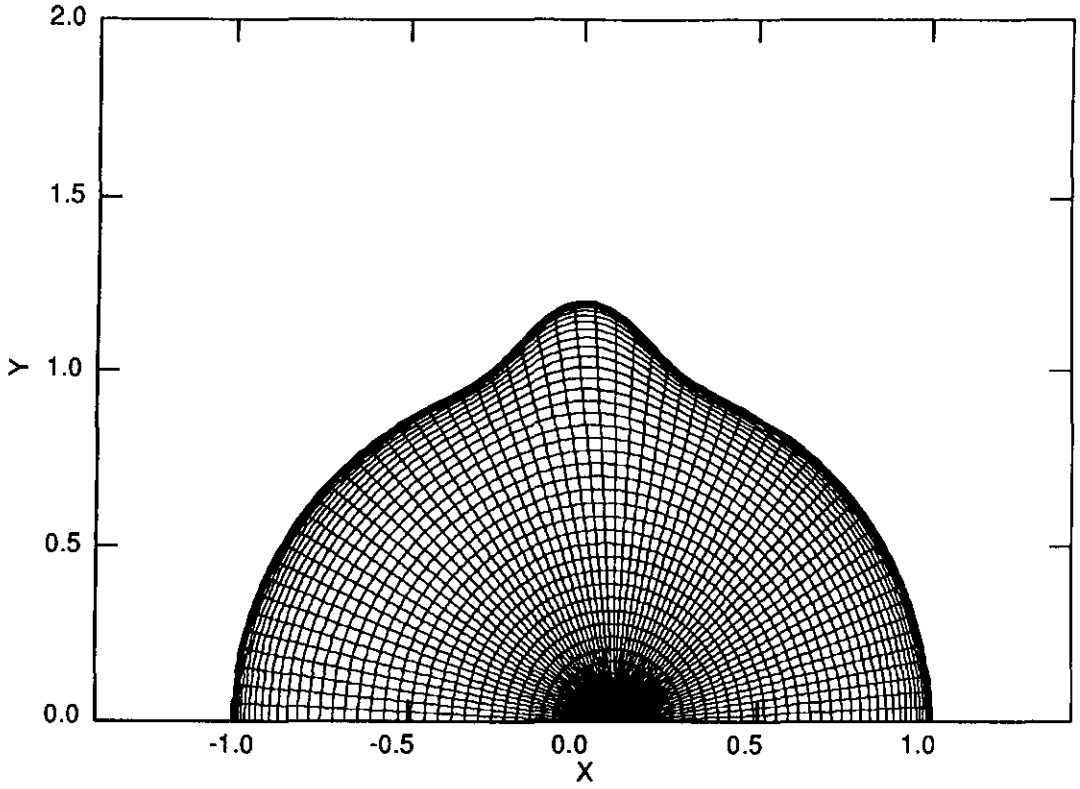


**Fig. 5.15a** *The flux surfaces of the X-point equilibrium.*

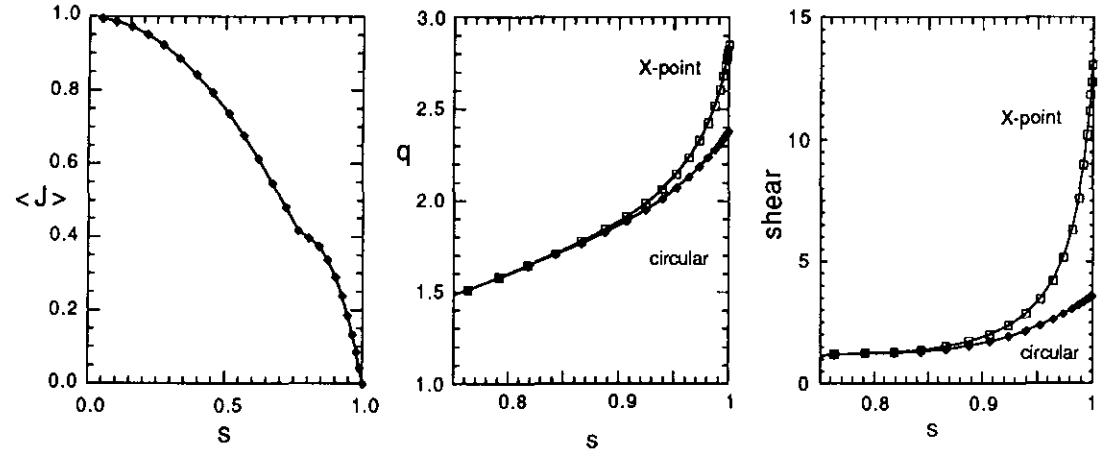


**Fig. 5.15b** *The profiles of the flux surface averaged current density, the safety factor $q$, and the shear as a function of the flux coordinate $s = \sqrt{\psi}$ for both the circular and the X-point equilibrium.*

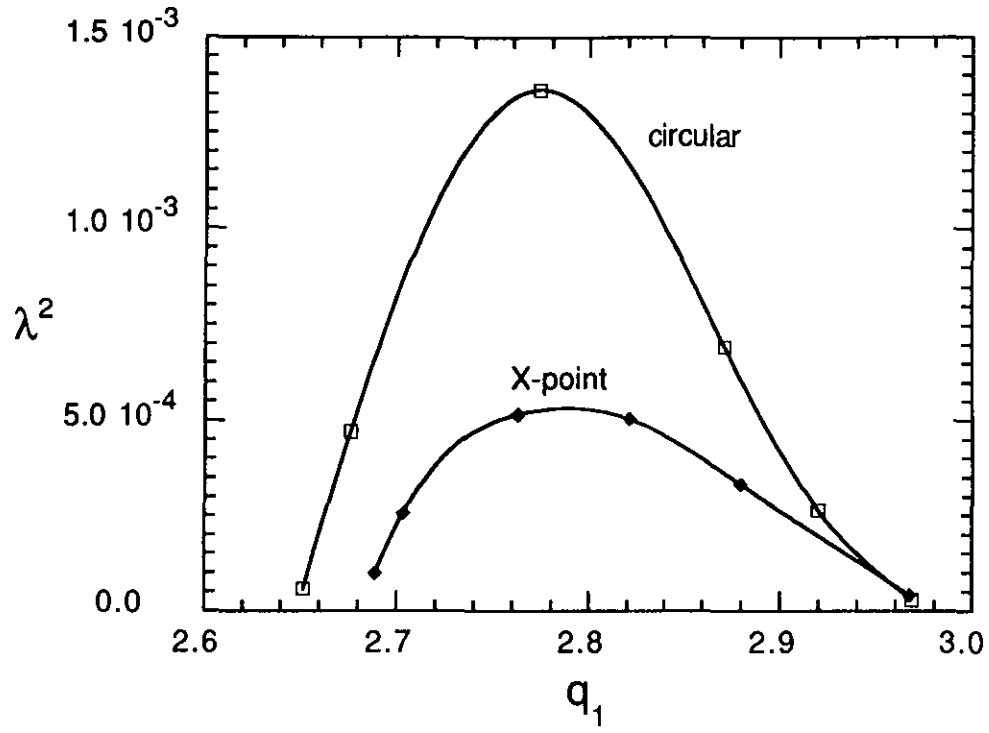


**Fig. 5.16** *The growth rate of the ideal $n = 1$ external kink mode as a function of $q$ at the boundary for the circular and the X-point plasma shape.*

The growth rate of the resistive free boundary $n = 1$ tearing mode as a function of the value of $q$ at the edge is plotted in Fig. 5.18, again for a circular and for an X-point shape. As in the previous calculations, the resistivity is taken constant over the plasma radius with a value of $\eta = 10^{-6}$. The maxima correspond to the $m = 3$ and $m = 4$ external modes. For $3.1 < q_1 < 3.8$ the instability is mainly an internal $m = 2$ tearing mode. For $q_1$ smaller than 3, the reduction of the growth rate of the resistive mode in the X-point geometry is similar to that of the underlying ideal mode. For $q_1$ larger than 3 the influence of the X-point appears to be much smaller. However, the stability windows of the external modes are not very clear in this picture due to the coupling to the internal $m = 2$ mode.

The internal and external modes can be separated if we lower the resistivity in the central part of the plasma. The $m = 2$ internal mode is then stabilized by the finite pressure (see section 5.2). Near the boundary ($0.95 < s < 1.$), the resistivity is constant with $\eta = 10^{-6}$. In the central part the resistivity is set to $10^{-12}$. This choice of resistivity profile effectively decouples the external modes localized near the boundary from the internal tearing modes through the pressure/curvature stabilization at low resistivity (as discussed in the previous section).

In Fig. 5.19 the growth rate of the $m = 3$ external mode is plotted versus

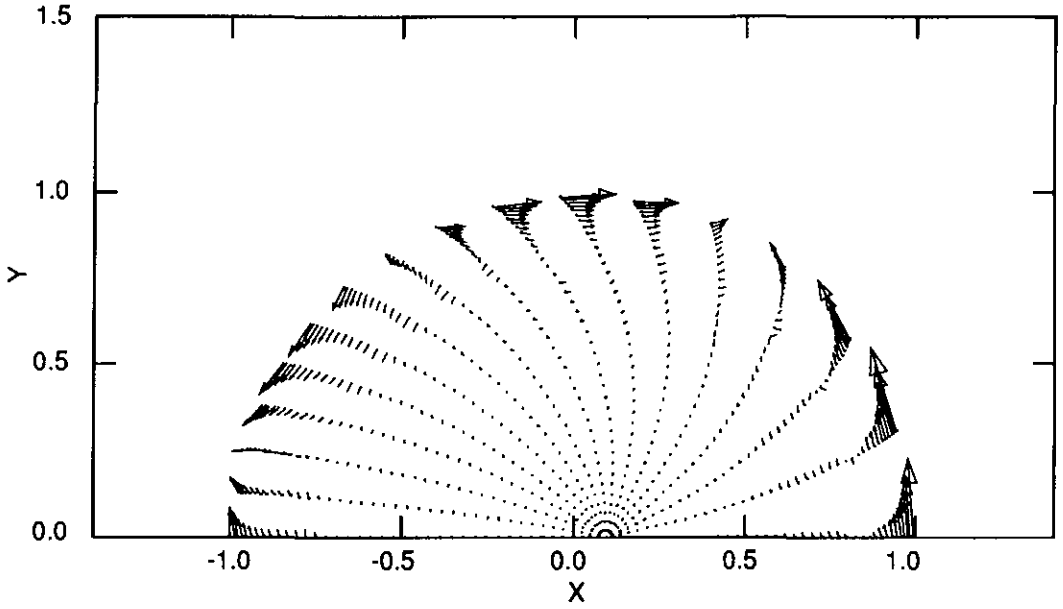


**Fig. 5.17a** *Vector plot of the poloidal velocity perturbation of the ideal $n = 1$ external kink mode in the circular plasma.*

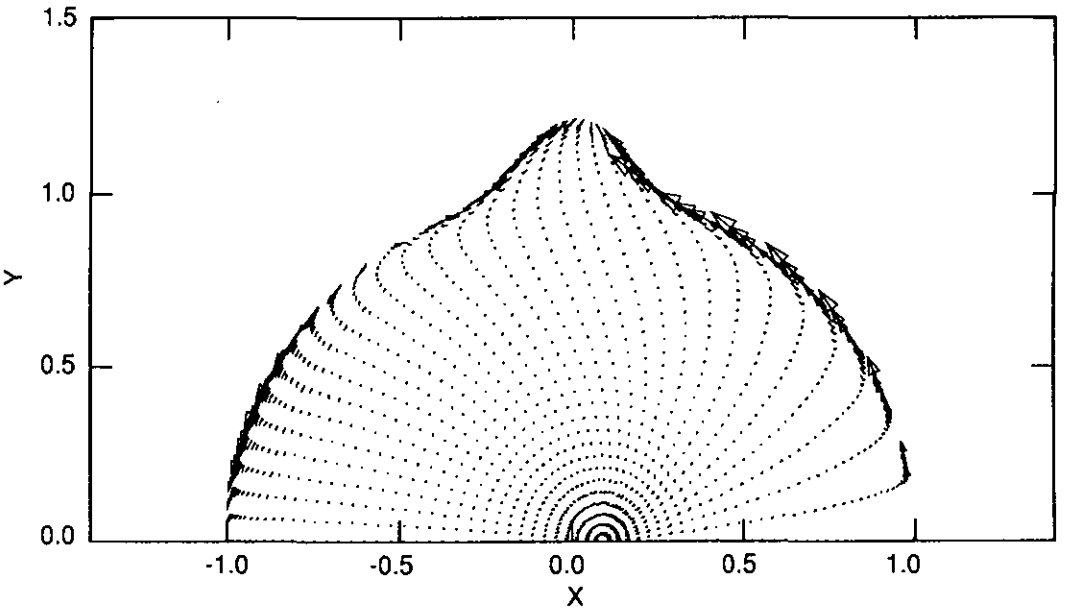


**Fig. 5.17b** *Vector plot of the poloidal velocity perturbation of the ideal $n = 1$ external kink mode in the X-point plasma.*

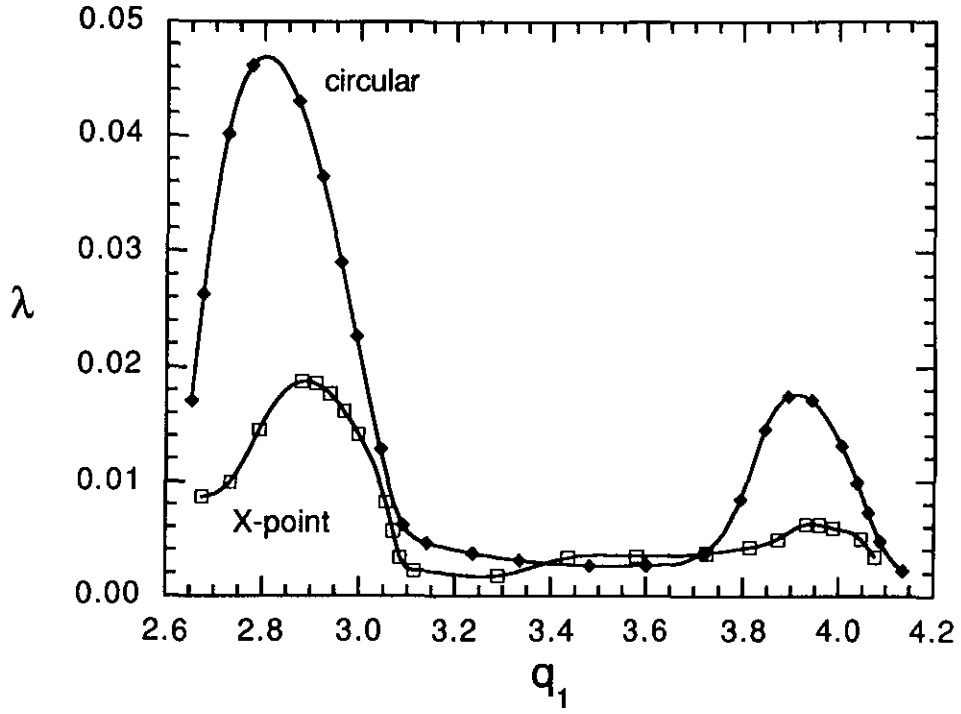


**Fig. 5.18** *The growth rate of the $n = 1$ free boundary tearing mode versus the value of $q$ at the boundary for the circular and the X-point plasma shape. The resistivity is $10^{-6}$.*

the value of $q$ at the boundary for the circular and the X-point plasma shape. Shown are the growth rates of both the ideal plasma and of the plasma with the resistivity profile as described above. The curves for the ideal plasma are the same as in Fig. 5.16, where $\lambda^2$ was plotted instead of $\lambda$. For the circular plasma, the stability threshold at $q_1 < 3$ is not changed by a finite resistivity. Surprisingly, however, for the X-point case the plasma is more stable with a finite resistivity as compared to the ideal plasma. This stabilizing effect can be attributed to the resistive boundary conditions which are more restrictive than the ideal boundary conditions in the sense that a surface current is not allowed. The surface current is replaced by a large current density in the resistive boundary layer. In the circular case, the radial width of the mode is much larger than the resistive boundary layer so that the influence of the resistive boundary conditions is very small. In the case of the X-point shape, the radial width of the mode is much smaller (see Fig. 5.17) so that the restrictive influence of the resistive boundary conditions is larger.

For $q_1 > 3$, where the ideal external mode is stable, the increased shear at the plasma boundary of the X-point plasma has no large effect. There is a small reduction of the growth rate but the stability window in $q_1$ is not affected. This

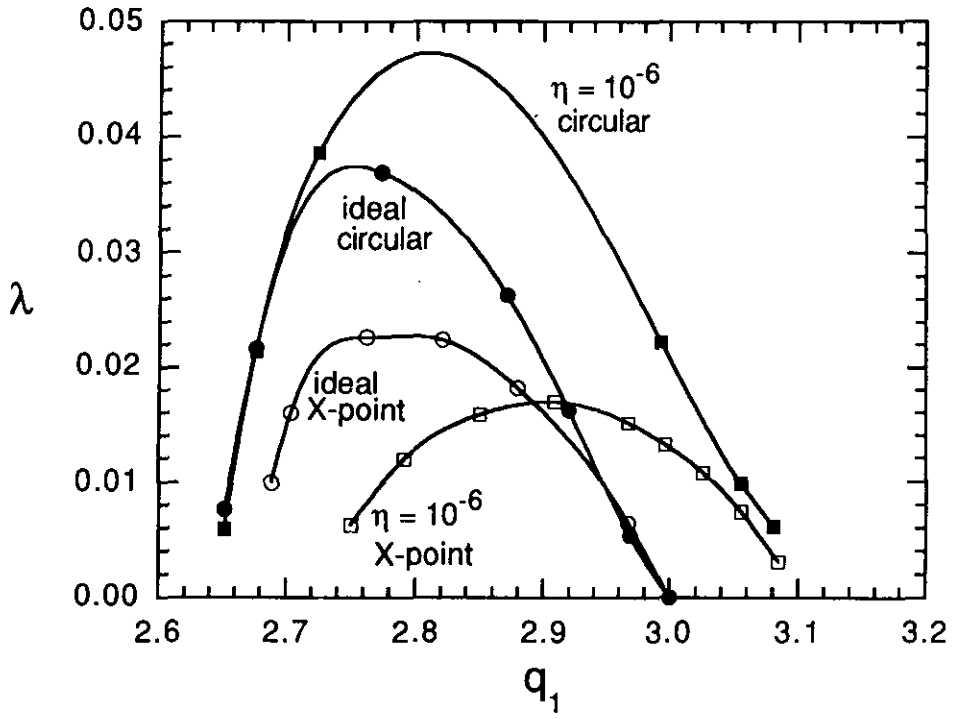


**Fig. 5.19** *A comparison of the growth rates of the ideal and the resistive $n = 1$ free boundary mode in both the circular and the X-point plasma.*

is also illustrated by Fig. 5.20 where we compare the growth rate of the $m = 3$ mode for the circular and the X-point shape as a function of the gradient of the flux surface averaged toroidal current density at a fixed value of $q$ at the boundary, $q_1 = 3.0$. The gradient of the current density is changed locally between $0.8 < s < 1$ by adding a parabolic current profile centered at $s = 0.9$. Extrapolating to zero growth rate shows that the marginally stable gradient of the current density is the same for both plasma shapes.

In conclusion, the stabilizing effect of the high shear near the boundary of an X-point plasma is larger for the resistive version of the external mode than for the ideal mode, if the rational surface lies in the vacuum. This is due to the very small radial extent of the mode in the high shear region in combination with the resistive boundary conditions, which do not allow a surface current density at the plasma boundary (contrary to the ideal boundary conditions). The high shear has much less influence on the stability of the tearing mode if the rational surface lies inside the plasma.

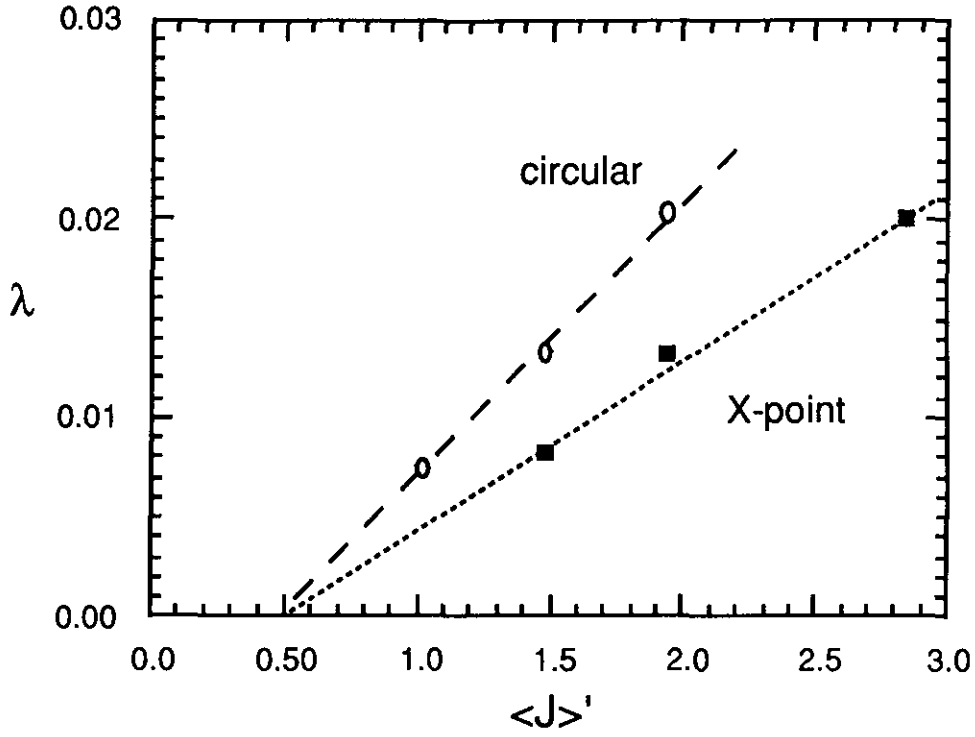


**Fig. 5.20** *The growth rate of the $n = 1$ free boundary tearing mode as a function of the current density gradient at the plasma boundary for the circular and for the X-point plasma shape.*

## 5.4 Conclusion

In this chapter, some aspects have been studied of the stability of free boundary tearing modes in a general toroidal geometry using the numerical codes CASTOR and HELENA, as described in the chapters 2, 3, and 4. The additional freedom of the moving boundary of a resistive plasma allows the resistive version of the ideal external kink to become unstable. This enlarges the instability window of the external kink mode in that the resistive mode, unlike the ideal mode, can also be unstable if the rational $q$-surface lies inside the plasma. This mode is essentially a tearing mode with a large amplitude at the plasma boundary. The effect of the free boundary is not limited to these external modes, it also has a significant influence on the stability of 'internal' modes, i.e., modes which can be unstable with a fixed plasma boundary.

In the first part of the chapter, we have examined the influence of a finite pressure on the stability of both the fixed and free boundary tearing modes. The effect of the pressure appears to be twofold. The fixed boundary tearing mode causes a compression of the plasma. At a finite pressure, the compression costs an amount of energy proportional to the pressure. This has a large stabilizing effect.

Removing the ideally conducting wall from the plasma boundary greatly reduces the compression of the plasma against the wall for modes localized near the boundary. Consequently, the stabilizing effect of the pressure due to the compression is lost.

The second effect of the pressure is due to the stabilizing influence of the 'good' average curvature of the magnetic field lines in a torus in combination with a finite pressure gradient at the rational $q$-surface. This effect becomes larger with decreasing resistivity. The curvature stabilization is very effective for the internal tearing modes. The external resistive modes with the rational surface close to the plasma boundary or in the vacuum are not influenced by the curvature since the pressure gradient goes to zero at the plasma edge.

In the second part of this chapter, we have investigated the effect of an X-point plasma shape on the stability of the external resistive mode. The increased shear near the plasma boundary in the region where the external mode is localized has a large stabilizing influence on the ideal external kink mode. It was shown that, surprisingly, a finite resistivity has an additional stabilizing effect on the external mode if the rational $q$-surface lies in the vacuum. This is attributed to the fact that the resistive MHD boundary conditions are more restrictive than the ideal ones since they do not allow surface currents at the plasma boundary. The effect of the X-point plasma shape is less stabilizing if the rational surface lies inside the plasma.

# 6. APPLICATION TO JET PLASMAS, THE ELM PRECURSOR

The Joint European Torus (JET) is the largest operating tokamak facility to date. The center of the vacuum vessel has a major radius of 2.96 m. The plasmas typically have a minor radius (in the horizontal plane) of 1.1 m. The maximum vacuum magnetic field in the center is 3.45 T. In JET, operation is possible in both limiter and X-point configuration. In the limiter configuration, the plasma boundary is typically given by an ellipticity of 1.5-1.8 and a triangularity of 0.2-0.3 (D-shaped). In the X-point configuration, with one single X-point or a double X-point at the top and bottom of the plasma, the plasma boundary is defined by the separatrix, i.e., the fluxsurface where the poloidal field goes to zero. In this configuration the ellipticity and triangularity are typically 1.7-1.8 and 0.3-0.40. An example of a JET equilibrium is shown in Fig. 6.1, where the equilibrium flux surfaces are plotted together with the vacuum vessel and the limiters. The maximum plasma currents in JET range from 7 MA in the limiter configuration to 3.5 and 5 MA, in respectively, the double and single X-point configuration. For the additional heating of the plasmas, both neutral beam and ion cyclotron heating are used, with a maximum power of 21 and 22 MW, respectively.

## 6.1 The ELM precursor

In a tokamak plasma where the plasma boundary is determined by a separatrix, the plasma can go from the so-called L(ow)-mode phase into a different regime called the H(igh)-mode phase. The additional heating power must exceed a certain threshold for the transition to occur. In the L-mode phase, the energy confinement time is deteriorated by the additional heating as compared to the confinement time in an ohmically heated plasma. The H-mode phase was discovered in 1982 in the ASDEX tokamak [Wagner82]. This phase is characterized by an increase in the energy confinement time by typically a factor 2 as compared to the L-mode phase. The particle confinement time is also improved during the H-mode phase. Experimentally, the L to H transition is marked by a drop in the $D_\alpha$ light which is a measure of the particle flux to the wall. At the transition, the total stored energy and the density start to increase. The improvements are (mainly) due to a local decrease in the energy and particle diffusivity near the plasma edge. As a consequence, both the temperature and the density profile develop large gradients near the plasma edge. The higher temperatures near the

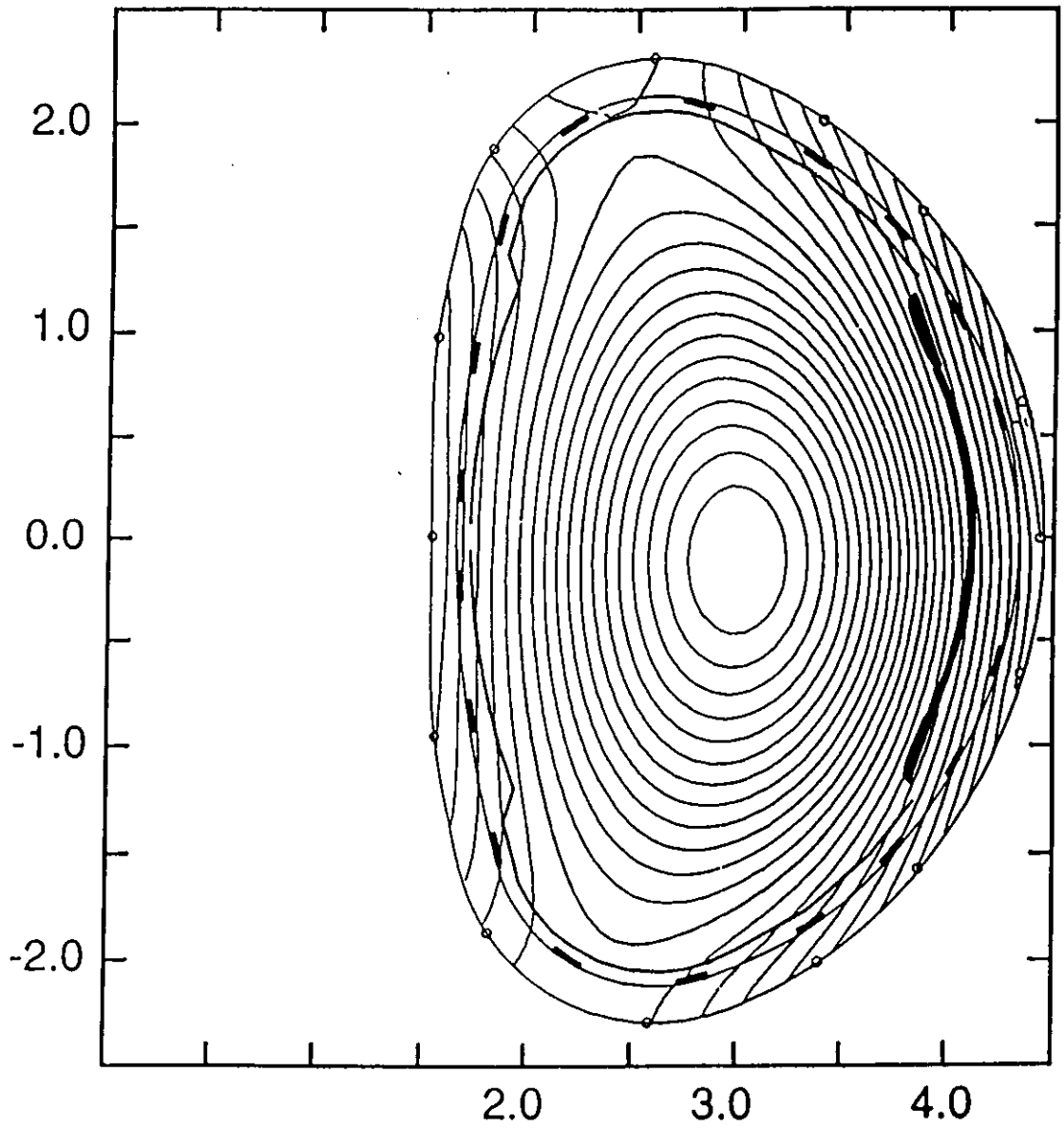


**Fig. 6.1** *The JET plasma shape in a double X-point configuration (discharge # 23336, time = 55.0s). The small circles represent the flux loops, the black rectangles show the positions of the pickup coils.*

edge lead to a broadening of the current density profile. A disadvantage of the H-mode is that, with the improved particle confinement, the impurities are also better confined. The impurity accumulation in the plasma eventually leads to the end of the H-mode when the energy losses due to the radiation become comparable to the input power [Gianella89].

Due to the steepening of the equilibrium profiles near the plasma boundary

during the H-mode, notably the pressure profile and the current density profile, an MHD instability can develop near the edge of the plasma. Experimentally, this so-called Edge Localized Mode (ELM) is observed as a spike in the $D_\alpha$ signal, accompanied by an increase in the magnetic signals. This signifies a rapid loss of energy and particles from the plasma edge into the scrape-off layer. Depending on the amplitude of the instability, an ELM expels typically 5-20% of the plasma energy content. This results in a degradation of the confinement time. The ELMs can however also be beneficial for the plasma performance. By adjusting the rate in which the ELMs occur, it is possible to control the increase in density and impurity content in the plasma. In this way, semi-stationary H-mode discharges have been produced [Burrel89, ASDEX90].

The underlying MHD phenomena of the ELM are not very well understood. The manifestation of the ELM depends on the equilibrium parameters and is different in different machines. In the DIII-D tokamak, three different types of ELMs have been identified experimentally [Doyle91].

1. The so-called giant ELMs occur in the high-$\beta$ plasmas near the Troyon limit. These ELMs are characterized by a large, more or less isolated, spike in the $D_\alpha$ signal. The repetition rate of this type of ELM increases with the heating power and decreases with increasing toroidal current. Gohil et al. [Gohil88] showed that the pressure gradients near the plasma edge just before the occurrence of the giant ELM are close to the ideal ballooning limit. They suggested that the ELM may be a transient return to the L-mode triggered by the pressure gradient hitting the first ideal high-$n$ ballooning stability boundary.

2. The second type of ELM is characterized by smaller, irregular, and more frequent spikes in the $D_\alpha$ signal. In DIII-D, these 'grassy' ELMs have been related to the second region of stability of the ideal ballooning modes. Extending the theoretical study of [Bishop86] to the relevant DIII-D plasma parameters, Ozeki et al. showed [Ozeki90] that near the separatrix, for large enough values of the ellipticity ($> 1.8$) and of the triangularity ($> 0.4$), the first stability boundary of the ideal ballooning modes disappears for low values of the shear. In this region of the plasma the pressure gradient is not limited by ballooning modes. Experimentally it was found that in the parameter range of the second stability region, the giant ELMs no longer occur. Instead, grassy ELMs are observed. The maximum amplitude of the pressure gradient is, however, still similar to that in the giant ELM discharges. Resistive ballooning modes were suggested as the modes limiting the pressure gradient.

3. Contrary to the first two types, the type-III ELM occurs at low $\beta$. Also different is that, with increasing heating power, the repetition rate of the ELMs decreases. This type of ELM shows a clear precursor on a resistive time scale with a large toroidal mode number ($n = 6 - 12$) having the largest mode amplitude on the outside. No explanation in terms of an MHD mode has been put forward for this type of ELM.

In the PBX-M tokamak [Kaye90], as in DIII-D, giant ELMs only occur in high-$\beta$ plasmas. The giant ELMs are preceded by a high frequency precursor which is growing on a time scale of the order of 10 $\mu s$. Different from DIII-D, the pressure gradient near the edge was found to be below the ideal ballooning mode limit. Also, the measured magnetic signal does not have a ballooning character. A theoretical stability analysis of low-$n$ ideal modes showed that, depending on the position of the wall, a pressure driven kink mode can be unstable. The structure of the mode is very global with a large $m = 1$ contribution in the plasma center and higher $m$ numbers near the boundary.

In the ASDEX tokamak [Zohm91, ASDEX89], the ELMs are observed when the pressure gradient is near the ballooning stability limit, but also when the pressure gradient is still low. The ELMs in ASDEX are preceded by a coherent high frequency precursor with large poloidal mode numbers $m \sim 10 - 15$. The growth time of the precursor just before the ELM is of the order of $50\mu s$. The ELM itself is seen, apart from the spike on the $D_\alpha$ signal, as broadband turbulence on the magnetic signals. The radial position of the ELM appears to be independent of the total current (i.e. $q_a$). As in DIII-D, the repetition rate of the ELMs decreases with increasing heating power. Stability analysis showed both the ideal ballooning and the ideal kink modes to be stable.

A free boundary, resistive MHD simulation of the non-linear evolution of the ELM in a circular cylinder was done by [Kerner and Jacoby88]. It was shown that for typical ASDEX H-mode equilibrium profiles, the different poloidal harmonics of the pressure and current density gradient driven instabilities couple non-linearly. This causes an expansion of the plasma and a turbulent layer of about 10% of the minor radius which develops on a time scale of $\sim$ 150 Alfvén times. For typical L-mode profiles the amplitude of the linear modes is too small to develop turbulence and the plasma boundary is not perturbed. From this simulation it has been concluded [Zohm91] that the ELM precursor in ASDEX is a resistive pressure driven mode with a medium poloidal mode number ($m \sim 10 - 20$). The toroidal mode number is assumed to match the value of $q$ at the position of the

large pressure gradient, i.e., $n \sim 3 - 7$.

In JET, it was found recently that the ELMs show the same type of behavior as is found in the ASDEX tokamak. That is, a coherent exponentially growing precursor is observed prior to the broadband turbulent phase of the ELM itself. The precursors and the turbulent phases have been observed on both the magnetic signals and the density measurements from the reflectometer.

The ELMs occurring at low $\beta$ in DIII-D, ASDEX, and JET are similar in their dependence on the parameters influencing the resistivity, such as the heating power, or active cooling of the edge by gas puffing. The ELMs appear to be more unstable at high resistivity. From this, one can conclude that the precursors as observed in ASDEX, JET, and DIII-D (type-III) are likely to be resistive modes.

## 6.2 Resistive stability analysis of JET H-mode discharges

In the H-mode discharges in JET, the ELMs do not occur very often. The reason for this is not clear but is probably related to the higher edge temperature in the JET H-mode discharges as compared to other tokamaks. In this section we examine the MHD stability properties of a JET H-mode discharge (#23336) during which ELMs did occur. The time traces of the poloidal $\beta$, the total heating power, and the $H_\alpha$ signal for this discharge are shown in Fig. 6.2. The ELMs can be observed as large spikes on the $H_\alpha$ signal.

The equilibrium at the time slice $t = 55.0$ s is calculated with the IDENTD equilibrium reconstruction code [Blum86]. The time $t = 55.0$ s is chosen because the electron pressure profile as measured by the LIDAR diagnosticis is available at that time. The IDENTD code solves the Grad-Shafranov equation with the poloidal flux as measured by the 14 flux loops surrounding the plasma as a boundary condition. The two unknown equilibrium profiles $p(\psi)$ and $F(\psi)$ (see section 3.1) are determined by a least square fit of the solution of the Grad- Shafranov equation to the measured equilibrium data. In this case, the poloidal field as measured by the 18 magnetic field pickup coils and the electron pressure profile as measured by the LIDAR diagnostic are used. The resulting plasma shape and the surfaces of constant poloidal flux were shown in Fig. 6.1. The positions of the flux loops and the pickup coils are, respectively, indicated by the small circles and the rectangular boxes. The electron pressure profile from LIDAR and the profile obtained by the equilibrium reconstruction, shown in Fig. 6.3a, are in good agreement. The equilibrium profiles of the current density and the $q$-profile are shown in Fig. 6.3b. It should be stressed that the IDENTD equilibrium reconstruction

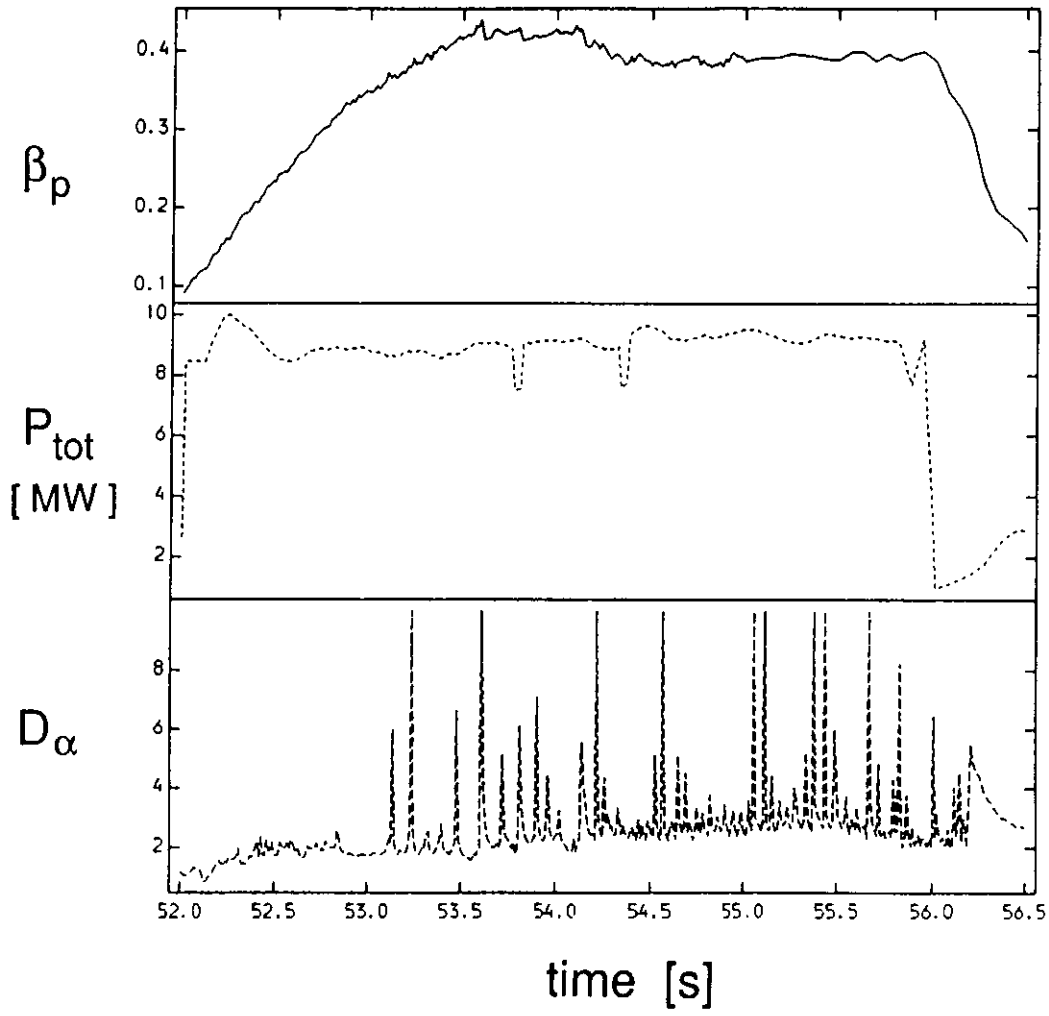


**Fig. 6.2** *The time traces of the poloidal $\beta$, the total heating power, and the $H_\alpha$ signal of discharge # 23336.*

can give only smooth pressure and current density profiles which are in global agreement with the measured profiles. The local gradients can be much larger than the reconstructed ones.

First, the reconstructed equilibrium is analyzed with respect to high-$n$ ballooning modes. For the calculation of the ballooning mode stability, we use the ideal MHD equilibrium and stability code, HBT [Goedbloed81, Huysmans90]. To determine how far the pressure gradient near the plasma boundary is from marginal stability to ballooning modes, the pressure gradient near the edge ($0.9 < s < 1.0$) is artificially increased up to the ballooning limit. It appears that the pressure gradient of the reconstructed equilibrium is at least a factor of 4 below the marginally stable pressure gradient at the edge. From this we may conclude that the ELMs in the JET H-mode discharges are not related to ideal high-$n$ ballooning modes.

Next, we try to establish the relevance of free boundary tearing modes in

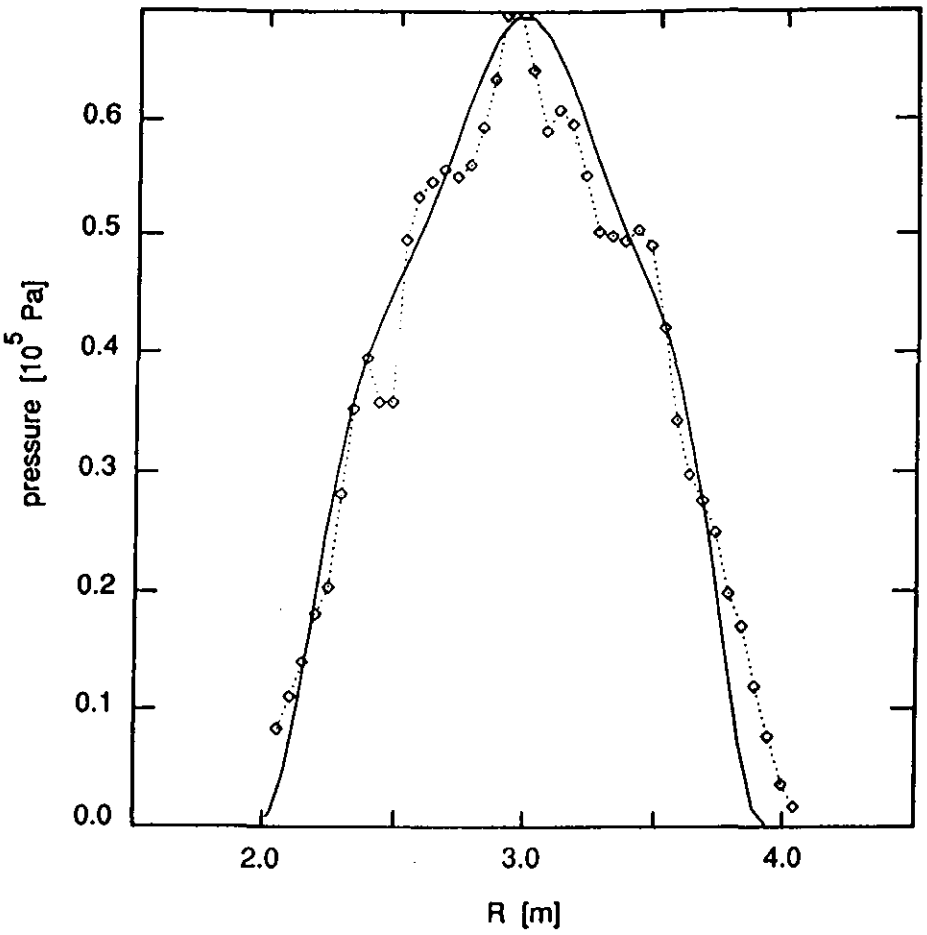


**Fig. 6.3a** *The electron pressure profile at $t = 55.0$ s as measured by the LIDAR diagnostic (dashed line with diamonds), and as obtained from the IDENTD equilibrium reconstruction (full curve).*

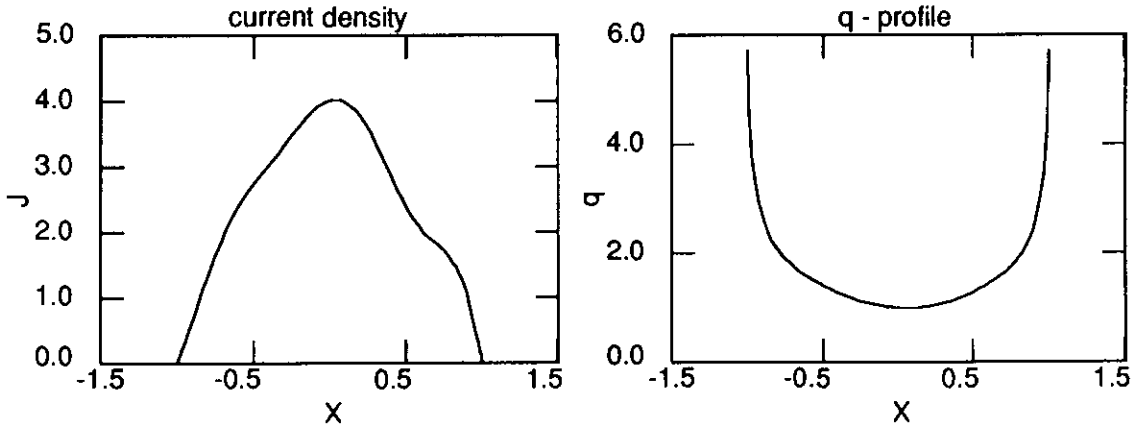


**Fig. 6.3b** *The equilibrium profiles of the current density and the safety factor $q$ as obtained by the IDENTD equilibrium reconstruction as a function of the normalized radius ($x$).*

explaining the linear precursor of the ELMs.

To calculate the growth rate of the resistive MHD modes, the equilibrium as reconstructed by the IDENTD code is reproduced with the HELENA equilibrium and mapping code (see chapter 3). The radial mesh of finite elements is packed near the plasma boundary for an accurate numerical representation of the equilibrium in the high shear region near the edge.

The growth rate of the $n = 1$ free boundary tearing mode of the actual JET discharge is shown by the lowest curve in Fig. 6.4 as a function of the resistivity. The ideally conducting wall is placed at 10 times the minor radius, the shape of the wall is the same as that of the plasma boundary. The eigenfunctions of the velocity perturbation corresponding to the mode at $\eta = 10^{-4}$ are shown in Fig. 6.5. The mode is shown at this relatively high value of $\eta$ to show the structure more clearly. The mode consists of many overlapping harmonics, with each harmonic having a maximum at the corresponding rational $q$-surface. The width of the different harmonics becomes smaller with decreasing resistivity, reducing the overlap of the harmonics.

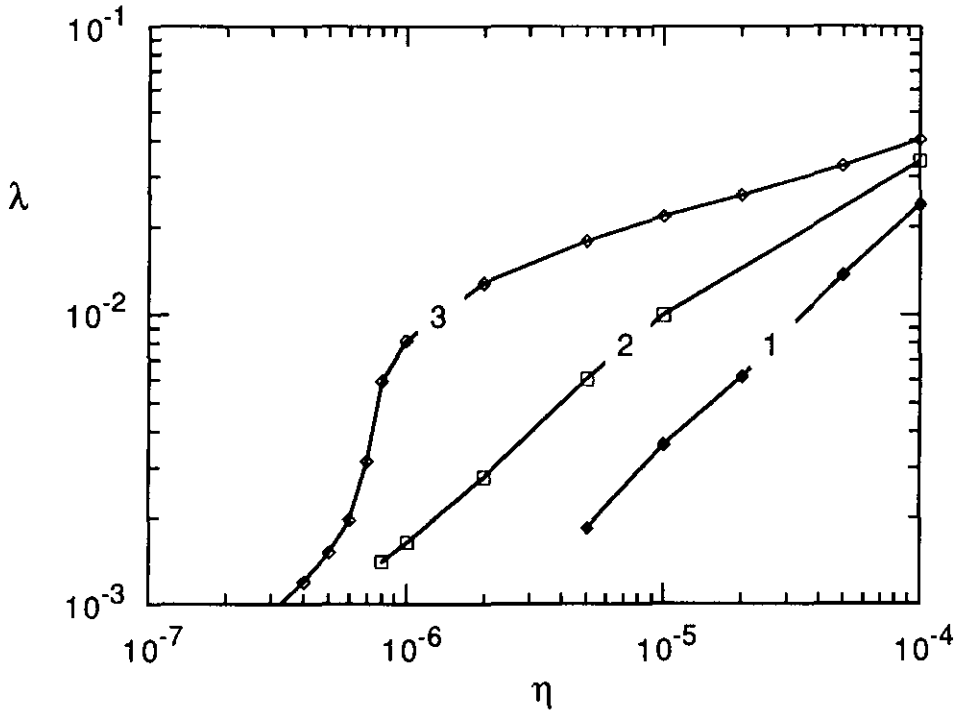


**Fig. 6.4** *The growth rate of the $n = 1$ free boundary tearing mode as a function of the resistivity for the three current density profiles shown in Fig. 6.6. The lowest curve, marked by (1), corresponds to the actual JET equilibrium. The labels (1), (2), and (3) correspond to the same labels in Fig. 6.6.*

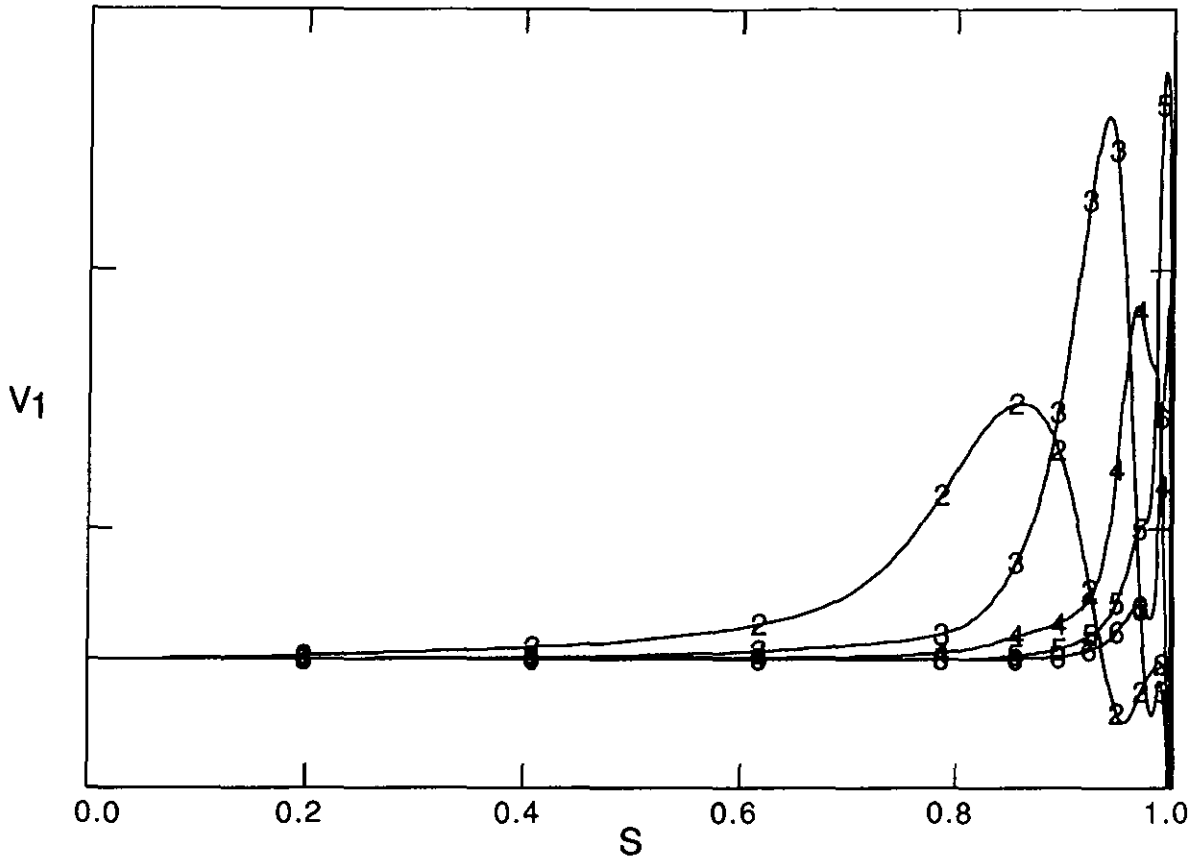


**Fig. 6.5** *The mode structure of the $n = 1$ free boundary tearing mode of the reconstructed JET H-mode equilibrium. Shown are the Fourier harmonics of velocity component normal to the fluxsurfaces, indicated by the numbers. The resistivity is* $10^{-4}$.

The scaling of the growth rate with resistivity is close to $\eta^{+1}$. If we extrapolate the growth rate to typical values of the resistivity near the edge, $\eta \sim 10^{-7} - 10^{-8}$ for a temperature of 500 eV, the growth rate is of the order $10^{-4} - 10^{-5}$ Alfvén times. This is far to slow to be of relevance. The mode will probably saturate nonlinearly at a small amplitude.

The possible driving forces of the ELM precursor are the current density gradient and the pressure gradient near the plasma boundary. The usual picture is that during the discharge the gradients gradually increase until the gradients exceed a critical value and an instability is triggered. However, one can also assume that the instability is triggered, not by a driving force becoming too large, but by the reduction of a stabilizing effect. For example, a tearing mode can be stabilized by the good average curvature in the presence of a pressure gradient and a low resistivity. The mode can then be triggered by an increasing resistivity due to,

for example, the build up of impurities. A combination of an increasing current density gradient and an increase in resistivity is also possible.

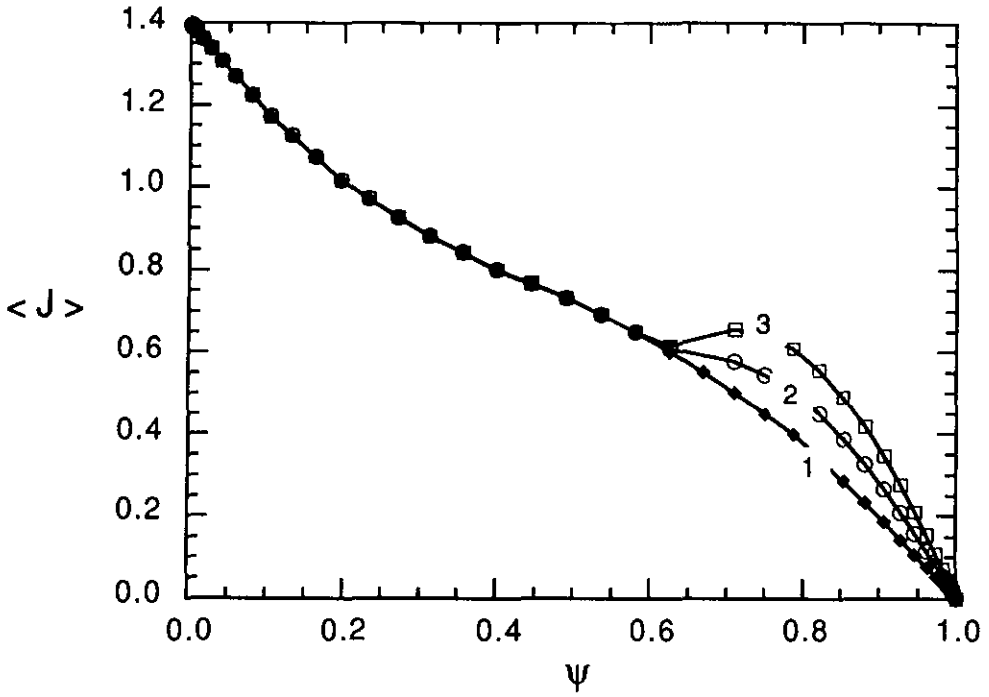


**Fig. 6.6** *The three profiles of the flux surface averaged toroidal current density as a function of $\psi$ as used in the stability analysis. The curve marked by (1) corresponds to the reconstructed JET equilibrium.*

To determine the dependence of the $n = 1$ tearing mode on its driving force, we have increased the current density gradient at the edge as compared to the actual reconstructed JET equilibrium. This is done by changing the $FF'(\psi)$ profile locally near the plasma boundary ($0.8 < \sqrt{\psi} < 1.$). The flux surface averaged toroidal current density for the original equilibrium and for two cases with an increased gradient are shown in Fig. 6.6. The pressure profile is kept constant. The growth rate of the free boundary $n = 1$ mode of the three cases are shown in Fig. 6.4 as a function of the resistivity. It is clear that the growth rate increases with an increasing current gradient at the edge. Also, the growth rate decreases more slowly with decreasing resistivity. For the case with the largest current gradients, however, we find a different behavior as a function of resistivity. For this case the growth rate shows a sharp decrease at $\eta = 10^{-6}$ which is due to the stabilization of the tearing mode by the good average curvature (see section 5.2). The eigenmode is similar to the eigenmode shown in Fig. 6.5.

To show that these modes are essentially free boundary modes, we have calculated the growth rate as a function of the distance between the ideally conducting wall and the plasma boundary. The results for the case with the largest current density gradient for a resistivity of $\eta = 10^{-5}$ are plotted in Fig. 6.7, showing that the growth rate of the tearing decreases if the wall is brought closer to the plasma. The mode is completely stabilized if the wall is closer than 1.1 times the minor radius.

As described above, the large decrease in growth rate with decreasing resistivity could well be related to the occurrence of the ELM precursor. However, the value of the current density gradient for which the mode has a significant growth rate and for which it shows the sharp decrease in growth rate with resistivity, is about a factor of two larger than the one that resulted from the equilibrium reconstruction.

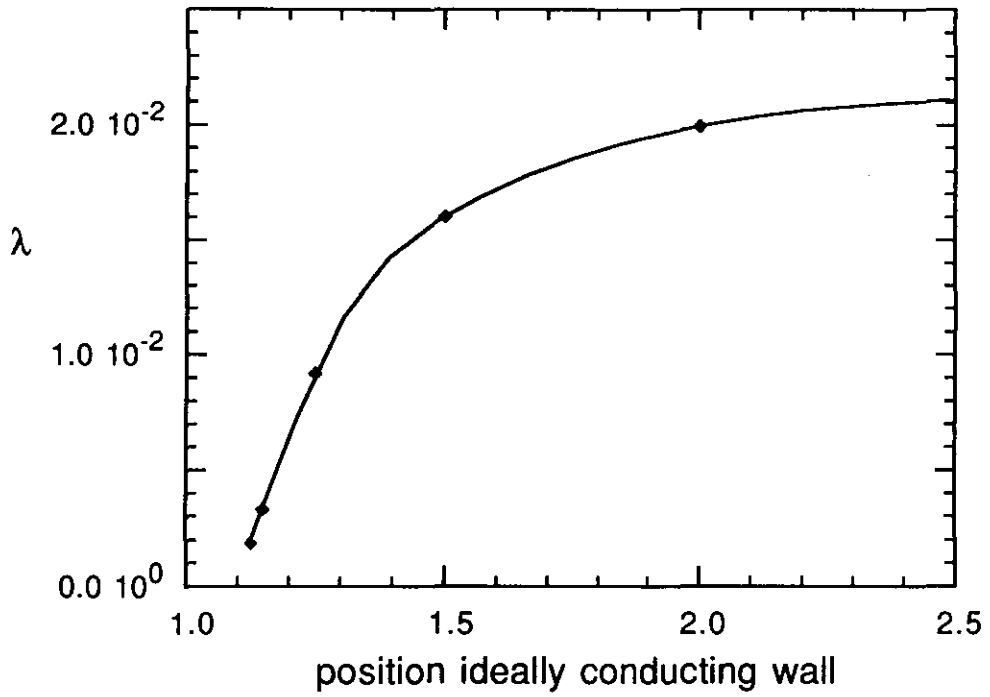


**Fig. 6.7** *The growth rate of the $n = 1$ free boundary tearing mode of the case with the largest current density gradient with $\eta = 10^{-5}$ as a function of the position of the ideally conducting wall. The wall position is given in units of the minor radius of the plasma. The wall positioned at 1.0 corresponds to the fixed boundary case.*

The effect of increasing the pressure gradient near the boundary on the tearing mode stability has been examined by locally increasing the pressure gradient

in the same way as was done for the current density profile. The flux averaged current density profile was kept fixed at profile (3) in Fig. 6.6. The poloidal beta is also fixed. At $\eta = 10^{-5}$, the effect of an increase in the pressure gradient with a factor of two with respect to the original JET equilibrium, is to reduce the growth rate of the $n = 1$ tearing mode by about a factor of two. A further increase in the edge pressure gradient has no influence on the growth rate. From this we can conclude that the pressure gradient has a stabilizing influence on the $n = 1$ tearing mode, even for relatively large pressure gradients.

## 6.3 Conclusion

The experimental data of the ASDEX, JET, and DIII-D tokamaks suggest that the ELM precursors as observed during the H-mode are resistive MHD modes. In this chapter we have analyzed the resistive stability of a JET H-mode discharge with respect to the $n = 1$ free boundary tearing mode, to establish the relevance of the tearing mode with respect to the ELM precursor.

It was shown that raising the current density gradient locally at the edge by a factor of two, as compared to the reconstructed JET equilibrium, an $n = 1$ tearing mode becomes unstable with a significant growth rate. This mode shows a sharp decrease in the growth rate with decreasing resistivity due to the stabilization by the average curvature and the pressure gradient. Unfortunately, there is a large uncertainty in the experimental determination of the current density profile. The limited number of parameters used for the representation of the equilibrium profiles in the equilibrium reconstruction leads to smooth global current density profiles. Locally large gradients of the current density will not be accurately reproduced. These large current density gradients can be due to the bootstrap current driven by the edge pressure gradient. In this way the pressure gradient would be destabilizing the $n = 1$ tearing mode, although in an indirect manner.

In this chapter we have discussed the $n = 1$ tearing mode. A more complete picture of the stability of the resistive low-n modes in the H-mode discharges would also require the $n = 2$ and $n = 3$ modes to be analyzed. For the higher $n$ modes, the influence of the pressure gradient is probably more destabilizing and the modes will be more like low-$n$ resistive ballooning modes.

In conclusion, although knowledge on the current density profile becomes increasingly available, the accuracy is not yet sufficient to prove or disprove the presence of local current gradients large enough to drive a free boundary resistive mode. Consequently, rather than confirming experimental results, the calculations presented are of a predictive nature, deriving conditions under which external resistive modes can be expected.

# 7 DAMPING OF GLOBAL ALFVEN WAVES DUE TO RESONANT ABSORPTION

The normal mode code CASTOR was also used for the spectral analysis of 2D fusion plasmas. Hereby, special attention was given to the continuous part of the ideal MHD spectrum of tokamak plasmas. For this purpose, a new numerical code, CSCAS, has been developed which turned out to be an indispensable tool for the study of the continuous part of the ideal MHD spectrum and of the so-called toroidicity-induced Alfvén eigenmodes, also called 'gap modes' because the frequencies of these global Alfvén modes are located in gaps in the continuous spectrum. We quantified the damping of such gap modes due to resonant absorption.

## 7.1 Introduction

The gross macroscopic properties of a plasma concerning equilibrium and stability are well described by the theory of magnetohydrodynamics (MHD). In tokamak discharges the plasma evolves through a sequence of MHD equilibria, where the maximum pressure is limited by the stability-, or beta-, limit given by ideal MHD. Non-ideal effects, such as resistivity or viscosity, allow development of slower and weaker instabilities and introduce finite damping in the system.

Additional plasma heating in the form of neutral beam injection or ion cyclotron resonance heating can introduce a strong anisotropy in the plasma pressure. A major effect of energetic ions generated by this heating is the destabilisation of marginally stable ideal MHD modes leading to a burst-like loss of these energetic particles. A prominent example of such an event is the fishbone instability. On the other hand, the interaction of energetic ions and a global MHD mode can lead to enhanced stability. The $m = 1$ mode has been studied extensively. For more details we refer to a recent review [Porcelli91].

Additional heating is not the only mechanism to generate energetic particles. The fusion of tritium and deuterium ions produces high-energy $\alpha$-particles. The confinement of these fusion born $\alpha$-particles is essential for ignition and hence for the possibility of generating energy by controlled fusion. It has been argued by [Cheng] that these $\alpha$-particles can destabilise global Alfvén modes and, hence, are lost by the particle-wave resonance. On the other hand, global Alfvén modes experience finite damping in such tokamak plasmas. Since the energetic particles are expected to excite global Alfvén waves, the corresponding energy can also get

heating. In order to find out whether the destabilisation of the global Alfvén waves by the $\alpha$-particles dominates the damping of these modes by phase-mixing, or vice versa, it is essential to obtain a deeper insight in the Alfvén spectrum of toroidal systems. Therefore, the ideal MHD continuous spectrum needs to be determined for such plasmas and the global Alfvén modes need to be studied in detail. Here, we discuss the results of our investigations of the poloidal mode coupling in the ideal MHD continuous spectrum, the interaction of the global Alfvén modes with the continuum modes, and the resulting damping of these modes by phase-mixing.

## 7.2 Toroidal Alfven Spectrum

### 7.2.1 Continuous spectrum

In ideal MHD the Alfvén spectrum of tokamak plasmas comprises both discrete and continuous spectra. The corresponding continuous "normal" modes are characterised by non-square integrable singularities. We have found an extremely convenient way for computing the continuous sub-spectra. This numerical method was applied to CASTOR which resulted in the program CSCAS. Details on the numerical method and on CSCAS are given in appendix C. The continuous spectra shown below, are all calculated by means of the program CSCAS.

The plasma density has been assumed constant so far. For the study of the toroidal Alfvén spectrum and the damping of gap modes due to resonant absorption, we introduced the following density profile in CASTOR and in CSCAS :

$$\rho_0(r) = \left\{1 - (1 - D)s^2\right\}^{\nu} , \tag{7.1}$$

determined by the two parameters $D$ and $\nu$. Hence, the density at the plasma surface is given by $D^{\nu}$.

We first consider a circular cross-section equilibrium with aspect ratio $\epsilon^{-1} = 2.5$, a safety factor increasing monotonically from $q_0 = 1.10$ on the magnetic axis to $q_S = 2.66$ at the plasma surface (as indicated in Fig. 7.1a) and with a small pressure $\beta_p \approx 2\%$ and $\beta \approx 0.06\%$. The density is only slightly varying with $D = 0.5$ and $\nu = 2$ in Eq. (7.1). The toroidal wave number is chosen as $n = -1$ and five poloidal harmonics are included, viz. $m = 0$, 1, 2, 3, and 4. Part of the continuous spectrum is displayed in Fig. 7.1a. The profiles of the local Alfvén frequencies are shown in dependence of the radial coordinate $s$. The dominant poloidal Fourier harmonic is indicated on each continuum branch. The slow magnetosonic continua are in this case close to the origin (as a consequence of the considered low plasma

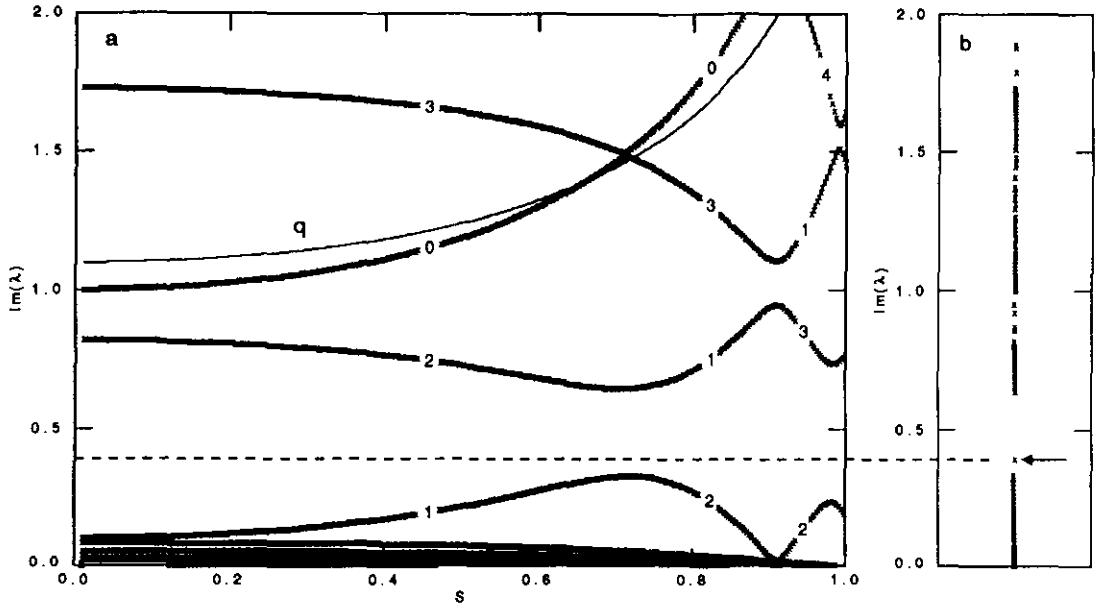


**Fig. 7.1** *a) The ideal MHD continuous spectrum, in particular local Alfvén and slow magnetosonic frequencies versus s for a circular cross-section toroidal plasma with* $\epsilon = 0.4$, $q_0 = 1.10$, $q_S = 2.66$, *and* $\beta_p \approx 2\%$. *The density varies according to Eq. (7.1) with* $D = 0.5$ *and* $\nu = 2$. *The wave numbers are chosen as* $n = -1$, *and* $m = 0,1,2,3$, *and 4. b) Corresponding part of the full ideal MHD spectrum as obtained by using CASTOR* ($N_\psi = 21$, *same wave numbers).*

pressure), whereas the frequencies of the Alfvén continuum modes readily exceed unity.

The branch of the predominantly $m = 1$ (or $m = 2$) mode extends with increasing $s$ from $Im(\lambda) = 0.10$ to $Im(\lambda) = 1.64$ (or from $Im(\lambda) = 0.82$ to $Im(\lambda) = 0$). There is a finite gap around $Im(\lambda) \approx 0.5$ induced by poloidal mode coupling. The mode coupling between the $m = 1$ and $m = 2$ components is the strongest at $s = 0.72$, where the safety factor is $q = 1.50$. The resulting gap in the continuous spectrum reaches from $Im(\lambda) = 0.33$ to $Im(\lambda) = 0.65$. In the cylindrical limit ($\epsilon = 0$) this coupling between the $m = 1$ and the $m = 2$ mode vanishes producing two independent continua for $m = 1$ and $m = 2$ with a degenerate continuum frequency at the rational surface where $q = 1.50$. Near the plasma boundary, at the rational surface where $q = 2.5$ ($s = 0.98$), toroidicity-induced poloidal mode coupling between the $m = 2$ and the $m = 3$ modes causes a similar 'avoided crossing' in the continuum branches of the predominantly $m = 2$ and 3 components. The resulting gap in the continuous spectrum overlays the previous one and reaches from $Im(\lambda) = 0.23$ to $Im(\lambda) = 0.73$. Three other

gaps are visible in the window shown in Fig. 7.1a, one around $Im(\lambda) = 1.0$ and two around $Im(\lambda) = 1.5$. These gaps are much smaller than the previous ones because they result from the coupling of 'non-neighbouring' poloidal modes, i.e. $|m-m'| \neq 1$. As the mode coupling is gradually weaker with increasing $|m-m'|$, the corresponding gaps are gradually smaller. The gap at $s = 0.91$, for instance, is due to the coupling of the $m = 1$ and 3 harmonics, which is strongest at $q = 1.0$. This gap is smaller than the previous ones : it reaches from $Im(\lambda) = 0.94$ to $Im(\lambda) = 1.11$. Still smaller are the two gaps around $Im(\lambda) = 1.5$ : one at $s = 0.72$, reaching from $Im(\lambda) = 1.48$ to $Im(\lambda) = 1.50$, and one at $s = 0.98$, reaching from $Im(\lambda) = 1.51$ to $Im(\lambda) = 1.60$. These gaps are due to the next higher order in the mode coupling, namely between the $m = 0$ and 3 components at $s = 0.72$ (where $q = 1.5$) and between the $m = 1$ and 4 harmonics at $s = 0.98$ (where $q = 2.5$).

Fig. 7.1b displays the corresponding part of the full ideal MHD spectrum computed with CASTOR with only 21 radial grid points and for the same poloidal mode numbers. Of course, CASTOR can not determine the internal structure of the continuous spectrum, i.e. the radial profiles of the local Alfvén frequencies. Instead, the projection of these profiles on the imaginary $\lambda$-axis is obtained with CASTOR. The continuous part of the spectrum as well as the related gap structure corresponds satisfactorily for the two procedures. For a full agreement, of course, the same number of radial grid points should be provided in both procedures, which would require the inverse iteration technique for one eigenvalue at a time as the QR algorithm, which diagonalises the entire matrix, is then no longer applicable because of its enormous memory requirements. Nevertheless, it is evident from Fig. 7.1a and b that the two spectra agree well on the continuum branches. The apparent discrepancy near $Im(\lambda) \leq 0.94$ and 2.0 is due to the coarse grid in the complete solver using only $N_\psi = 21$ grid points and thereby resolving only few continuum modes. For Fig. 7.1a the reduced eigenvalue problem was solved on 400 (equidistant) magnetic flux surfaces.

### 7.2.2 Discrete global modes

Inspection of the location of the singular surfaces of the continuum modes reveals indeed full agreement with the sub-spectra in Fig. 7.1a. This confirms the existence of "forbidden zones" in the eigenvalue plane as can be established easily in the large-aspect ratio limit by keeping at least two Fourier harmonics. Fig. 7.1b reveals, in addition, the existence of discrete global modes within these forbidden zones, here for $Im(\lambda) = 0.39$ and $Im(\lambda) = 0.95$. The Real part of the

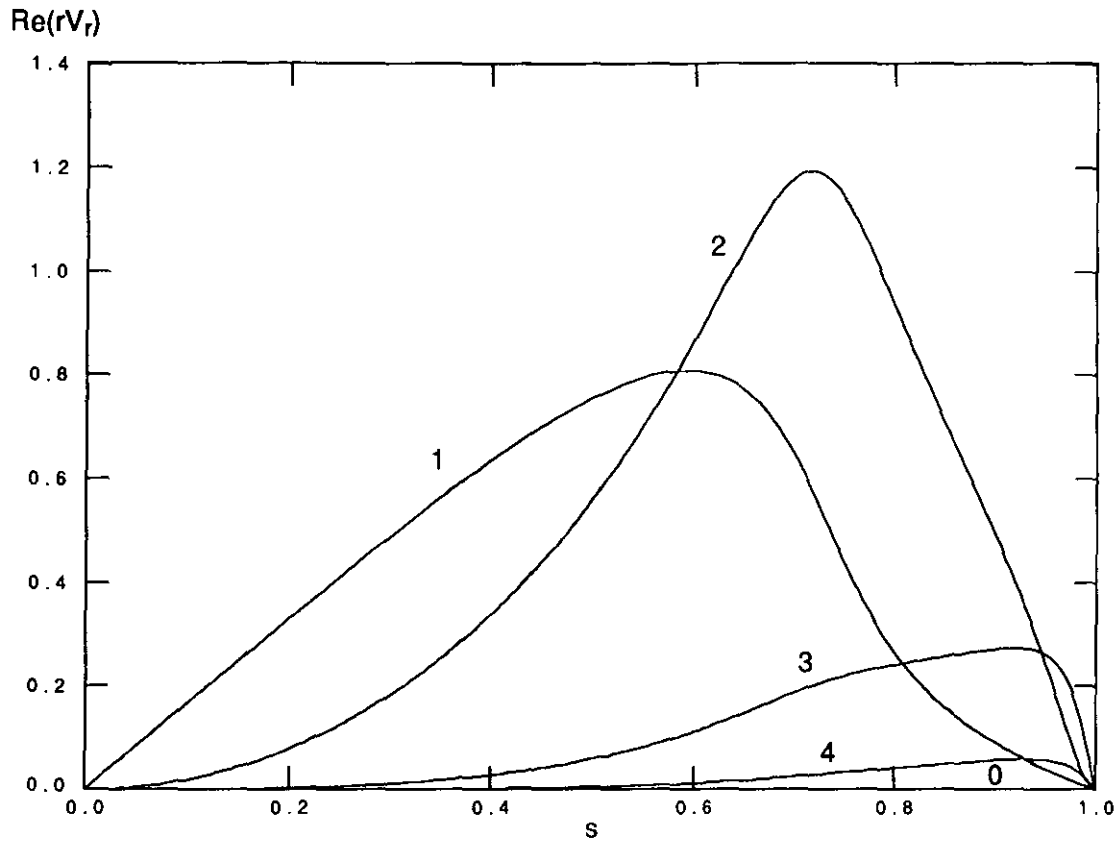


**Fig. 7.2** *Radial dependence of the Fourier harmonics of the $rv_r$-component of the eigenfunction of the discrete Alfvén mode with a frequency located in the basic gap shown in Fig. 7.1 (as indicated in Fig. 7.1b).*

$rv_r$-component of the eigenfunction of the discrete Alfvén mode in the basic gap is shown in Fig. 7.2. In addition to the expected $m = 1$ and 2 components the $m = 3$ and 4 components show up too, with a smaller amplitude due to the small aspect ratio ($\epsilon = 0.4$). It is evident that the discrete gap mode extends throughout the plasma. This indicates that the mode coupling allows the construction of discrete normal modes, which avoid the jumps and singularities that are present in the cylindrical limit ($\epsilon^{-1} = \infty$) and which satisfy the boundary conditions. An immediate conclusion is that there should be more than one discrete global mode with this property as many poloidal modes couple. We expect an entire class of global Alfvén modes with increasing number of radial nodes. On the other hand, not in every gap such a global mode occurs. Gap modes only appear when the poloidal mode coupling is strong enough. For instance, in Fig. 7.1 such a mode is missing in the small gap ('small' because of weak mode coupling) around $Im(\lambda) = 1.5$. But, as we will see, even with strong mode coupling the resulting

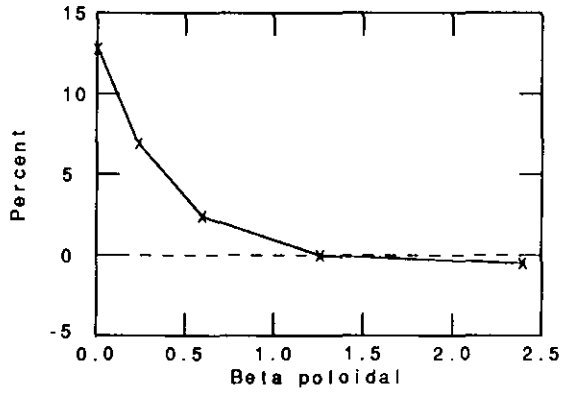


**Fig. 7.3** *Relative distance of the frequency of the gap mode from the lower edge of the gap versus the (poloidal) plasma beta. Here* $\epsilon = 0.4$, $q_0 = 1.2$, $D = 0.01$, $\nu = 2$, $n = -1$, *and* $m$ *=0, 1, 2, 3, and 4.*

gaps can be 'empty'.

The frequencies of these discrete gap modes and, hence, the position of these frequencies in the gaps, depend clearly on the specific equilibrium. By changing the equilibrium parameters, for instance by increasing the pressure and/or by decreasing the inverse aspect ratio $\epsilon^{-1} \longrightarrow 1.0$, the eigenvalue corresponding to the gap mode can even be 'pushed' outside the gap. This is demonstrated in Fig. 7.3 where a set of equilibria is considered with increasing pressure. In Fig. 7.3 the relative distance of the gap mode frequency to the lower edge of the gap in which it is located, is displayed versus the poloidal plasma beta, $\beta_p$, of the equilibrium. It is seen that the gap mode shifts towards the lower edge of the gap as the plasma pressure is increased. For $\beta_p = 1.27$ the mode sits on the lower edge of the gap and for still higher plasma pressure disappears out of the gap into the continuous spectrum where it couples to the continuum modes.

In order to demonstrate the other extreme, namely the fact that a single gap can contain more than one global mode at once, we found it more effective to vary the aspect ratio. We enhanced the poloidal mode coupling due to toroidicity by increasing the toroidicity effect, i.e. by increasing the inverse aspect ratio of the equilibrium. As a result of the increasingly stronger mode coupling the gap size gradully increases as illustrated in Fig. 7.4, where the lower and upper edges of the basic gap are plotted versus the inverse aspect ratio $\epsilon$. Also indicated here are the corresponding frequencies of the discrete gap modes found in this gap. When the gap is wide enough, i.e. when the poloidal mode coupling is strong enough, a second gap mode appears in the basic gap. For the case shown in Fig. 7.4 this

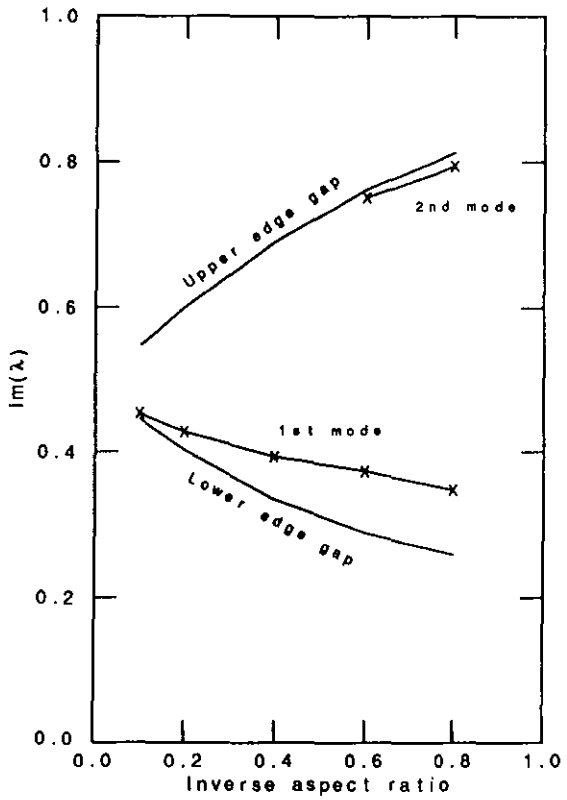


**Fig. 7.4** *Width of the basic ($m = 1$ and 2) gap and frequencies of discrete gap modes therein versus the inverse aspect ratio. The other parameters are chosen as $q_0 = 1.05$, $D = 0.5$, $\nu = 2$, $n = -1$, and $m$ =0, 1, 2, 3, and 4.*

happens for $\epsilon = 0.6$. We made a convergence study of the frequency of this second gap mode for $\epsilon = 0.8$, both in $N_\psi$ and $N_m$, in order to check whether this second gap mode is not an artefact caused by a too low resolution or a too small number of Fourier harmonics (for $\epsilon = 0.8$ the poloidal mode coupling is quite strong and 5 modes do not suffice to represent the mode accurately). We went up to 100 radial intervals and 11 Fourier components ($m = -3 \rightarrow 8$) and obtained full convergence with the frequency still in the gap which proves that there are indeed two modes in this gap. The second gap mode looks different than the first one which looks very similar to the mode shown in Fig. 7.2. The dominant $m = 2$ component of this mode has one radial node in the $rv_r$-component in contrast to the first gap mode. This mode also has a different parity in the Fourier harmonics. For the mode shown in Fig. 7.2, all coefficients of the Fourier harmonics have the same sign whereas for the second gap mode, these signs are not all the same. The same applies to the other components of the eigenfunction. The $m = 2$ contribution is dominant and all coefficients of Fourier modes with $m > 2$ have the same sign as the $m = 2$ component, while those of the harmonics with $m < 2$ all have the

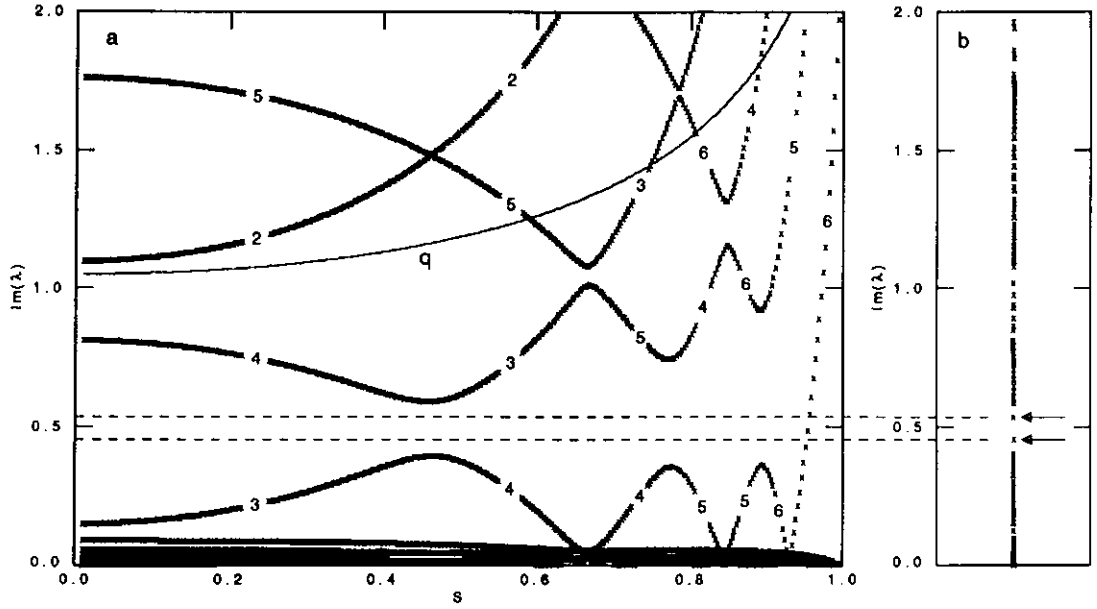


**Fig. 7.5** *a) Structure of the ideal-MHD continuous spectrum for $n = -3$ and $m$ =2, 3, 4, 5, and 6, $q = 1.05$ and a density profile given by Eq. (7.1) with $D = 0.05$ and $\nu = 1$. b) Corresponding part of the full ideal-MHD spectrum obtained by using CASTOR ($N_\psi = 21$).*

opposite sign.

### 7.2.3 High-$n$ cases

A gradually more complex gap structure emerges in the continuous spectrum for a stronger magnetic shear, stronger density variation and higher toroidal mode number. Again the circular cross-section tokamak with aspect ratio $\epsilon^{-1} = 2.5$ is analysed having small pressure and a safety factor increasing from $q_0 = 1.05$ on axis to $q_S = 2.54$ on the surface. Now, the toroidal wave number is chosen as $n = -3$ and the poloidal wave numbers are $m = 2, 3, 4, 5$, and 6. The density profile considered here is given by equation (8) with $D = 0.05$ and $\nu = 2$. The continuum structure and the corresponding part of the entire ideal-MHD spectrum are shown in Figs. 7.5a and 7.5b, respectively. The $q(\psi)$-profile is also indicated in Fig. 7.5a. Again, the numbers on the continuum branches indicate the dominant Fourier harmonic for that continuum branch. Three overlaying gaps with $Im(\lambda) \approx 0.5$ occur : near $s = 0.47$ where $q = 7/6$ and $m = 3$ and 4 couple strongly, near $s = 0.78$ where $q = 1.5$ and $m = 4$ and 5 couple strongly, and near $s = 0.89$ where $q = 11/6$ and $m = 5$ and 6 couple strongly. From Fig. 7.5b it is clear that two discrete, global Alfvén waves exist in these gaps. The ideal MHD eigenfrequencies

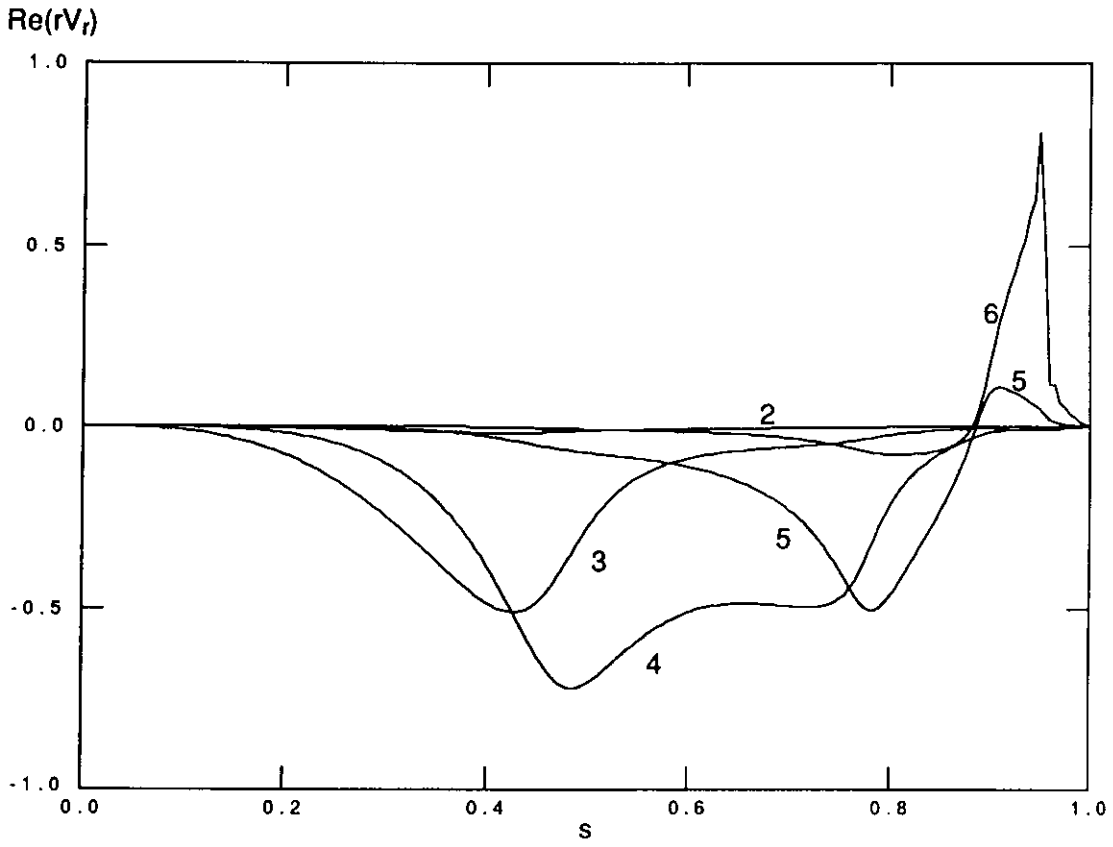


**Fig. 7.6** *Radial dependence of the Fourier harmonics of the real part of the $rv_r$-component of the gap mode with $Im(\lambda) = 0.46$ as indicated in Fig. 7.5b.*

of these two modes are indicated in Fig. 7.5b and the $rv_r$-components of the eigenfunction corresponding to the one with the lowest frequency is displayed in Fig. 7.6. Two other gaps occur around $Im(\lambda) = 1.0$ due to the coupling of the $m = 3$ and 5 modes (at the $q = 4/3$-surface) and the $m = 4$ and 6 modes (at the $q = 5/3$-surface). The calculation of the ideal MHD spectrum by means of the QR algorithm seems to suggest the existence of a global wave inside the $m = 3, m = 5$ gap (see indication on Fig. 7.5b). This, however, is a consequence of the low spatial resolution imposed by the enormous memory requirements of the QR algorithm. An inverse vector iteration with higher resolution ($N_\psi = 101$) reveals that the indicated frequency corresponds to a continuum mode and not to a global mode. Indeed, the $m = 4$, 5 and 6 continuum branches in the outer part of the plasma cover the $m = 3, m = 5$ gap at the $q = 4/3$-surface (see Fig. 7.5a). The low spatial resolution used to produce Fig. 7.5b is responsible for the bad representation of these continuum branches. Hence, only two gap modes are found in this configuration. In contrast to the previously shown gap modes, these global

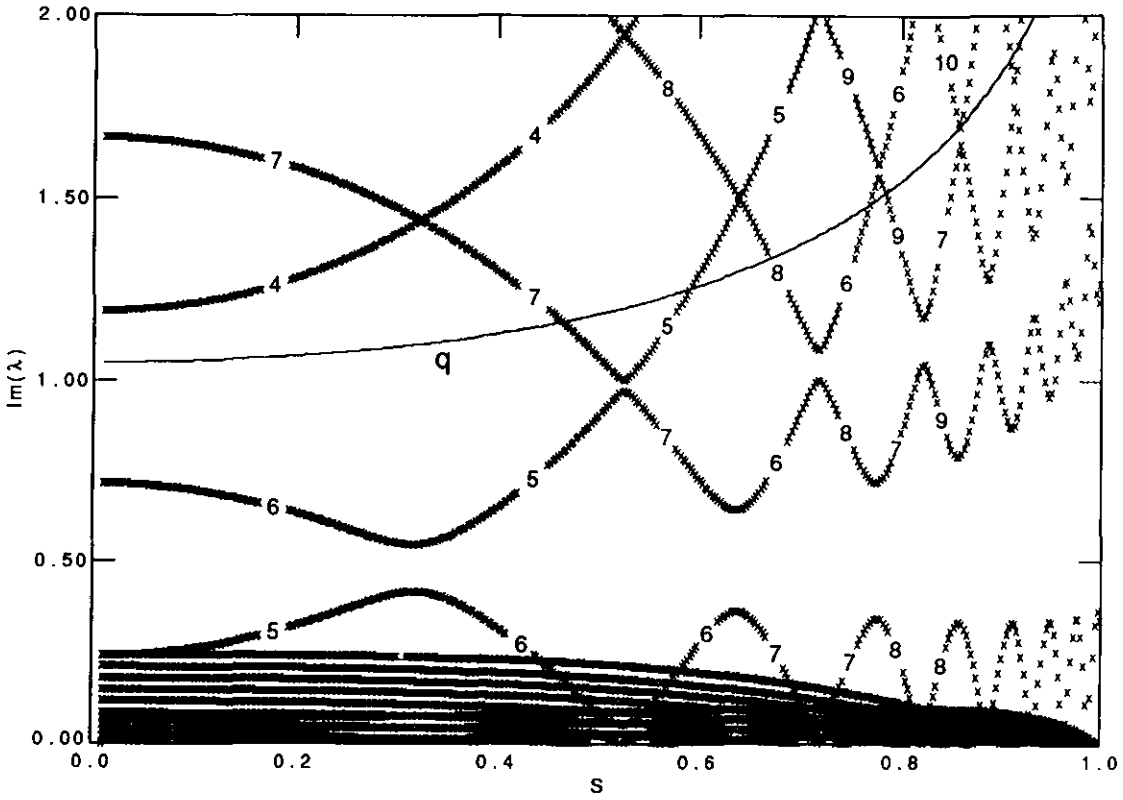


**Fig. 7.7** *Structure of the ideal-MHD continuous spectrum for* $n = -5$ *and* $m = 3 \rightarrow 13$, $q_0 = 1.05$ *and a density profile given by Eq. (7.1) with* $D = 0.1$ *and* $\nu = 1$.

modes interact now with the continua because the gaps in which they are located are now overlayed by one or more continuum branches which is a consequence of the steep density profile near the plasma surface ($D = 0.05$). The two discrete global modes in the lower gaps both exhibit a singular $m = 6$ component due to coupling to the $m = 6$ continuum branch that is overlaying these gaps (see Fig. 7.5a), whereas the regular gap modes are mainly due to coupling of the $m = 3$ and 4 and of the $m = 4$ and 5 harmonics, respectively. The consequences of the coupling between the discrete global modes and the (singular) continuum modes, yielding singular parts in the eigenfunctions, is discussed in the next Section.

An even more pronounced gap structure is obtained for $n = -5$ as shown in Fig. 7.7. Here the equilibrium parameters are chosen such that the interaction of the gap modes with the continua are not pronounced. In Fig. 7.7 many more gaps occur as compared to the previously shown continua. This is a consequence of the higher $|\ n|$-value. Remember that the gaps occur in toroidal plasmas on the rational surfaces where $q = -(m + m')/2n$ as a result of the cancellation of the one-dimensional degeneracies on those surfaces. For higher $n$-values there are

gradually more of such rational surfaces and, hence, there are gradually more gaps in the continuous spectrum. In Fig. 7.7 even 8 overlying gaps occur around $Im(\lambda) = 0.5$ due to coupling of the $m = 5$ and the $m = 6$ branch at $s = 0.32$ (where $q = 11/10$), the $m = 6$ and the $m = 7$ branch at $q = 13/10$, etc. The same scenario is repeated around $Im(\lambda) = 1.0$ due to the (higher order) coupling of dominant modes with a poloidal mode number that differs by 2 ($m = 5$ and 7, 6 and 8, etc.). Notice also in Fig. 7.7 that the width of the gaps depends clearly on the magnetic shear : the gap size increases with increasing $q$-values.

The findings of this Section reveal that for tokamak configurations there exist gaps, i.e. forbidden eigenvalues, in the ideal MHD continuous spectrum. These gaps are due to toroidal effects which couple continuum branches with different poloidal wave numbers $m$ and $m'$. This coupling is the strongest at the rational surfaces where the corresponding one-dimensonal continuum frequencies are degenerate, i.e. where $q = -(m + m')/2n$. The effect of the mode coupling is to cancel these degeneracies which results in 'crossing avoidances' and, hence, gaps. In addition, there exists a class of discrete global Alfvén modes with eigenfrequencies within these gaps due to toroidal coupling.

## 7.3 Damping of Global Alfven Waves

Regular discrete Alfvén modes possess a well defined frequency and in such a mode every part of the plasma oscillates with this particular frequency. For a continuum mode, on the other hand, it holds that the normal component of the velocity is damped like $1/t$ :

$$v_n \sim \omega_A e^{-\omega_A t}/t, \tag{7.2}$$

whereas the tangential components execute undamped oscillations :

$$v_t \sim -i(\omega_A \omega'_A/k_\perp)e^{-\omega_A t}. \tag{7.3}$$

These components undergo completely uncoordinated oscillations, where each plasma layer oscillates with its own local Alfvén frequency. If the plasma is continuously excited periodically at such a continuum frequency, phase-mixing takes place until eventually after a time $\tau_{SS}$ a steady state is reached and the entire plasma

oscillates with the same driving frequency $\omega = \omega_d$. As a consequence of the phase-mixing, the oscillation of neighbouring flux surfaces with different local Alfvén frequencies gets out of phase and large gradients build up around the plasma layer where the local Alfvén frequency matches the frequency of the external driver. In this resonant layer dissipative effects become important. Hence, the damping of Alfvén waves by phase-mixing is essentially due to the inhomogeneity of the equilibrium in ordinary space and is analogous to Landau damping which results from the inhomogeneity of the equilibrium in velocity space. The efficiency of plasma heating by phase-mixing or resonant absorption is completely determined by the presence of global discrete modes with a frequency in the range of the ideal continuous spectrum. These modes play the role of energy-carrier and transport the energy supplied by the external source from the plasma surface, through the magnetic surfaces, to the resonant layer. As shear Alfvén waves propagate only along magnetic field lines, resonant absorption is highly inefficient without such a damped global mode. Since the ideal MHD differential operator is Hermitian, there exist no eigenfrequencies with both a non-vanishing real and imaginary part. Therefore, this mode of plasma oscillation does not correspond to a normal mode in ideal MHD and is consequently called a "quasi-mode" or "collective mode". In a previous paper [Poedts91] it has been shown that the ideal quasi-modes correspond to weakly damped eigenmodes of the resistive-MHD differential operator. Moreover, in the limit of vanishing plasma resistivity, the damping of these resistive eigenmodes remains finite and becomes independent of the plasma resistivity. Hence, these resistive eigenmodes converge to their ideal-MHD analogues in the limit of vanishing $\eta$. It is emphazised that this does not hold for the Alfvén continuum modes. In resistive MHD, the ideal continuum is replaced by a set of discrete resistive eigenvalues which lie on well-defined curves in the complex $\lambda$-plane. With a finite number of exceptions these resistive eigenmodes do not converge to the ideal MHD continuum modes in the limit of asymptotically small resistivity.

In the following we will construct global Alfvén modes interacting with continuum modes by choosing the equilibrium parameters such that there is a continuum branch overlaying the gap, so that the gap mode frequency corresponds to the local Alfvén frequency of at least one magnetic surface. In analogy to the calculation in cylindrical geometry the singularity in the equations is removed by including finite resistivity. Again, the resulting damping is determined by computing $Re(\lambda)$ in a resistive plasma and then decreasing the plasma resistivity. Since the damping becomes independent of the actual value of the resistivity in the limit of vanishing $\eta$, we are again dealing with quasi-modes but this time in toroidal

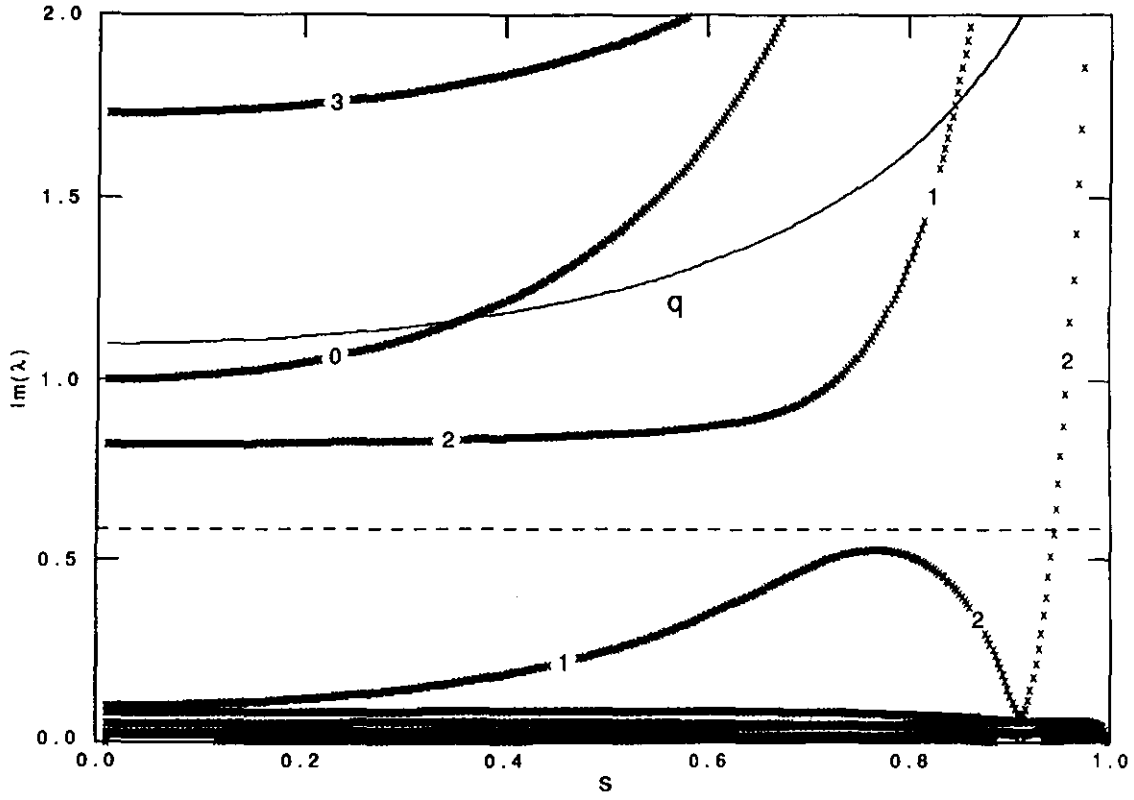


**Fig. 7.8** *Structure of the ideal-MHD continuous spectrum for* $n = -1$ *and* $m = 0 \rightarrow 4$, $q_0 = 1.10$ *and a density profile given by Eq. (7.1) with* $D = 0.01$ *and* $\nu = 2$.

systems. It has been shown above how the gap structure is changed by varying the magnetic shear and the density profile. By changing the constant $D$ for the equilibrium studied in Fig. 7.1 from $D = 0.5$ to $D = 0.01$, the density decreases strongly in the outer part of the plasma causing a strong increase in the local Alfvén frequency. The resulting gap structure is displayed in Fig. 7.8. There is only one gap visible in the window shown in Fig. 7.8. It results from a crossing avoidance of the two continuum branches with, respectively, $m = 1$ and $m = 2$ as dominant Fourier harmonic and extending from $Im(\lambda) = 0.525$ to $Im(\lambda) = 0.819$. A global Alfvén mode is found with $Im(\lambda) = 0.58$ (in the gap). Notice, however, that due to the strong density decrease in the outer part of the plasma, the $m = 2$ branch increases again in this part of the plasma and overlays the gap. As a result, the gap mode frequency matches now a continuum frequency on the $m = 2$ branch near the boundary. Next, it has to be examined how the results and, in particular, the damping that follows from the coupling to the continuum modes, depend on the actual value of $\eta$. In Fig. 7.9 a convergence study of the damping ($| Re(\lambda)|$) of the gap mode indicated in Fig. 7.8 is presented. This figure

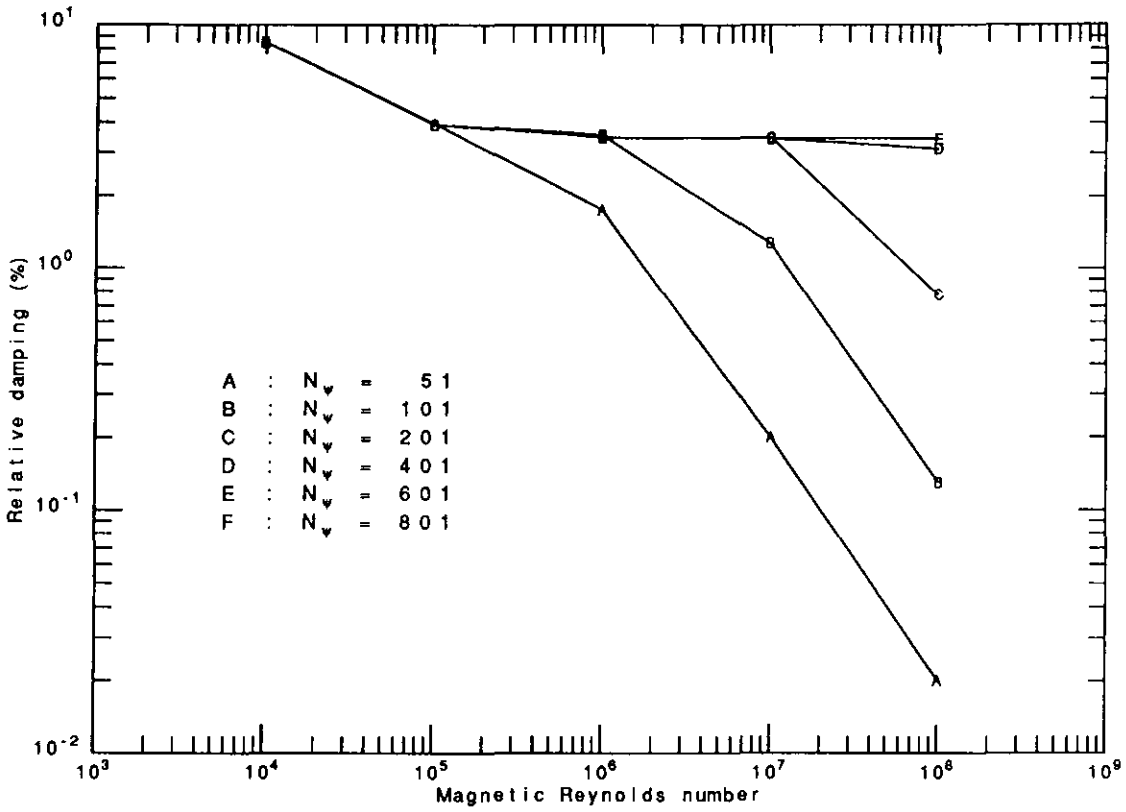


**Fig. 7.9** *Relative damping versus plasma resistivity for the mode indicated in Fig. 7.8 and for different values of $N_\psi$. This convergence study shows the need for a sufficiently high resolution in the resistive layer in order to get the damping correct.*

shows in fact two kinds of convergence at once, viz. convergence of the damping for $\eta \longrightarrow 0$ and, for each value of $\eta$, convergence with respect to the $N_\psi$. The plasma resistivity $\eta$ was varied over four orders of magnitude from $10^{-4}$ to $10^{-8}$ and the damping has been computed with 51, 101, 201, 401, 601, and 801 spatial grid points in radial direction for each value of $\eta$. It is clear that sufficiently many radial mesh points are required for properly resolving the (nearly-singular) layer around $s = 0.94$. It is also clear that this resolution has to be higher for lower values of the plasma resistivity since the layer is narrower than. This qualitative picture is indeed confirmed and quantified in Fig. 7.9. For $\eta = 10^{-4}$ and $10^{-5}$, 51 radial grid points are sufficient and increasing the resolution just yields exactly the same damping. For $\eta = 10^{-6}$, however, 101 radial mesh points are needed to get the damping right and for $\eta = 10^{-7}$ we need $N_\psi \geq 201$. For $\eta = 10^{-8}$ the damping becomes idependent of the spatial resolution for $N_\psi \geq 601$. The oscillatory frequency stays at $Im(\lambda) = 0.58$ and the real part of the frequency converges to $Re(\lambda) = -1.99 \times 10^{-2}$, thus the relative damping factor, defined as

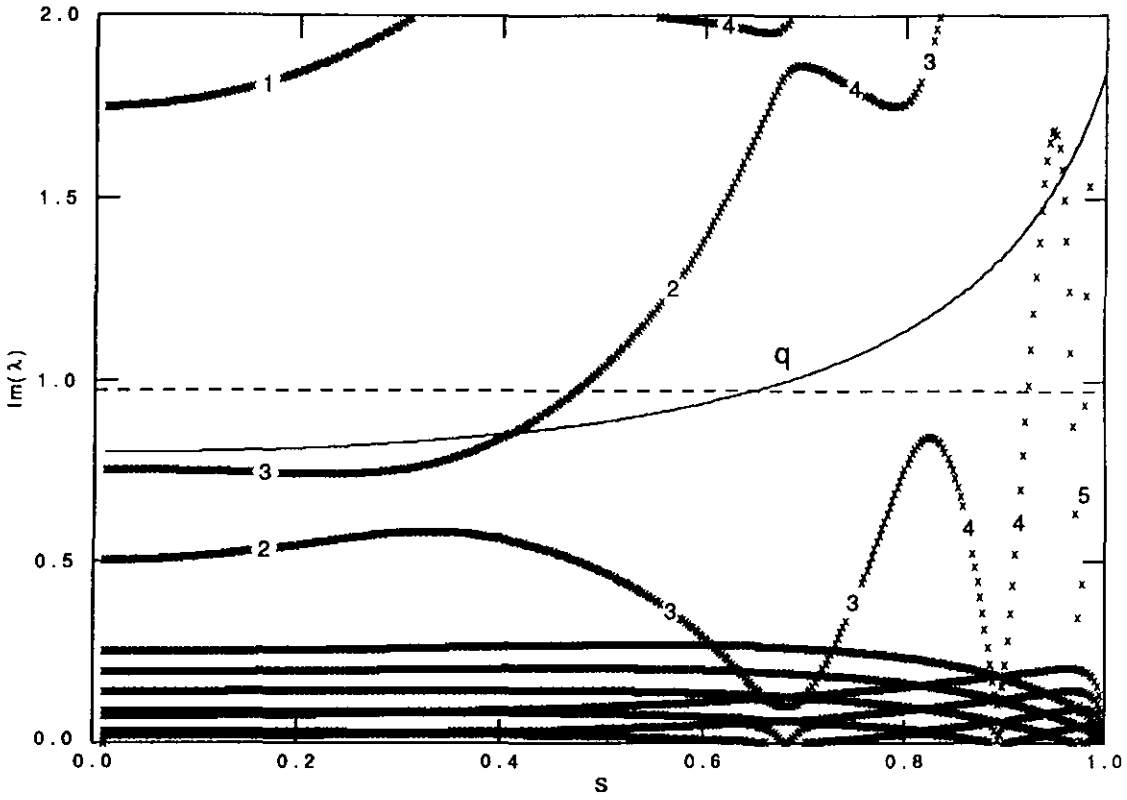


**Fig. 7.10** *Structure of the ideal-MHD continuous spectrum for* $n = -3$ *and* $m = 1 \rightarrow 7$, $q_0 = 0.8$ *and a density profile given by Eq. (7.1) with* $D = 0.01$ *and* $\nu = 2$.

$\delta = |\frac{Re(\lambda)}{Im(\lambda)}|$, is 3.4%. It is evident that we have a well defined result for $\eta \leq 10^{-6}$.

So far the possible strong damping for global toroidal Alfvén waves has been demonstrated. When this mode is excited by energetic particles the absorption of the corresponding energy takes place near the plasma boundary in the two simulations shown so far. It is natural to conjecture that this absorption should also occur near the centre, if the equilbrium profiles are chosen such that a resonance can occur there. An interesting configuration is generated by choosing $q$ on axis as $q_0 = 0.8$ and $q_S = 1.84$ in the previously examined low pressure equilibrium with the density sharply falling at the edge, $D = 0.01$ and $\nu = 2$ in Eq. (7.1). When the toroidal wave number is $n = -3$ and the poloidal harmonics $m = 1$ to 7 are included, the corresponding toroidal continua yield a wide gap around $s \approx 0.8$ where $q = 1.16$. This gap is generated by the strong coupling of the $m = 3$ and 4 Fourier harmonics. This coupling should take place for $q = -(m + m')/2n = 7/6 = 1.16$, which is indeed confirmed by the results shown in Fig. 7.10. A global Alfvén mode exists with an eigenvalue $Im(\lambda) \leq 0.96$ well within this gap. This global mode interacts with the $m = 2$ continuum branch at $s = 0.47$, with the $m = 4$ contin-

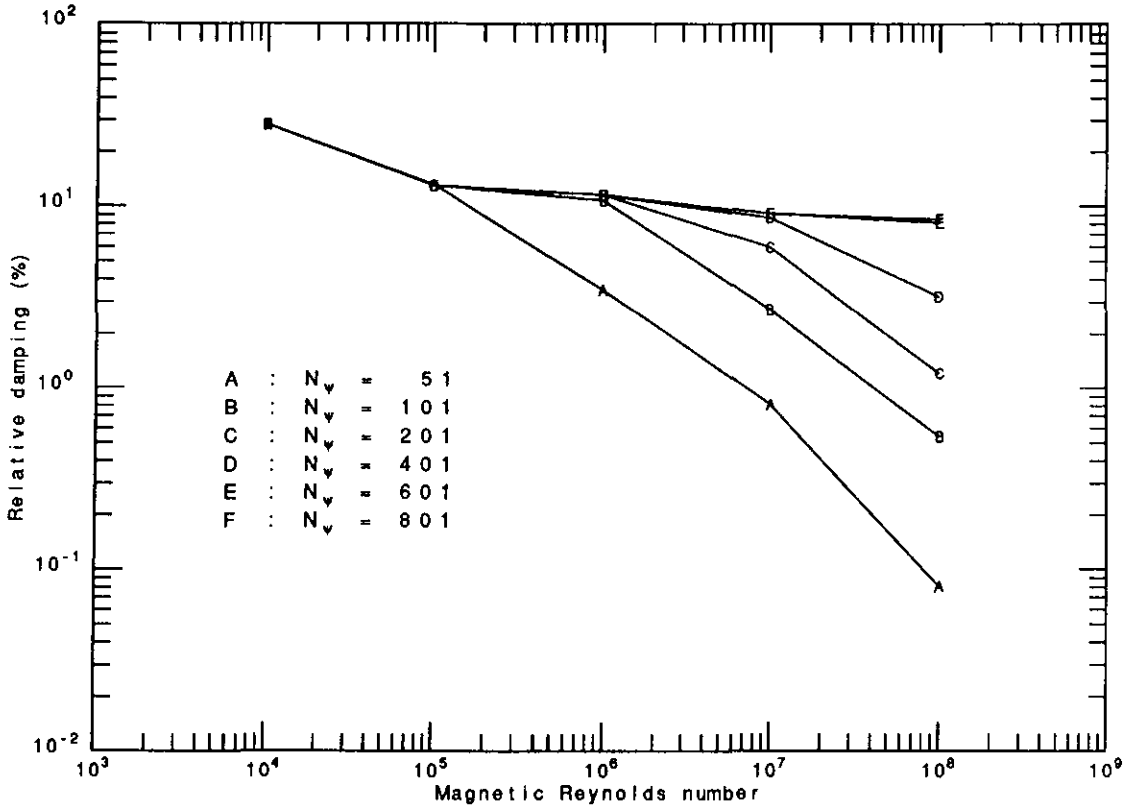


**Fig. 7.11** *Relative damping versus plasma resistivity for the mode indicated in Fig. 7.10 and for different values of $N_\psi$ again showing the need for a sufficiently high resolution in the resistive layer in order to get the damping correct.*

uum branch at $s = 0.92$, and with the two $m = 5$ continuum branches at $s = 0.96$ and at $s = 0.97$. The corresponding ideal eigenfunction exhibits a global structure with predominantly $m = 2$, 3, and 4 harmonics and with 4 singular layers at $s = 0.47$ ($m = 2$ branch), at $s = 0.92$ ($m = 4$ branch), and at at $s = 0.96$ and $s = 0.97$ ($m = 5$ branches). Again the singularity of the ideal case $\eta \equiv 0$ is coupled to several Fourier components. The convergence study for asymptotically small resistivity, shown in Fig. 7.11, reveals that the damping remains constant for $\eta$ smaller than $10^{-6}$. Now, four basic singularities at four distinct positions have to be resolved accurately. This requires a large number of radial grid points for resolving these four resistive layers in the limit of vanishing resistivity, e.g. up to $N_\psi \geq 801$ for $\eta = 10^{-8}$. Apart from this increased computational effort, the results emerge very clearly. For asymptotically small dissipation the damping becomes independent of dissipation and remains finite, i.e. $\lim_{\eta \longrightarrow 0} \delta = 9.5\%$. In this case, where resonant absorption takes place at four distinct locations, the damping is indeed large.

## 7.4 Conclusions

We have studied the Alfvén spectrum of axisymmetric tokamak plasmas. In contrast to the determination of the continuous part of the ideal MHD spectrum of plasmas with cylinder symmetry, the determination of the ideal continuum of toroidal plasmas is not trivial. The toroidal curvature induces a poloidal mode coupling which is the strongest on rational surfaces where the cylindrical continuum frequencies are at least four-fold degenerate. The effect of the mode coupling is to remove these degeneracies which gives rise to 'avoided crossings' and, by consequence, 'gaps' in the continuous spectrum of finite aspect ratio tokamaks. The size of these gaps is proportional to the strength of the poloidal mode coupling and the appearance of the gaps stresses the importance of two-dimensional effects, e.g. for Alfvén wave heating, since complete frequency bands that yield resonant absorption in one-dimensional (cylindrical) models are not eligible for this heating mechanism in the more realistic two-dimensional equilibrium models. When the poloidal mode coupling is strong enough, global Alfvén modes are found with a frequency in the above mentioned gaps. These 'gap modes' might play an important role in controlled thermonuclear fusion as they can be destabilized by interaction with (fusion born) $\alpha$-particles. These $\alpha$-particles — whose confinement is essential for ignition and hence for the possibility of generating controlled fusion energy — are lost by particle-wave resonances. However, the interaction of these gap modes with ideal continuum modes causes phase-mixing so that these modes are damped by the same resonant absorption mechanism that enables Alfvén wave heating. The important question now is which of the two phenomena — destabilization by interaction with $\alpha$-particles or damping by interaction with continuum modes — is dominant. In the present paper, we were able to quantify the damping of the gap modes due to resonant absorption. The internal structure of the ideal Alfvén continuum is very complex in tokamak plasmas and the gaps that occur at the rational surfaces are 'covered' by one or several continuum branches overlaying the gaps. As a consequence, the gap modes interact with the continuum modes with the same frequency and are damped by phase-mixing. Hence, the gap modes become quasi-modes in ideal MHD. Upon studying these modes in resistive MHD numerically by utilising the code CASTOR, we were able to show that, for asymptotically small resistivity, the damping of the global gap modes is finite and independent of $\eta$. We presented cases where the ratio of the real (damping) and imaginary (oscillatory) part of the frequency of the gap modes is of the order of 10% in the ideal-MHD limit.

The existence of TAE modes and their destabilization by neutral beam injection has been demonstrated in TFTR [Wong91] and in DIII-D [Heidbrink91]. In both experiments the pressure due to the energetic particles, $\beta_{hot}$, had to exceed the analytic threshold by one order of magnitude in order to produce the predicted instabilities. This clearly indicates that the plasma exhibits a certain damping, most probably in the form of resonant absorption as considered here. A damping in the order of $\delta \approx 0.5-1\%$ can easily explain the observed increased threshold for $\beta_{hot}$. Further detailed studies have to be performed to show whether the damping can yield indeed re-absorption of the energy near the plasma center and whether the high damping rates with $\delta \approx 5-10\%$ can be realised by appropriately modifying the density profiles. In this context, experiments with pellet injection are of great interest.

# 8. GENERAL CONCLUSIONS

An important subject in the tokamak research program is the study of the equilibrium and stability with respect to large scale motions of the plasma. The MagnetoHydroDynamic (MHD) theory, which models the plasma as a fluid in a magnetic field, provides a good description of these motions. The relative simplicity of the MHD equations allows for the (numerical) calculation of the stability of the plasma in the complicated geometry of a tokamak.

The subject of this report is the numerical study of ideal and resistive MHD instabilities in tokamaks. Most studies of resistive instabilities in a general toroidal geometry have been limited to modes which do not perturb the plasma boundary so that a number of interesting experimental and theoretical problems have not been studied. The main theme of this report is the stability of free boundary resistive modes in a fully toroidal geometry.

The CASTOR code (chapter 2) is used to solve the linearized resistive MHD equations for general axisymmetric equilibria. The eight variables are discretized using quadratic and cubic finite elements in the radial direction and a Fourier representation in the poloidal angle. The Galerkin method used results in a non-Hermitian eigenvalue problem with large sparse matrices. Inverse vector iteration is used for the calculation of single eigenvalues, whereas the QR algorithm can be used to calculate the complete spectrum of complex eigenvalues.

For the calculation of the growth rates of instabilities, it is essential to start from an accurate solution of the equilibrium equations. For this purpose, we have written a new equilibrium code called HELENA (chapter 3). The poloidal plane bounded by the plasma boundary curve is discretized by an isoparametric mapping using bicubic finite elements. By representing the poloidal flux in terms of the same two dimensional finite elements, very accurate solutions are obtained. With this representation the magnetic field is continuous. By adjusting the nodes of the isoparametric mapping the final solution is obtained in flux coordinates.

To enable the calculation of modes which perturb the plasma boundary with the CASTOR code, the plasma-vacuum boundary conditions and the numerical solution of the vacuum magnetic field equations have been implemented in the CASTOR code (chapter 4). The boundary conditions are implemented as natural boundary conditions, with the property that the ideal boundary conditions are

retrieved from the resistive ones by putting the resistivity to zero. The vacuum equations are solved independently from the eigenvalue problem of the plasma. The Laplace equation for the scalar potential of the magnetic field perturbation in the vacuum is solved using a cubic finite element/Fourier representation.

In the chapters 5 and 6, results are presented on the numerical study of the stability of resistive free boundary modes. The stability of these mode has not yet been investigated in a fully toroidal geometry, without any ordering in pressure, aspect ratio, or resistivity. In chapter 5, the influence of the pressure is investigated and a comparison is made with the stability of fixed boundary resistive modes. It is shown that the stabilizing effect of the pressure due to the plasma compression of the fixed boundary modes is lost for the free boundary modes localized near the boundary. Since the stabilization due to the favorable average curvature in combination with a pressure gradient is small, the influence of the pressure on the stability is much less important for the free boundary modes than for the fixed boundary modes.

In the second part of chapter 5, we have studied the effect of an X-point plasma shape as compared to a circular plasma boundary. The stabilizing effect of the X-point, known for ideal free boundary modes, was found even stronger for the resistive modes if the rational $q$ surface lies outside the plasma. The stabilizing effect of the X-point is less efficient if the rational surface lies inside the plasma.

In recent years, diagnostics have become available for the measurement of the equilibrium profiles of, for example, the pressure and the safety factor. This allows for the reconstruction of the plasma equilibrium with a reasonable degree of accuracy. This in turn allows for the calculation of the MHD stability properties of the plasma and a comparison between the calculated and the observed MHD instabilities.

The edge localized modes as observed during the H-mode are one example of an observed instability where the free boundary resistive mode can be important. In chapter 6, we have analyzed the stability of the $n = 1$ resistive free boundary mode of a reconstructed equilibrium of an H-mode discharge in the JET tokamak. It is shown that for the resistive free boundary mode to become significantly unstable, the current density gradient at the edge must be a factor of two larger as compared to the reconstructed equilibrium. Local details of the resistivity and of the current density profile are extremely important for the stability of these modes. The influence of the edge pressure gradient on the stability of the $n = 1$ free boundary resistive mode is small, but it may drive bootstrap currents at the

plasma edge causing a local increase of the current density gradient. Knowledge on the current distribution has become available at JET, however, not in sufficient detail at present to prove or disprove the presence of local current gradients large enough to drive external resistive modes. Consequently, rather than confirming experimental results, the calculations presented are necessarily of a predictive nature, deriving conditions under which external resistive modes can be expected in tokamaks.

In chapter 7, the MHD spectrum of circular cross-section tokamak plamas with small aspect ratio is studied for low mode numbers. Particular attention is given to the continuous part of the ideal MHD spectrum of such plasmas. Poloidal mode coupling in finite aspect ratio tokamaks yields gaps in the Alfvén continuum. Global Alfvén modes are found with a frequency inside these gaps. By interaction with the continuum branches the global Alfvén modes experience damping via phase-mixing. This damping is computed in resistive MHD. It is shown that for asymptotically small resistivity the damping is finite and independent of $\eta$.

## References


Blum J., Gilbert J.C., Le Foll J. and Thooris B., (1986), 8th Europhys. Conf. on Comp. Phys. Computing in Plasma Physics, Eibsee, Vol 10D, p. 49.

Bishop C.M., Nucl. Fusion, **26**, p. 1063, (1986).

Burrel, K.H., et al., Plasma Phys. Contr. Fusion **31** (1989) 1649.

Cheng C.Z., Phys. Fluids B, **2**, 1427 (1990).

Cheng C.Z., *Kinetic Extensions of Magnetohydrodynamic Modes for axisymmetric Toroidal Plasmas*, PPPL Report, (1990).

Coppi B., *On the Stability of Hydromagnetic Systems with Dissipation*, Propagation and Instabilities in Plasmas, ed. W.I. Futterman, (Stanford U.P., Stanford 1963).

Doyle E.J., Burrel K.H., Lehecka T., Luhmann N.C., Matsumoto H., Osborne T., Peebles W.A., Philipona R., and Rettig C., *ELM Precursors on DIII-D*, Proc. $18^{th}$ Conf. on Contr. Fusion and Plasma Physics, Berlin 1991 , Vol. I, p. 285.

Frind E.O., *An isoparametric Hermitian Element for the Solution of Field Problems*, Int. Num. Meth. Eng., **11**, 945-962 (1977).

Giannella R., Behringer B., Denne B., Gottardi N., Hawkes N.C., von Hellermann M., Lawson K., Morgan P.D., Pasini D., Stamp M.F., *Behavior of Impurities during the H-mode in JET*, Proc. $16^{th}$ Conf. on Contr. Fusion and Plasma Physics, Venice 1989, Vol. I, p. 209.

Glasser A.H., Greene J.M., and Johnson J.L., *Resistive Instabilities in General Toroidal Plasma Configurations*, Phys. Fluids, **18**, p. 875, (1975).

Glasser A.H., Greene J.M., and Johnson J.L., *Resistive Instabilities in a Tokamak*, Phys. Fluids, **19**, p. 567, (1976).

Goedbloed J.P., and Sakanaka P., Phys. Fluids, **17**, p.908, (1974).

Goedbloed, J.P., Phys. Fluids **18**, 1258 (1975).

Goedbloed J.P., Comp. Phys. Commun., (1981), **24**, p.311.

Goedbloed J.P., Hogewey G.M.D., and Hewett D.W., *Plasma Physics Plotting Library Fortran 77 Revision*, Rijnhuizen Report 86-166 (1986).

Gohil P., Ali Mahdavi M., Lao L., Burrel K.H., Chu M.S., DeBoo J.C., Hsieh C.L., Ohyabu N., Snider R.T. Stambaugh R.D., and Stockdale R.E., *Study of*

*Giant Edge-Localized Modes in DIII-D and Comparison with Ballooning Theory*, Phys. Rev. Lett. **61**, 1603 (1988).

Grimm R.C., Greene J.M., and Johnson J.L., *Methods in Computational Physics*, ed. J. Killeen, Academic Press, New York, (1976), Vol.16, p. 253.

Gruber R., Rappaz J., *Finite elements methods in linear ideal magnetohydrodynamics*, Springer-Verlag, Berlin, 1985.

Jacoby A., *MHD relaxationsinstabilitäten in Tokamak Plasmen*, Thesis Max-Planck-Institut für Plasmaphysik, 1988.

Hageman L.A., and Young D.M., *Applied Iterative Methods*, Acad. Press, London (1981).

Harley T.R., *The Computation of resistive instabilities in axisymmetric toroidal plasmas*, dissertation Princeton University, 1990.

Hastie R.J., Sykes A., Turner M., and Wesson J.A., *Stabilization of Tearing Modes in Tokamaks*, Nucl. Fusion, **17**, p.515, (1977).

Heidbrink W.W., Strait E.J., Doyle E., Sager G., and Snider R., *An Investigation of Beam-driven Alvén Instabilities in the DIII-D Tokamak*, submitted to Nucl. Fusion.

Hender T.C., Hastie R.J., Robinson D.C., *Finite Beta Effects on Tearing Modes in the Tokamak*, Nucl. Fusion, **27**, p.1389, (1987).

Huysmans G.T.A., Galvao R.M.O., Goedbloed J.P., Lazzaro E., and Smeulders P., Plasma Physics and Contr. Fusion, **31**, 2101 (1989).

Huysmans G.T.A., Galvao R.M.O., and Goedbloed J.P., *High beta stability studies of JET discharges with the numerical program HBT*, Rijnhuizen Report 90-193, 1990a.

Huysmans G.T.A., Galvao R.M.O., and Goedbloed J.P., *Documentation of the high beta stability codes HBT and HBTAS at JET*, Rijnhuizen Report 90-194, 1990b.

Huysmans G.T.A., Goedbloed J.P., and Kerner W. , *Isoparametric Bicubic Hermite Elements for Solution of the Grad-Shafranov Equation*, Proc. CP90 Conf. on Comp Phys.Proc., World Scientific Publ. Co., 1991a., p 371.

Huysmans G.T.A., Hender T.C., Kwon O.J., Goedbloed J.P., Lazzaro E., and Smeulders P., Plasma Physics and Contr. Fusion, 1991b, to appear.

Kaye S.M., Manickam J., Asakura N., Bell R.E., Lau Y., LeBlanc B., Kessel C.E., Kugel H.W., Paul S.F., Sesnic S., Takahashi H., *Characteristics of High Frequency ELM Precursors and Edge Stability in the PBX-M Tokamak*, Nucl. Fusion **30** (1990) 2621.

Kerner W. and Jandl O., *Axisymmetric MHD Equilibria with Flow*, Comp. Phys. Comm., **31**, (1984), p. 269-285.

Kerner W., Lerbinger K., Gruber R., and Tsunematsu T., *Normal mode analysis for linear resistive magnetohydrodynamics*, Comp. phys. Comm. **36** (1985), 225.

Kerner W., and Jacoby A., in *The H-mode of ASDEX*, Sec 7.2, ASDEX team, Nucl. Fusion, **29**, (1989), p. 1959.

Kerner W., *Large-scale complex eigenvalue problems*, J. Comp. Phys., Vol.85, no. 1, 1989.

Kerner W., Poedts S., Goedbloed J.P., Huysmans G.T.A., Keegan B. and Schwarz E., *Computing the damping and destabilization of global Alvén waves in tokamaks*, Proc. 18th Eur. Conf. on Contr. Fusion and Plasma Phys., Berlin (1991), part IV, p.89-93.

Laval G., Pellat R., and Soule J.L., Phys. Fluids, **17**, p.835, (1974).

Lütjens H., Bondeson A., and Roy A. , *Axisymmetric MHD Equilibrium Solver with Bicubic Hermite Elements*, 1990, CRPP Lausanne report, LRP405/90.

Mercier C., Nucl. Fusion **1**, p.47, (1960).

Ozeki T., Azumi M., Ninomiya H., Tokuda S., Tsunematsu T., and Seke S., *Divertor Effects on the Stability of Axisymmetric Modes and Kink Modes in Tokamaks*, Nucl. Fusion **28**, p. 1859 (1988).

Ozeki T., Chu M.S., Lao L.L. Taylor T.S., Chance M.S., Kinoshita S., Burrel K.H., Stambaugh R.D., *Plasma Shaping, Edge Ballooning Stability and ELM Behavior in DIII-D*, Nucl. Fusion **30** (1990) 1425.

Pao, Y.-P. : Nuclear Fusion **15**, 631 (1975).

Poedts S., Kerner W., and Goossens M., 1989, J. Plasma Physics **42**, p. 27-58.

Poedts S. and Kerner W., 1991, Phys. Rev. Letters **66**, p. 2871-2874.

Porcelli F., 1991, Plasma Phys. and Contr. Fusion **33**, pp. 1601.

Roy A., *Stabilité MHD d'un Tokamak Quasi Circulaire, Optimisation des Profils de Courant et de Pression et Influence d'un Point de Rebroussement a la Surface du Plasma*, 1990, Laussanne Report LRP 415/90.

Strang G., and Fix G.J., *An analysis of the finite element method*, 1973, Prentice Hall, Englewood, N.J..

Schwarz H.R., *Finite element methods*, Academic press, London, 1988.

Soloviev L.S., in : Reviews of plasma Physics, vol. 6, ed. M.A. Leontovich (Consultants Bureau, New York), 1975, p.257.

Vollmer O., Aratari R., Ryter F., Steuer K., and Wagner F., *Long Pulse Heating in Asdex L- and H-mode Discharges*, Proc. $17^{th}$ Conf. on Contr. Fusion and Plasma Physics, Amsterdam 1989 , Vol. I, p. 295.

Wagner F. et al., *Regime of Improved Confinement and High Beta in Neutral-Beam-Heated Divertor Discharges of the ASDEX Tokamak*, Phys. Rev. Lett. **49**, 1408 (1982).

Wong K.L., 1991, Phys. Rev. Letters, **66**, pp. 1874.

Zienkiewicz O.C., *The Finite Element Method in Engineering Science*, McGraw-Hill, London 1971.

Zohm H., Wagner F., Endler M., Gernhardt J., Holzhauer E., Kerner W., and Mertens V., *ELM Studies on ASDEX*, submitted to Nuclear Fusion.

# APPENDICES

## Appendix A : Technical details on the CASTOR code

### A.1 Structure of CASTOR

Whereas the physics background of CASTOR has been extensively described in the main text, it is usely helpful for users to get some introduction in the organization of the code as a whole. Since CASTOR has gone through a long series of a gradual transformations over the past two years, and is still in the process of rapid change, the best we can do here is to point to the code itself and, in particular, to its internal documentation. On the next three pages we show a part of the listing of CASTOR8 (dating from July 4, 1991) which has been made by means of the REVISE program NEW (described in Appendix D1). The listing shows both line numers (to the left) and REVISE identification numbers (to the right), whereas an index to all the COMMON blocks and subroutines is appended at the end (not shown here).

Throughout the code the subroutines are equiped with a comment box describing the function of that particular subroutine. Here, we have only printed the comment box of the main program since it provides the necessary information on the NAMELIST input parameters (CASTOR.19-102), a short description of the modular structure of the code (CASTOR.122-135), needed external library routines (CASTOR.137-145), and memory requirements associated with the number of radial grid points and poloidal harmonics chosen (CASTOR.150-184).

The SOURCE of the code is in a precompile format, with the COMMON blocks appearing at the beginning (starting with the line COMVER.1, and suppressed for most of the rest in the listing shown), which requires the precompiler PRE of REVISE to produce a FORTRAN file that can be compiled.

The code consists of four parts (modules) which separate the different main functions, viz. specification of the equilibrium (module EQUIL), computing the matrices A and B (module MAT), solving the eigenvalue problem (modules SOLV), and diagnosing the solution by printing and plotting (module DIAG). One of the

merits of the vacuum solution of the perturbations is that it may be completely separated from the rest of the computation, resulting in an additional module VACUUM. The usual routine of computing eigenvalues or spectra is to execute the code with a succession of calls to the different eigenvalue solvers: QR (SOLV1) to get a rough idea of the overall structure of the spectrum, inverse vector iteration with the matrices kept in core (SOLV2), out of core (SOLV3), or efficiently stored in core (SOLV4) to accurately hunt out single eigenvalues, and using the Lanczos algorithm (SOLV5) to compute parts of the spectrum in one run.

```
----- SOURCE LISTING (*COMDECKS) ----  5/ 7/91 - 13. 3.44 ----- CASTOR8, P.  1 -------------

                                    ==========
                                    = *COMDECKS =
                                    ==========

   1 *COMDECK COMVER                                                          COMVER  .   1
   2       CHARACTER  VERSION*(*),   DD*(*)                                   COMVER  .   2
   3       PARAMETER (VERSION = '8', DD = '4 JULY 1991')                      COMVER  .   3
   4 *COMDECK COMMAX                                                          COMMAX  .   1
   5       PARAMETER (LANZ=5, MANZ=5, MDIF=1, LMAX=20)                        COMMAX  .   2
   6       PARAMETER (NGMAX=251, MXNINT=NGMAX-1)                              COMMAX  .   3
   7       PARAMETER (NDEQ=4*MXNINT)                                          COMMAX  .   4

     ..........................................................................
     ..........................  etc. etc.  ...................................
     ..........................................................................

----- SOURCE LISTING (*DECKS) -------  5/ 7/91 - 13. 3.44 ----- CASTOR8, P.  9 -------------

                                    ==========
                                    = *DECKS =
                                    ==========

 403 *DECK CASTOR                                                           CASTOR  .   1
 404       PROGRAM CASTOR                                                   CASTOR  .   2
 405 C                                                                      CASTOR  .   3
 406 ************************************************************************** CASTOR  .   4
 407 ************************************************************************** CASTOR  .   5
 408 **                                                                   ** CASTOR  .   6
 409 **  M A S T E R F I L E  :  CASTOR                                   ** CASTOR  .   7
 410 **  ----------------------------                                    ** CASTOR  .   8
 411 **                                                                   ** CASTOR  .   9
 412 **  COMPLEX ALFVEN SPECTRUM FOR TOROIDAL PLASMAS                     ** CASTOR  .  10
 413 **  -       -      -            ---                                 ** CASTOR  .  11
 414 **                                                                   ** CASTOR  .  12
 415 **  VERSION :                                                        ** CASTOR  .  13
 416 *CALL COMVER                                                           CASTOR  .  14
 417 **                                                                   ** CASTOR  .  15
 418 ************************************************************************** CASTOR  .  16
 419 ************************************************************************** CASTOR  .  17
 420 **                                                                   ** CASTOR  .  18
 421 **  INPUT :                                                          ** CASTOR  .  19
 422 **  -----                                                            ** CASTOR  .  20
 423 **                                                                   ** CASTOR  .  21
 424 **  EQUILIBRIUM : READ FROM DISK (UNIT NMAP)                         ** CASTOR  .  22
 425 **                                                                   ** CASTOR  .  23
 426 **  NAMELIST NEWRUN :                                                ** CASTOR  .  24
 427 **                                                                   ** CASTOR  .  25
 428 **    MODE      - CONTROL PARAMETER;                                 ** CASTOR  .  26
 429 **                VALUES:                                            ** CASTOR  .  27
 430 **                 0 - TERMINATION OF EXECUTION                      ** CASTOR  .  28
 431 **                 1 - QR ALGORITHM                                  ** CASTOR  .  29
 432 **                 2 - VECTOR ITERATION, IN-CORE (STEUERWALD)        ** CASTOR  .  30
 433 **                 3 - VECTOR ITERATION, OUT-OF-CORE (SCHWARZ)       ** CASTOR  .  31
 434 **                 4 - VECTOR ITERATION, IC VERSION OF OOC SOLVER    ** CASTOR  .  32
 435 **                 5 - LANCZOS ALGORITHM                             ** CASTOR  .  33
 436 **                11 - TESTCASE SOLOVEV (ASPECT=3,ELLIPT=2), SOLVER 1 ** CASTOR  .  34
 437 **                12 - TESTCASE SOLOVEV (ASPECT=3,ELLIPT=2), SOLVER 2 ** CASTOR  .  35
 438 **                13 - TESTCASE SOLOVEV (ASPECT=3,ELLIPT=2), SOLVER 3 ** CASTOR  .  36
 439 **                14 - TESTCASE SOLOVEV (ASPECT=3,ELLIPT=2), SOLVER 4 ** CASTOR  .  37
 440 **                                                                   ** CASTOR  .  38
 441 **    EQNAME    - NAME OF THE EQUILIBRIUM                            ** CASTOR  .  39
 442 **    NLTORE    - TOROIDAL EQUILIBRIUM (.T. OR .F.)                  ** CASTOR  .  40
 443 **    NG        - NUMBER OF GRID POINTS                              ** CASTOR  .  41
 444 **    RFOUR(1)  - LOWEST POLOIDAL MODE NUMBER                        ** CASTOR  .  42
 445 **    NTOR      - TOROIDAL MODE NUMBER                               ** CASTOR  .  43
 446 **    ETA       - RESISTIVITY                                        ** CASTOR  .  44
 447 **    ASPECT    - ASPECT RATIO (ONLY IF NLTORE=.F.)                  ** CASTOR  .  45
 448 **    Q0ZYL     - Q ON AXIS                                          ** CASTOR  .  46
 449 **    SIG1      - SIGMA OF FIRST MESHACC. POINT                      ** CASTOR  .  47
 450 **    SIG2      - SIGMA OF SECOND MESHACC. POINT                     ** CASTOR  .  48
```

```
 451 **    XR1       - POSITION OF FIRST MESHACC. POINT                          ** CASTOR  .  49
 452 **    XR2       - POSITION OF SECOND MESHACC. POINT                         ** CASTOR  .  50
 453 **    RWALL     - POSITION OF THE WALL                                      ** CASTOR  .  51
 454 **    NVPSI     - NUMBER OF RADIAL POINTS IN VACUUM METRIC                  ** CASTOR  .  52
 455 **    NGV       - NUMBER OF RADIAL POINTS IN VAC. POTENTIAL SOL.            ** CASTOR  .  53
 456 **    SIGV      - SIGMA OF MESHACC. IN VACUUM (XR = 0.)                     ** CASTOR  .  54
 457 **    DSURF     - PARAMETER FOR DENSITY PROFILE :                           ** CASTOR  .  55
 458 **    IDPOW     - PARAMETER FOR DENSITY PROFILE :                           ** CASTOR  .  56
 459 **                RHO = ( 1 - (1 - DSURF) * S**2 )**IDPOW                   ** CASTOR  .  57
 460 **    NDIAGFK   - PRINT SWITCH FOR FOURIER COMPONENTS OF THE METRIC         ** CASTOR  .  58
 461 **                                                                          ** CASTOR  .  59
 462 **    VSHIFT(I)- I-TH ESTIMATE OF EIGENVALUE FOR VECTOR ITERATION           ** CASTOR  .  60
 463 **                (I.LE.100); IF AUTOMATIC :                                ** CASTOR  .  61
 464 **    NRS       - NUMBER OF AUTOMATIC REAL      SHIFTS                      ** CASTOR  .  62
 465 **    NIS       - NUMBER OF AUTOMATIC IMAGINARY SHIFTS                      ** CASTOR  .  63
 466 **    DRS       - WIDTH  OF AUTOMATIC REAL      SHIFTS                      ** CASTOR  .  64
 467 **    DIS       - WIDTH  OF AUTOMATIC IMAGINARY SHIFTS                      ** CASTOR  .  65
 468 **                                                                          ** CASTOR  .  66
 469 **    EPS       - RELATIVE ACCURACY OF EIGENVALUE (VECTOR ITERATION)        ** CASTOR  .  67
 470 **    NPLOT     - PLOT SWITCH FOR SOLVERS 1 - 4,                            ** CASTOR  .  68
 471 **                NUMBER OF PLOTS FOR QR-SOLVER                             ** CASTOR  .  69
 472 **    XMINQR(I)- LOWER LIMIT X-AXIS FOR I-TH QR-PLOT                        ** CASTOR  .  70
 473 **    XMAXQR(I)- UPPER LIMIT X-AXIS FOR I-TH QR-PLOT                        ** CASTOR  .  71
 474 **    YMINQR(I)- LOWER LIMIT Y-AXIS FOR I-TH QR-PLOT                        ** CASTOR  .  72
 475 **    YMAXQR(I)- UPPER LIMIT Y-AXIS FOR I-TH QR-PLOT                        ** CASTOR  .  73
 476 **                                                                          ** CASTOR  .  74
 477 **  NAMELIST NEWLAN :                                                       ** CASTOR  .  75
 478 **                                                                          ** CASTOR  .  76
 479 **    ISTART  - IF 0 : START WITH SHIFT (EWSHIFT) AND COMPUTATION           ** CASTOR  .  77
 480 **                     OF THE T-MATRIX                                      ** CASTOR  .  78
 481 **              ELSE  : READ T-MATRIX FROM DISK                             ** CASTOR  .  79
 482 **    ISTOP   - IF < 0 : WRITE T-MATRIX ON DISK + COMPUTATION               ** CASTOR  .  80
 483 **              ELSE   : WRITE T-MATRIX ON DISK AND STOP                    ** CASTOR  .  81
 484 **    KMAX    - DIMENSION OF THE T-MATRIX                                   ** CASTOR  .  82
 485 **    MXLOOP  - MAXIMUM NUMBER OF SHIFTS                                    ** CASTOR  .  83
 486 **    ISHIFT  - IF 1 : MAKE SHIFTS FOR EWSHIFT AND OWS(1:NUS)               ** CASTOR  .  84
 487 **              ELSE : MAKE SHIFTS FOR EWSHIFT AND REGION DETERINED         ** CASTOR  .  85
 488 **                     BY XLIML,XLIMR,YLIMB,YLIMT                           ** CASTOR  .  86
 489 **    FOR ISHIFT.EQ.1 :                                                     ** CASTOR  .  87
 490 **    NUS     - NUMBER OF GIVEN SHIFTS IN ADDITION TO EWSHIFT               ** CASTOR  .  88
 491 **    OWS     - VECTOR FOR EIGENVALUE SHIFTS                                ** CASTOR  .  89
 492 **    FOR ISHIFT.NE.1 :                                                     ** CASTOR  .  90
 493 **    XLIML   - MINIMUM REAL PART OF INVESTIGATED REGION                    ** CASTOR  .  91
 494 **    XLIMR   - MAXIMUM REAL PART OF INVESTIGATED REGION                    ** CASTOR  .  92
 495 **    YLIMB   - MINIMUM IMAGINARY PART OF INVESTIGATED REGION               ** CASTOR  .  93
 496 **    YLIMT   - MAXIMUM IMAGINARY PART OF INVESTIGATED REGION               ** CASTOR  .  94
 497 **    IHOLE   - .TRUE. : THERE IS A REGION XHOLEL,XHOLER,YHOLEB,            ** CASTOR  .  95
 498 **                       YHOLET, PART OF THE REGION XLIML,XLIMR,            ** CASTOR  .  96
 499 **                       YLIMB,YLIMT, WITHIN WHICH NO EIGENVALUES           ** CASTOR  .  97
 500 **                       ARE TO BE SEARCHED FOR                             ** CASTOR  .  98
 501 **    XHOLEL  - MINIMUM REAL PART                                           ** CASTOR  .  99
 502 **    XHOLER  - MAXIMUM REAL PART                                           ** CASTOR  . 100
 503 **    YHOLEB  - MINIMUM IMAGINARY PART                                      ** CASTOR  . 101
 504 **    YHOLET  - MAXIMUM IMAGINARY PART                                      ** CASTOR  . 102
 505 **                                                                          ** CASTOR  . 103
 506 **  OUTPUT :                                                                ** CASTOR  . 104
 507 **  ------                                                                  ** CASTOR  . 105
 508 **                                                                          ** CASTOR  . 106
 509 **    WRITTEN ON UNIT  6                                                    ** CASTOR  . 107
 510 **            ON UNIT  8 (AT IPP)                                           ** CASTOR  . 108
 511 **            ON UNIT 11 (TEXT FOR FIRST PLOT)                              ** CASTOR  . 109
 512 **            AND FOR SOLVER 3 :                                            ** CASTOR  . 110
 513 **            ON UNIT ND1 (DEFINED IN PRESET = 13)                          ** CASTOR  . 111
 514 **            ON UNIT ND2 (DEFINED IN PRESET = 14)                          ** CASTOR  . 112
 515 **            ON UNIT ND3 (DEFINED IN PRESET = 15)                          ** CASTOR  . 113
 516 **            ON UNIT ND4 (DEFINED IN PRESET = 16)                          ** CASTOR  . 114
 517 **            ON UNIT ND5 (DEFINED IN PRESET = 17)                          ** CASTOR  . 115
 518 **            ON UNIT ND6 (DEFINED IN PRESET = 18)                          ** CASTOR  . 116
 519 **            ON UNIT ND7 (DEFINED IN PRESET = 19)                          ** CASTOR  . 117
 520 **                                                                          ** CASTOR  . 118
 521 ************************************************************************** CASTOR  . 119
 522 ************************************************************************** CASTOR  . 120
 523 **                                                                          ** CASTOR  . 121
```

```
524 **  MODULAR STRUCTURE :                                                  ** CASTOR  . 122
525 **  -----------------                                                   ** CASTOR  . 123
526 **    CASTOR - PRESET                                                   ** CASTOR  . 124
527 **             TESTS                                                    ** CASTOR  . 125
528 **             EQUIL                                                    ** CASTOR  . 126
529 **                (MODULE SPECIFYING THE EQUILIBRIUM)                   ** CASTOR  . 127
530 **             VACUUM                                                   ** CASTOR  . 128
531 **                (MODULE COMPUTING VACUUM PERTURBATION)                ** CASTOR  . 129
532 **             MAT1-5                                                   ** CASTOR  . 130
533 **                (MODULE COMPUTING THE MATRICES A AND B)               ** CASTOR  . 131
534 **             SOLV1-5                                                  ** CASTOR  . 132
535 **                (MODULES FOR THE DIFFERENT EIGENVALUE SOLVERS)        ** CASTOR  . 133
536 **             DIAG1-5                                                  ** CASTOR  . 134
537 **                (MODULE FOR THE DIAGNOSTICS)                          ** CASTOR  . 135
538 **                                                                      ** CASTOR  . 136
539 **  EXTERNAL SUBROUTINES :                                              ** CASTOR  . 137
540 **  --------------------                                                ** CASTOR  . 138
541 **    PPPLIB  : BEGPLT, LBLTOP, LPLOT, DLCH, NFRAME, FINPLT             ** CASTOR  . 139
542 **    BLAS    : C(Z)COPY, C(Z)DOTC, C(Z)SCAL, C(Z)AXPY, IC(Z)AMAX       ** CASTOR  . 140
543 **              C(Z)DOTU, S(D)SCAL, S(D)COPY, C(Z)S(D)SCAL              ** CASTOR  . 141
544 **    LINPACK : CPOCO, CPOSL, S(D)GTSL                                  ** CASTOR  . 142
545 **    EISPACK : CBAL, CORTH, COMQR                                      ** CASTOR  . 143
546 **    CRAY    : RANSET, RCFFT2, ORDERS                                  ** CASTOR  . 144
547 **    HGOLIB  : RFT2 (NOT AT IPP)                                       ** CASTOR  . 145
548 **                                                                      ** CASTOR  . 146
549 ************************************************************************ CASTOR  . 147
550 ************************************************************************ CASTOR  . 148
551 **                                                                      ** CASTOR  . 149
552 **  MAXIMUM NUMBER OF GRID POINTS AND FOURIER COEFFICIENTS :            ** CASTOR  . 150
553 **  ======================================================              ** CASTOR  . 151
554 **                                                                      ** CASTOR  . 152
555 **                                MEMORY (64-BIT WORDS)                 ** CASTOR  . 153
556 **                                                                      ** CASTOR  . 154
557 **                        1 800 000       3 600 000        64 000 000   ** CASTOR  . 155
558 **  ------------------------------------------------------------------- ** CASTOR  . 156
559 **  1) QR                 NG=12, MANZ=3   NG=18, MANZ=3   NG=83,  MANZ= 3  ** CASTOR  . 157
560 **     ==                 NG=7,  MANZ=5   NG=11, MANZ=5   NG=49,  MANZ= 5  ** CASTOR  . 158
561 **                                                NG=35,  MANZ= 7  ** CASTOR  . 159
562 **                                                                 ** CASTOR  . 160
563 **  2) IV (IC)            NG=49, MANZ=3   NG=113,MANZ=3   NG=2279,MANZ= 3  ** CASTOR  . 161
564 **     =======            NG=17, MANZ=5   NG=40, MANZ=5   NG=822, MANZ= 5  ** CASTOR  . 162
565 **                                        NG=20, MANZ=7   NG=420, MANZ= 7  ** CASTOR  . 163
566 **                                                        NG=254, MANZ= 9  ** CASTOR  . 164
567 **                                                        NG=169, MANZ=11  ** CASTOR  . 165
568 **                                                        NG=121, MANZ=13  ** CASTOR  . 166
569 **                                                                 ** CASTOR  . 167
570 **  3) IV (OOC)           MANZ=7          MANZ=11         MANZ=21          ** CASTOR  . 168
571 **     ========           NO LIMIT ON NG (FOR PLOTS : NG < NGMAX)          ** CASTOR  . 169
572 **                                                                 ** CASTOR  . 170
573 **  4) IV (IC-OOC)        NG=95, MANZ=3   NG=221,MANZ=3   NG=4458,MANZ= 3  ** CASTOR  . 171
574 **     ==========         NG=32, MANZ=5   NG=78, MANZ=5   NG=1622,MANZ= 5  ** CASTOR  . 172
575 **                                        NG=39, MANZ=7   NG=831, MANZ= 7  ** CASTOR  . 173
576 **                                                        NG=503, MANZ= 9  ** CASTOR  . 174
577 **                                                        NG=336, MANZ=11  ** CASTOR  . 175
578 **                                                        NG=240, MANZ=13  ** CASTOR  . 176
579 **                                                        NG=180, MANZ=15  ** CASTOR  . 177
580 **                                                                 ** CASTOR  . 178
581 **  5) LANCZOS            NG=32, MANZ=3   NG=74, MANZ=3   NG=1491,MANZ= 3  ** CASTOR  . 179
582 **     =======            NG=11, MANZ=5   NG=26, MANZ=5   NG=542, MANZ= 5  ** CASTOR  . 180
583 **                                        NG=13, MANZ=7   NG=277, MANZ= 7  ** CASTOR  . 181
584 **                                                        NG=168, MANZ= 9  ** CASTOR  . 182
585 **                                                        NG=112, MANZ=11  ** CASTOR  . 183
586 **                                                        NG=80,  MANZ=13  ** CASTOR  . 184
587 **                                                                 ** CASTOR  . 185
588 ************************************************************************ CASTOR  . 186
589 ************************************************************************ CASTOR  . 187
590 C                                                                       CASTOR  . 188
591 *CALL COMMAX                                                           CASTOR  . 189
```

.....
..... etc. etc. .....
.....

## A.2 Explicit expressions of the matrix elements

The final form of the matrix elements of the $A$ and $B$ matrices is given below. The indices are the same as in the sub block of the $ZMA$ matrix in Fig. A.1. The second index labels the variable in the state vector, $\widetilde{U} = (\bar{\rho}_1, \bar{v}_1, \bar{v}_2, \bar{v}_3, \bar{T}_1, \bar{A}_1, \bar{A}_2, \bar{A}_3)$, the first index labels the number of the equations (in the same order as the state vector). The expressions do not explicitly show the dependence on the radial interval, the Fourier harmonics and the index of the two interpolating functions (the index $p$). The equilibrium terms should be read as the $(\bar{m} - m)^{th}$ harmonic, where $\bar{m}$ and $m$ determine the position in the $(\bar{k}, k)$ sub-block. The lower and upper case $h$ stand for the two quadratic and cubic finite elements respectively.

With these shorthand notations in mind, the $B$ and $A$ matrices are given by:

$$B(1,1) = hh\frac{fqR^2}{s^2F} \tag{A.1}$$

$$\begin{aligned} B(2,2) &= HH\rho_0\frac{FR^2}{fq}\, g_{11} \\ B(2,3) &= -Hh\rho_0\frac{FR^2}{fq} i g_{12} \\ B(2,4) &= -Hh\rho_0\frac{FR^2}{fq} i g_{12} \end{aligned} \tag{A.2}$$

$$\begin{aligned} B(3,2) &= hH\rho_0\frac{FR^2}{fq} i g_{12} \\ B(3,3) &= hh\rho_0\frac{FR^2}{fq}\, g_{22} \\ B(3,4) &= hh\rho_0\frac{FR^2}{fq}\, g_{22} \end{aligned} \tag{A.3}$$

$$\begin{aligned} B(4,2) &= hH\rho_0\frac{FR^2}{fq} i g_{12} \\ B(4,3) &= hh\rho_0\frac{FR^2}{fq}\, g_{22} \\ B(4,4) &= hh\rho_0\frac{FR^2}{fq}\,(g_{22} + q^2R^2) \end{aligned} \tag{A.4}$$

$$B(5,5) = hh\frac{1}{\gamma - 1}\rho_0\frac{fqR^2}{s^2F} \tag{A.5}$$

$$\begin{aligned} B(6,6) &= hh\frac{F}{fq}\, g_{22} \\ B(6,7) &= -hH\frac{F}{fq} i g_{12} \end{aligned} \tag{A.6}$$

$$
\begin{aligned}
B(7,6) &= Hh\frac{F}{fq}ig_{12} \\
B(7,7) &= HH\frac{F}{fq}\,g_{11}
\end{aligned}
\tag{A.7}
$$

$$
B(8,8) = HH\frac{fq}{F} \tag{A.8}
$$

$$
\begin{aligned}
A(1,2) &= hH'\frac{-\rho_0 R^2}{s} - hH\,\frac{1}{s}\Big(R^2\frac{\partial\rho_0}{\partial s} + \rho_0\frac{\partial R^2}{\partial s}\Big) \\
A(1,3) &= -hh\,m\frac{\rho_0 R^2}{s} \\
A(1,4) &= -hh\,(m+nq)\frac{\rho_0 R^2}{s}
\end{aligned}
\tag{A.9}
$$

$$
\begin{aligned}
A(2,1) &= H'h\,\frac{R^2 T_0}{s} + Hh\,\frac{T_0}{s}\frac{\partial R^2}{\partial s} \\
A(2,5) &= H'h\,\frac{R^2\rho_0}{s} + Hh\,\frac{\rho_0}{s}\frac{\partial R^2}{\partial s} \\
A(2,6) &= H'h\,\frac{F^2}{fq^2R^2}(ng_{22} - \bar{m}qR^2) \\
&\quad + Hh\,\frac{nF^2}{fq^2R^2}\Big(ig_{12}(2m-\bar{m}+nq) - R^2\frac{\partial}{\partial s}\Big(\frac{g_{22}}{R^2}\Big)\Big) \\
A(2,7) &= H'H'\,\frac{F^2}{fq} + H'H\,\frac{-ing_{12}F^2}{fq^2R^2} \\
&\quad + HH\,\frac{nF^2}{fq^2R^2}\Big(g_{11}(m+nq) - ig_{12}\frac{q}{F}\frac{d}{ds}\Big(\frac{F}{q}\Big)\Big) \\
A(2,8) &= H'H'\,\frac{-g_{22}F^2}{fq^2R^2} + H'H\,\frac{i\bar{m}g_{12}F^2}{fq^2R^2} \\
&\quad + HH'\,\frac{-F^2}{fq^2R^2}\Big(ig_{12}(2m-\bar{m}+nq) - R^2\frac{\partial}{\partial s}\Big(\frac{g_{22}}{R^2}\Big)\Big) \\
&\quad + HH\,\frac{-\bar{m}F^2}{fq^2R^2}\Big(g_{11}(m+nq) - ig_{12}\frac{q}{F}\frac{d}{ds}\Big(\frac{F}{q}\Big)\Big)
\end{aligned}
\tag{A.10}
$$

$$
\begin{aligned}
A(3,1) &= hh\,\frac{R^2 T_0}{s}\bar{m} \\
A(3,5) &= hh\,\frac{R^2\rho_0}{s}\bar{m} \\
A(3,6) &= hh\,\frac{-F^2}{fqR^2}(m\bar{m}R^2 + n^2 g_{22})
\end{aligned}
\tag{A.11}
$$

$$
\begin{aligned}
A(3,7) &= hH' \frac{mF^2}{fq} \\
&\quad + hH \frac{nF^2}{fq^2R^2}\Big(ig_{12}(\bar{m}-m+nq) + \frac{qR^2}{F}\frac{\partial}{\partial s}\big(\frac{Fg_{22}}{qR^2}\big)\Big) \\
A(3,8) &= hH' \frac{F^2 n g_{22}}{fqR^2} \\
&\quad + hH \frac{-\bar{m}F^2}{fq^2R^2}\Big(ig_{12}(\bar{m}-m+nq) + \frac{qR^2}{F}\frac{\partial}{\partial s}\big(\frac{Fg_{22}}{qR^2}\big)\Big)
\end{aligned}
\tag{A.11}
$$

$$
\begin{aligned}
A(4,1) &= hh \frac{R^2 T_0}{s}(\bar{m}+nq) \\
A(4,5) &= hh \frac{R^2 \rho_0}{s}(\bar{m}+nq) \\
A(4,6) &= hh \frac{F^2}{fq}\bar{m}(\bar{m}-m) \\
A(4,7) &= hH' \frac{F^2}{fq}(m-\bar{m}) \\
&\quad + hH \frac{nF^2}{fq^2R^2}\Big(-ig_{12}(m-\bar{m}) + \frac{qR^2}{F}\frac{\partial}{\partial s}\big(\frac{Fg_{22}}{qR^2}\big) + \frac{q^2R^2}{F}\frac{dF}{ds}\Big) \\
A(4,8) &= hH \frac{-\bar{m}F^2}{fq^2R^2}\Big(-i(m-\bar{m})g_{12} + \frac{qR^2}{F}\frac{\partial}{\partial s}\big(\frac{Fg_{22}}{qR}\big) + \frac{q^2R^2}{F}\frac{dF}{ds}\Big)
\end{aligned}
\tag{A.12}
$$

$$
\begin{aligned}
A(5,2) &= hH' \frac{-R^2\rho_0 T_0}{s} + hH \frac{-\rho_0}{s}\Big(T_0\frac{\partial R^2}{\partial s} + \frac{R^2}{\gamma-1}\frac{\partial T_0}{\partial s}\Big) \\
A(5,3) &= hh \frac{-R^2\rho_0 T_0}{s} m \\
A(5,4) &= hh \frac{-R^2\rho_0 T_0}{s}(m+nq)
\end{aligned}
\tag{A.13}
$$

$$
\begin{aligned}
A(6,2) &= hH \frac{ig_{12}F^2}{fq} \\
A(6,3) &= hh \frac{g_{22}F^2}{fq} \\
A(6,6) &= hh \frac{-\eta F}{fqR^2}(g_{22}n^2 + \bar{m}^2R^2) \\
A(6,7) &= hH' \frac{\eta F}{fq}\bar{m} + hH \frac{\eta F}{fqR^2} ig_{12}n^2 \\
A(6,8) &= hH' \frac{\eta F}{fqR^2} g_{22}n + hH \frac{-\eta F}{fqR^2} i\bar{m}ng_{12}
\end{aligned}
\tag{A.14}
$$

$$
\begin{aligned}
A(7,2) &= HH\,\frac{-g_{11}F^2}{fq} \\
A(7,3) &= Hh\,\frac{ig_{12}F^2}{fq} \\
A(7,6) &= H'h\,\frac{\eta F}{fq}\,\bar{m} + Hh\,\frac{F}{fqR^2}(-i\eta n^2 g_{12} + \frac{\partial \eta}{\partial s}\bar{m}R^2) \\
A(7,7) &= H'H'\,\frac{-\eta F}{fq} + HH\,\frac{-\eta F}{fqR^2}\,n^2 g_{11} + HH'\,\frac{-F}{fq}\frac{\partial \eta}{\partial s} \\
A(7,8) &= HH'\,\frac{\eta F}{fqR^2}\,ing_{12} + HH\,\frac{\eta F}{fqR^2}\,g_{11}n\bar{m} \\
A(8,2) &= HH\,f \\
A(8,6) &= H'H\,\frac{\eta F}{fqR^2}\,ng_{22} + Hh\,\frac{nF}{fqR^2}(i\eta m g_{12} + g_{22}\frac{\partial \eta}{\partial s}) \\
A(8,7) &= H'H\,\frac{-\eta F}{fqR^2}\,ing_{12} + HH\,\frac{nF}{fqR^2}(\eta m g_{11} - ig_{12}\frac{\partial \eta}{\partial s}) \\
A(8,8) &= H'H'\,\frac{-\eta F}{fqR^2}\,g_{22} + HH'\,\frac{-F}{fqR^2}(i\eta m g_{12} + g_{22}\frac{\partial \eta}{\partial s}) \\
&\quad + H'H\,\frac{\eta F}{fqR^2}\,i\bar{m}g_{12} + HH\,\frac{-\bar{m}F}{fqR^2}(\eta m g_{11} - ig_{12}\frac{\partial \eta}{\partial s})
\end{aligned}
\qquad (A.15)\ (A.16)
$$

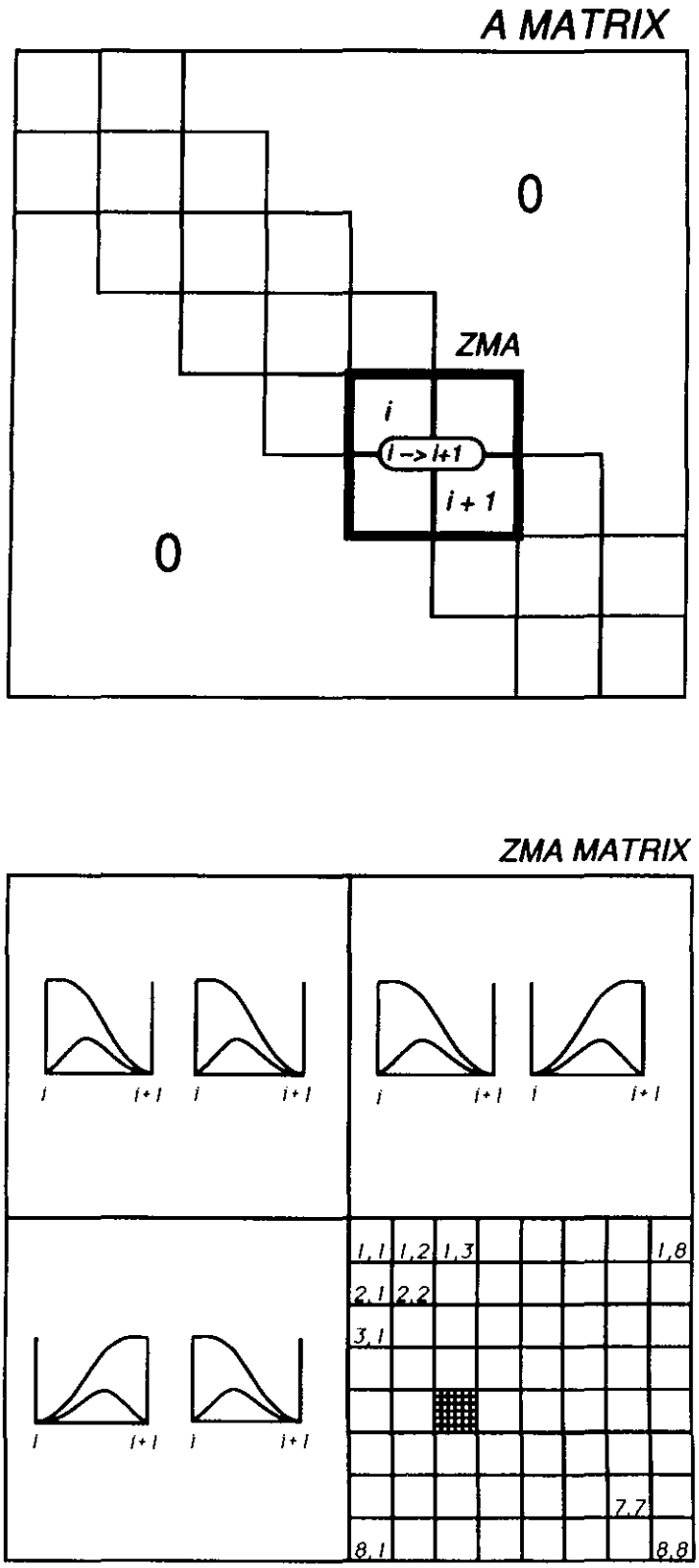


**Fig. A.1** *The structure of the A (B) matrix. The ZMA matrix contains the contribution to the weak form of one radial interval. The functions drawn in the ZMA matrix represent the two finite elements for each node.*

## Appendix B : Numerical testcases CASTOR vacuum

Before we can apply the CASTOR code with the added vacuum module to actual ideal and resistive free boundary problems, the code has to be tested in order to gain confidence in the results. In this paragraph we will give the results of some test cases for both the ideal and the resistive free boundary modes. Some attention is given to the accuracy with which the boundary conditions are satisfied and to the influence on the growth rate.

### B.1 The vacuum solution

For a test of the vacuum equations, independent of the plasma solution, we can, for example, use the analytic solution of the Laplace equation for an elliptical plasma boundary with an infinite aspect ratio. For a flat current density in the plasma, the angular coordinate of the straight field line coordinates (as defined in chapter 2) at the plasma boundary is identical with the angular coordinate of the separable orthogonal elliptic coordinates. The two coordinate systems are respectively given by:

$$\begin{aligned} x &= \sqrt{\psi}\cos\theta\,, & \hat{x} &= (E^2-1)^{1/2}\sinh\mu\,\cos\hat{\theta}, \\ y &= E\sqrt{\psi}\sin\theta\,, & \hat{y} &= (E^2-1)^{1/2}\cosh\mu\,\sin\hat{\theta}\,, \end{aligned} \qquad (B.1)$$

where $E$ is the ellipticity of the plasma boundary which is given by $\psi = 1$ or $\mu = \mu_0 = \tanh^{-1}(1/E)$. The general vacuum solution, for a toroidal mode number $n$ and the wall at infinity, is given by:

$$\Phi = \sum_m \Phi_m(\mu_0)\mathrm{e}^{-|m|(\mu-\mu_0)}\mathrm{e}^{im\hat{\theta}+in\phi}. \qquad (B.2)$$

The driving term $Jb^1$ at the plasma boundary is identical for the two coordinate systems. Thus, setting $(Jb^1)_m = (b_1)_m = \partial\Phi/\partial\mu = \delta_{m,m_{\mathrm{pert}}}$, we obtain a very simple vacuum response matrix:

$$(b_3)_m = \sum_{\bar{m}}\left(-in\frac{\delta_{m,\bar{m}}}{|m|}\right)(Jb^1)_{\bar{m}}. \qquad (B.3)$$

Note that, although in the analytic solution in the elliptic coordinates the Fourier harmonics are independent, this is not true in the coordinate system (4.35) used

in the numerical solution. In the vacuum the solution will consist of many coupled harmonics which must all go to zero at the boundary except for the driving harmonic. This makes the test of the vacuum solution non-trivial.

The equilibrium used for the test has an ellipticity of 2 and an aspect ratio of $10^4$. In Fig B.1, the $m = 2$ and 4 response, $\Phi_m$ at the plasma boundary on an $m = 2$ perturbation are plotted as a function of the number of equidistant radial grid points in the vacuum. The number of Fourier harmonics is 15. The shape of the wall is a confocal ellipse with $\mu = 3$. The numerically calculated response converges to the analytic values within the errors caused by the finite aspect ratio and the wall distance. Included in the figure are the values calculated using a non equidistant grid. The radial points are placed using a Gaussian distribution with a half width of $\sigma = 0.1$ with the maximum of the Gaussian at the plasma boundary. This greatly improves the convergence: the accuracy with 11 radial points is now of the same order as that with 51 equidistant points. The reason is the behavior of the vacuum solution near the plasma boundary. The vacuum solutions of $m = 2$ and $m = 4$ are shown in Fig. B.2, where the number of radial points, $N$, is 21 and $\sigma = 0.1$. The computational cost of the calculation of the vacuum response matrix is negligible compared to the actual eigenvalue calculation. The CPU time on an IBM 3090 is about $6 \times 10^{-4} NM^2$, i.e about $10\,s$ for a typical case.

## B.2 Ideal free boundary modes

The standard test case for ideal free boundary modes in toroidal geometry is the instabilities of the so-called Soloviev equilibrium. The growth rates of low-$n$ ($n = 1, 2$) instabilities for a number of different situations as obtained by ideal MHD stability codes (PEST, ERATO, NOVA) have been published [Cheng90] and can be used for comparison.

The Soloviev equilibrium (see Eq. 3.18) used here is characterized by $\epsilon_0 = 1/3$, $E = 2$ and $q_0 = 1.2$ is used here. The growth rate of the $n = 1$ instability is plotted in Fig B.3 versus the number of Fourier harmonics in the plasma. The number of radial grid points in the plasma is 21. Convergence up to the third decimal place is already obtained with 6 radial points. The vacuum response matrix is calculated with 31 harmonics and 51 radial grid points with $\sigma = 0.1$. Extrapolation to $M \rightarrow \infty$ yields a growth rate of $\lambda = 0.415$ or $\omega^2 = \lambda^2 q_1^2 = 0.75$. This value is to be compared with $0.75, 0.748$, and 0.78 calculated with, respectively, the PEST-1, NOVA, and the ERATO code.

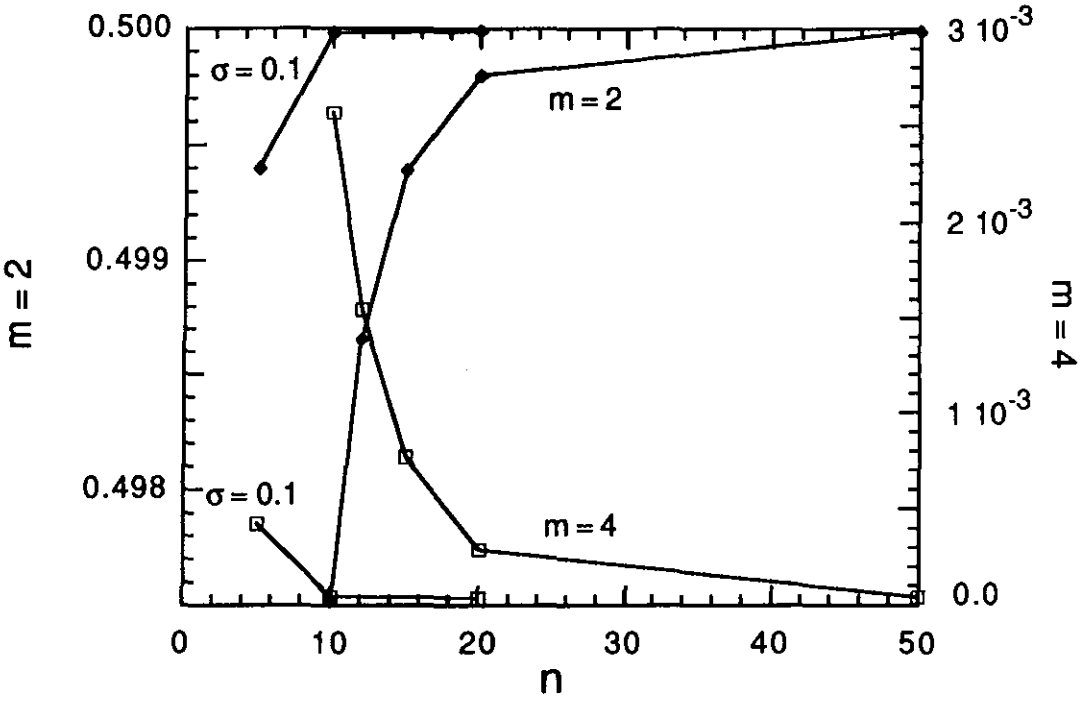


**Fig. B.1** *The amplitude of $m = 2$ and $m = 4$ Fourier harmonics of the vacuum solution, $\Phi_m$, at the plasma boundary as a function of the number of finite elements used in the vacuum solution. The curves marked by $\sigma = 0.1$ are calculated with the mesh accumulated near the plasma boundary.*

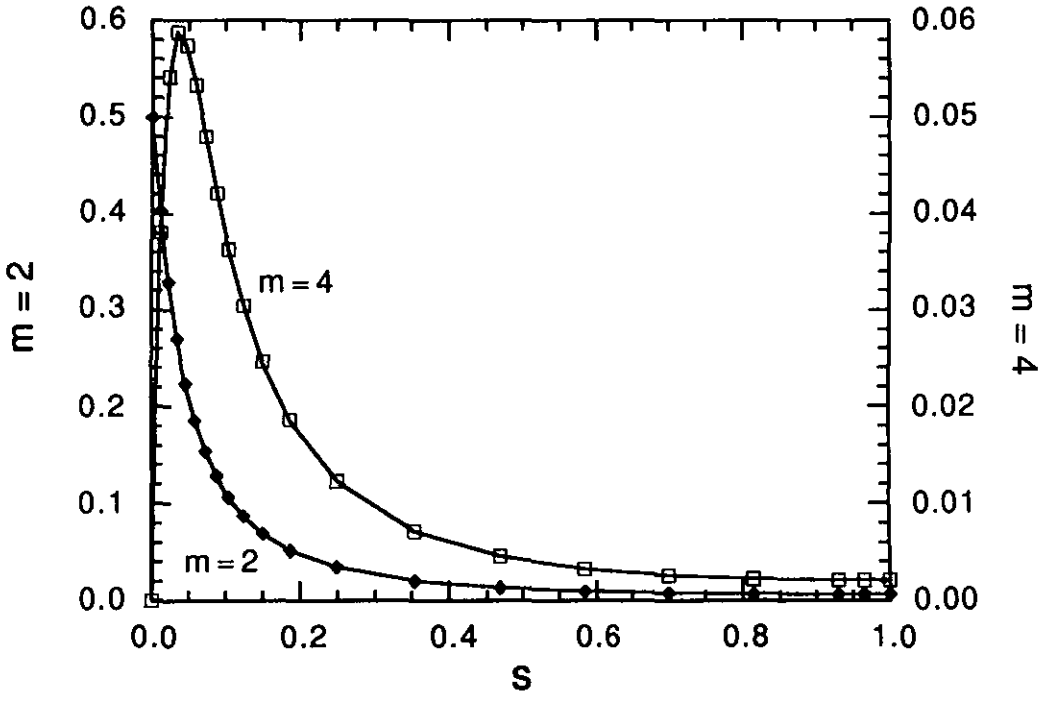


**Fig. B.2** *The $m = 2$ and $m = 4$ harmonics of the vacuum solution, $\Phi_m$, as a function of the radial coordinate in the vacuum.*

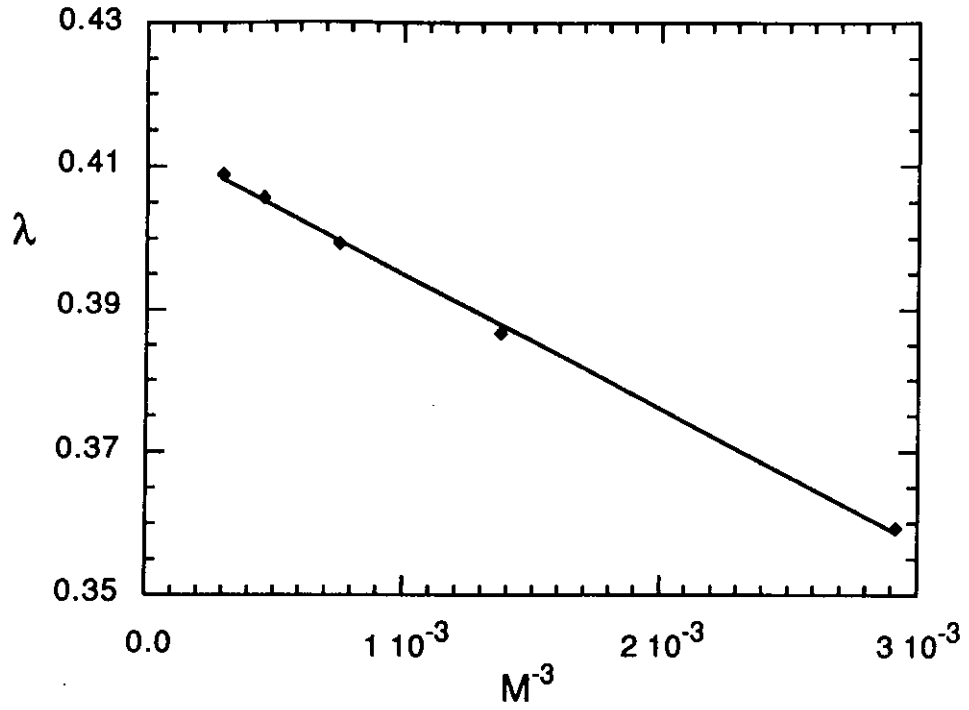


**Fig. B.3** *The growth rate of the $n = 1$ instability of the Soloviev equilibrium ($E = 2, \epsilon_0 = 1/3, q_0 = 0.6$) as a function of the number of Fourier harmonics in the plasma.*

## B.3 Resistive free boundary modes

Since no results of calculations of the growth rates of resistive free boundary modes in a general toroidal geometry have been published, we cannot fully test the resistive modes. Of course, results are known for cylindrical geometry and excellent agreement is found in the limit of infinite aspect ratio with the cylindrical resistive MHD code LEDA [Poedts89].

For testing the convergence of the error in the resistive boundary conditions, we calculate the eigenfunctions of an $n = 1$ free boundary resistive mode. The equilibrium is characterized by an ellipticity of 1.5, an inverse aspect ratio of 4 and a poloidal beta of 0.37. The two equilibrium profiles normalized to one on the magnetic axis, are given by $\Pi(\psi) = \Gamma(\psi) = 1 - \psi$. The $q$-profile is chosen such that the $q = 3$ surface is just inside the plasma ($q_{\text{edge}} = 3.003$).

In Fig. B.4 we have plotted the relative jump in the toroidal component of the $m = 3$ magnetic field perturbation at the plasma boundary as a function of the number of equidistant finite elements in the plasma for two values of the resistivity. It shows that the jump converges to zero with the third power of the radial grid

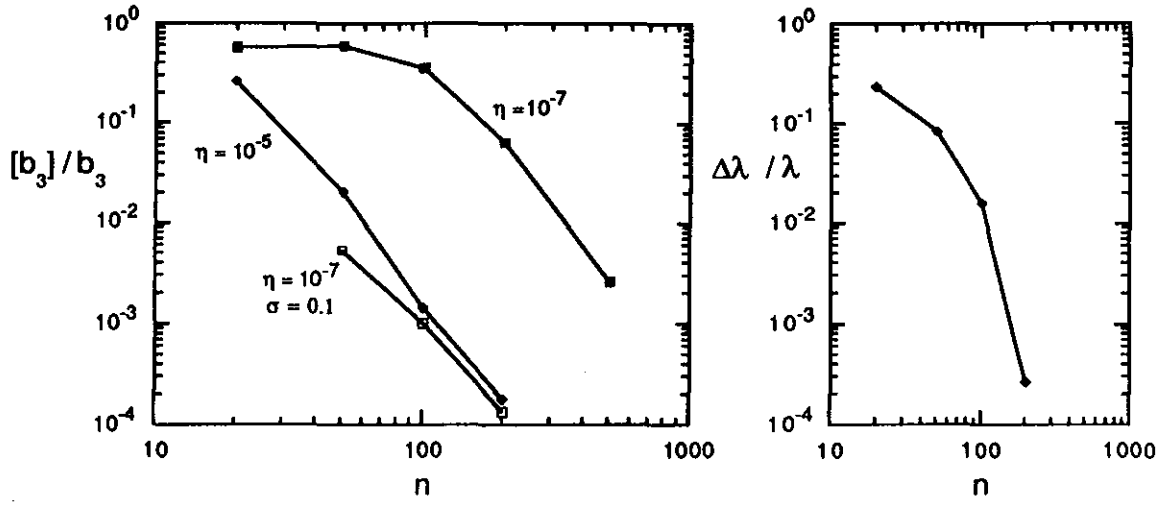


**Fig. B.4** *The relative jump in the toroidal magnetic field perturbation from the plasma to the vacuum as a function of the number of radial finite elements in the plasma for two values of the resistivity. Also shown (on the right) is the relative error in the growth rate as a function of the number of finite elements in the plasma ($\eta = 10^{-7}$).*

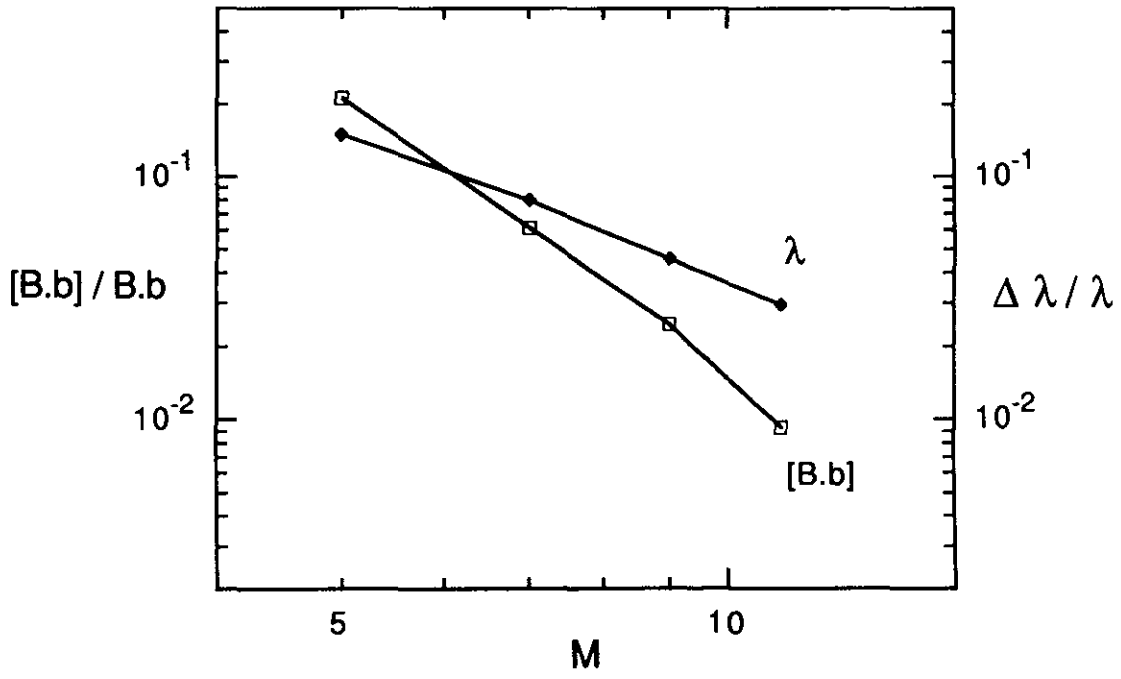


**Fig. B.5** *The relative jump in the component of the magnetic field perturbation tangential to the equilibrium magnetic field as a function of the number of Fourier harmonics used in the plasma.*

size. At smaller resistivities, the boundary layer at the plasma boundary gets smaller and more radial points are needed for an accurate representation of the layer. Using a non-equidistant mesh with the finite elements packed in the resistive layer greatly improves the accuracy of the boundary conditions. This is illustrated in Fig. B.4 for a mesh with a Gaussian distribution of the elements with a half width of $\sigma = 0.1$ centered at the boundary. Also drawn is the convergence of the relative error in the growth rate with an increasing number of equidistant elements. It shows that, as is to be expected, the growth rate converges much faster than the boundary conditions. The eigenfunctions of the velocity perturbations at a resistivity of $10^{-5}$ are shown in Fig. B.6. The boundary layer is most clearly seen in the $v_2$ component. The $m = 3$ harmonic peaks near the plasma edge but returns to zero in the resistive boundary layer.

The second resistive boundary condition, i.e. continuity of $\boldsymbol{B_0 \cdot b}$, shows a quite different behavior. The relative error in $\boldsymbol{B_0 \cdot b}$ appears to be independent of the number of radial grid points or the resistivity. The jump does converge to zero with an increasing number of Fourier harmonics. Fig. B.5 shows the relative error in $\boldsymbol{B_0 \cdot b}$ and in the eigenvalue as a function of the number of Fourier harmonics for a resistivity of $\eta = 10^{-7}$.

The different behavior of the boundary conditions on the two tangential magnetic field perturbations results from the different origins of the two conditions. The continuity of $\boldsymbol{B_0 \cdot b}$ is essentially the same as the ideal MHD pressure balance condition and is therefore not affected by the resistive boundary layer. The jump in the other tangential component of the magnetic field perturbation in ideal MHD is connected with a surface current density in the perturbation. In resistive MHD, the surface current density is resolved in the resistive boundary layer at the edge. Thus, it is essential to accurately represent the boundary layer in order to satisfy the resistive boundary conditions.

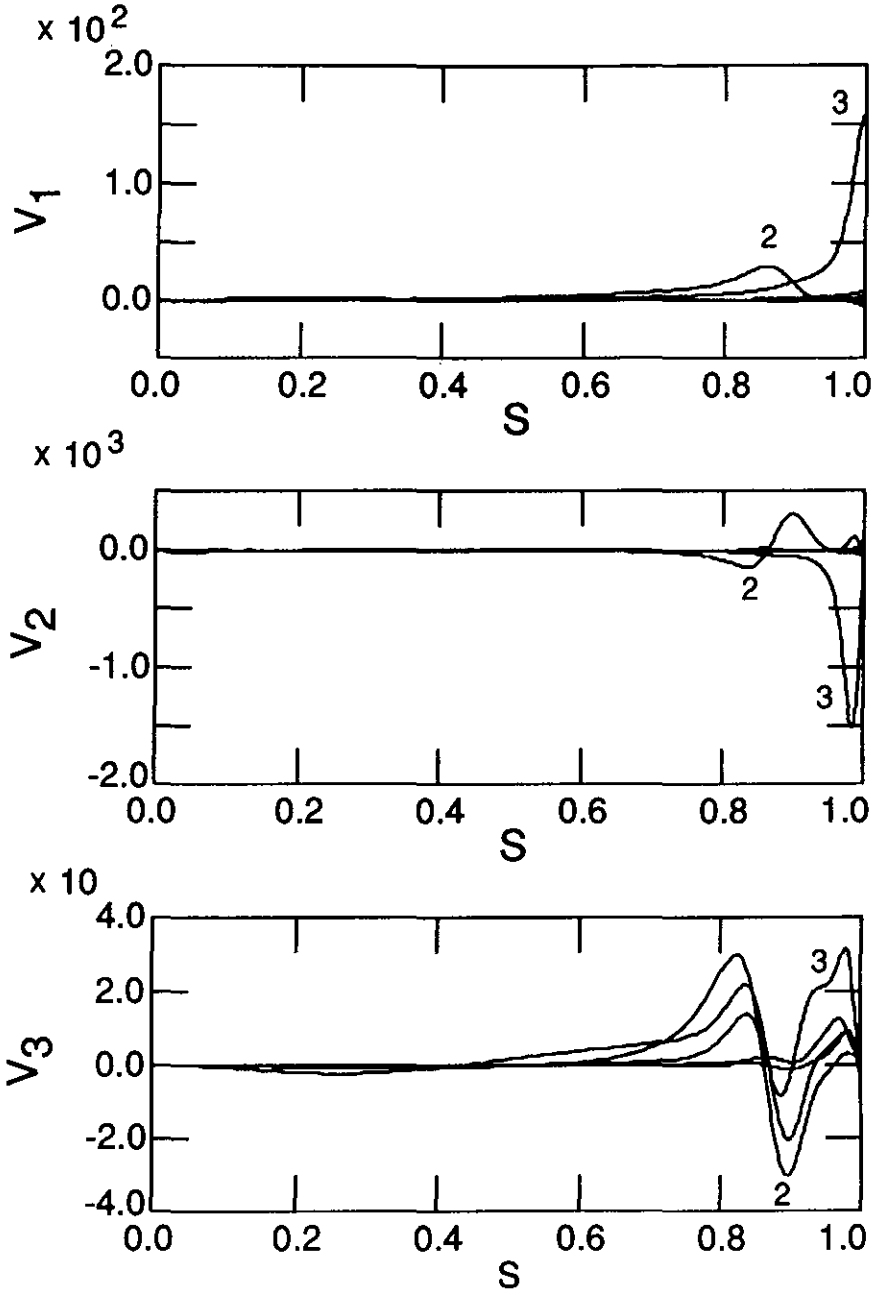


**Fig. B.6** *The Fourier components of the three components of the velocity perturbation as a function of the radial coordinate in the plasma. The labels refer to the* $m = 2$ *and* $m = 3$ *harmonics. Note the resistive boundary layer near* $s = 1$ *where* $v_2$ *and* $v_3$ *must go to zero.*

## Appendix C : Continuous spectrum code CSCAS

### C.1 The ideal MHD continuous spectrum

When the equilibrium quantities vary only in one spatial direction and are constant on magnetic surfaces, the perturbed quantities can be Fourier analyzed in the two ignorable spatial coordinates and each Fourier component can be studied separately since there is no interaction between them. The continuous parts of the spectrum can then be determined in an algebraic manner as they correspond to the singularities of the coefficients of a second-order ordinary differential equation (the Hain-Lüst equation). The Alfvén continuum, for instance, is given by the dispersion relation $\omega_a(\psi) = \vec{k}(\psi) \cdot \vec{B}_0(\psi)/\sqrt{\mu\rho_0(\psi)}$, with $\vec{k}$ the wave vector. In equilibria with inhomogeneity in two spatial directions, however, the equilibrium quantities also vary on magnetic surfaces and this loss of symmetry makes the determination of the continuous spectrum considerably more complicated. The continuous spectrum of static, axisymmetric and toroidal plasmas has been derived independently by [Goedbloed75] and [Pao75]. These authors showed that in such a plasma the continuous spectrum is determined by a reduced (one-dimensional non-singular) eigenvalue problem for a fourth-order system of ordinary differential equations on each flux surface. The reduced equations are obtained upon limiting the analysis to the neighbourhood of a particular flux surface $\psi = \psi_0$ and neglecting smaller terms. The coefficients of this reduced eigenvalue problem are all non-singular and, consequently, this eigenvalue problem yields a discrete set of eigenvalues on each flux surface. However, each eigenvalue of this discrete set spreads out a continuous spectrum when the magnetic surface is varied. It can be shown [Goedbloed75, Pao75] that a solution of the non-singular eigenvalue problem on $\psi = \psi_0$ corresponds to an improper solution of the original singular problem with the same eigenvalue and with $v_{1\psi}$, $a_{1\theta}$, and $a_{1\phi}$ (and, hence, $B_{1\psi}$) diverging logarithmically as $\psi \longrightarrow \psi_0$, while the other components of the state vector diverge as $(\psi - \psi_0)^{-1}$.

The numerical method applied in CSCAS is essentially a convenient way to obtain the equations of the reduced eigenvalue problem that determines the continuous spectrum from the full set of ideal MHD equations by using the results of Pao and Goedbloed and avoiding any analytic manipulations of these equations.

## C.2 Numerical method

Clearly, the continuous spectrum can be determined by means of the normal-mode code CASTOR. However, this procedure is not efficient because of the excessive memory requirements of the QR-algorithm. The general matrix eigenvalue problem solved by CASTOR involves matrices with dimension $(d \times d)$ with $d = 16 \times N_\psi \times N_m$, where $N_\psi$ is the number of radial mesh points and $N_m$ the number of poloidal fourier components. The problem now is that, in order to determine the continuous part of the spectrum, $N_\psi$ has to be large because the singularities have to be resolved properly. Moreover, when strong mode coupling occurs, $N_m$ has to be large too. The alternative inverse vector iteration does not have such severe memory requirements but demands a lot of CPU and, hence, this method is not efficient either.

Given a solver for the general ideal-MHD eigenvalue problem, such as CASTOR, the ideal continuous spectrum can easily be obtained by prescribing the radial dependence which is known to be singular and logarithmic in nature as discussed above. This is done by focussing on one magnetic flux surface and replacing the cubic finite elements by $\log(\epsilon)$ and the quadratic elements by $1/\epsilon$, with small $\epsilon$, *e.g.* $10^{-8}$. This approximates the logarithmic singularity of the radial velocity- and magnetic field components, and the $(\psi - \psi_0)^{-1}$-type singularity of the other dependent variables and introduces an ordering of the terms in the general ideal MHD equations analoguous to the ordering introduced by Pao and Goedbloed to obtain a reduced eigenvalue problem on $\psi = \psi_0$. This method has been implemented in CASTOR which resulted in the program CSCAS (Continuous Spectrum from **CAS**tor). The resulting reduced eigenvalue problem is solved with the QR-algorithm for a finite number of $\psi_0$'s. This reduced eigenvalue problem is determined by only $8 \times N_m$ equations and, hence, the memory problems are solved. In addition, the method turns out to be very efficient too. For five Fourier harmonics and 100 flux surfaces, for instance, CSCAS requires only 12 CPU seconds to detemine the range *and* the internal structure of the continuous spectrum.

## Appendix D : AUXILIARY PROGRAMS

### D.1 REVISE : a portable facility for structured program development

In an international group of scientists collaborating on related subjects and using the same numerical codes an immediate need arises with respect to communication on the development of these codes: How to control and to exchange the progression of changes, avoiding the introduction of mistakes, informing fellow collaborators of yet another version of their daily working tool, while stimulating growth of these tools? REVISE is a package of portable FORTRAN codes developed precisely for this purpose. Its use requires the source codes to be brought in a special precompile format so that changes can be detected, documented, and communicated easily. The five functions of creating a new source list, precompiling a FORTRAN program from the source, comparing a new source with a previous list, creating a modification set, and extracting a new source code from a REVISE list are cast in five auxiliary programs called NEW, PRE, COM, MOD, and EXT. These programs and their companion system procedures have been perfected and installed at the computers of IPP Garching, KUL Leuven, FOM Nieuwegein (i.e. SARA, Amsterdam), and JET. The agreement on this way of communication has turned out to be invaluable for the coherence of the numerical work of the collaborating groups.

REVISE is a portable facility for the systematic maintenance of large computer programs which combines the positive features of updating and screen editing (rigor and speed), while avoiding the negative ones (slowness and generation of errors). The basic information of a changing program (deck names, numbered lines, index, etc.) is stored into a LIST file which serves as a starting point for comparison with later versions of the same program.

REVISE consists of five programs:

| | | | |
|---|---|---|---|
| 1 a) | NEW FORTRAN A : | S $\longrightarrow$ L | (new list) |
| b) | PRE FORTRAN A : | S $\longrightarrow$ F (edit) | (precompile) |
| 2 a) | COM FORTRAN A : | L + S' $\longrightarrow$ M | (compare) |
| b) | MOD FORTRAN A : | L + M $\longrightarrow$ LM , L' | (modify) |
| c) | EXT FORTRAN A : | L(') $\longrightarrow$ S(') | (extract) |

written in Fortran 77, where the abbreviations have the following meaning:

| | | |
|---|---|---|
| S = SOURCE, | L = LIST, | F = FORTRAN, |
| S' = new SOURCE, | LM = LISTM, | |
| M = MODIF, | L' = new LISTR. | |

A usual FORTRAN file is brought into the required REVISE format by inserting the following instructions :

*COMDECK comdeck name
(followed by a comdeck, usually a COMMON block)
*DECK deck name
(followed by a deck, usually a subroutine)
*CALL comdeck name (instructing the precompiler to insert that comdeck)
*IF site1
(followed by FORTRAN lines pertinent to site1)
*ELSEIF site2,site3
(followed by FORTRAN lines pertinent to site2 and site3)
*ENDIF (closing the particular branching part refering to the different sites).

Modifications of the SOURCE thus obtained are then exchanged by means of MODIF files consisting of the following instructions:

*IDENT MOD_nr
*/ comment lines
*D deckname.l1,l2
(followed by new FORTRAN lines replacing the indicated ones)
*I deckname.l
(followed by new FORTRAN lines inserted after the indicated one).

This mechanism allows users to keep track of the evolution of the code, while exchanging this information in a very condensed form.

Departing from a SOURCE in REVISE format, such as CASTOR8 as partly listed in Appendix A1, a typical sequence of commands would be the following:

1) User A creates a new LIST file from the SOURCE:

"NEW CASTOR8"

(CASTOR8.SOURCE $\longrightarrow$ CASTOR8.LIST)

2) He receives a modification file from user B (e.g. by E-mail) and wishes to make a list of the modifications as well of the revised source resulting from it:

"MOD CASTOR8 MCAS8A CAS8A"

(CASTOR8.LIST + MCAS8A.MODIF $\rightarrow$ CAS8A.LISTM, CAS8A.LISTR)

3) Obviously, the revised source list on the LISTR file is only useful if user A can extract the new SOURCE from it:

"EXT CAS8A"

(CAS8A.LISTR $\longrightarrow$ CAS8A.SOURCE)

4) Next, user A develops the code further by just using any editor (but properly updating the name of the file):

(CAS8A.SOURCE $\longrightarrow$ CAS8B.SOURCE)

5) He then precompiles the appropriate FORTRAN file by means of PRE, which inserts the COMMON blocks and activates the FORTRAN lines pertinent to his particular site:

"PRE CAS8B"

(CAS8B.SOURCE $\longrightarrow$ CAS8B.FORTRAN)

6) Obviously, the FORTRAN file is then compiled and executed, while the steps 4 and 5 may be performed many times in between.

7) Finally, user A decides that his version of the code is a genuine improvement which he wishes to communicate to user B. To that end he creates a modification file:

"COM CASTOR8 CAS8B"

(CASTOR8.LIST + CAS8B.SOURCE $\longrightarrow$ MCAS8B.MODIF)

In this manner, it is possible for physicists to collaborate on the same program while permitting to make any changes that are required in the course of the investigations.

## D.2 PPPLIB : Plasma Physics Plotting Library

The portable package of FORTRAN plotting routines PPPLIB has been installed at the sites of the collaborating groups mentioned under D1. This has turned out to be another means of safeguarding the coherence of the numerical programs since this avoids the need of constant rewriting diagnostic parts of the codes calling local plotting facilities. A modernised version of this package (PPP15) has been developed which may deliver CALCOMP as well as Postscript files to be directly processed by a laserprinter. A description of the old version of the code (PPP10) is found in [Goedbloed86]. Whereas the quality of the plots is substantially improved through use of Postscript, the calls to the new version are unchanged. For details the user should consult the source which is completely documented internally.